Computational Studies on the Mechanism of Alkane Dehydrogenation on 2D layered TiS₂ and the Electronic Structure of a Manganese Dimer

Joëlle Siewe

4290151

Prof. Dr. Marc-Etienne Moret &

Prof. Dr. Mu-Hyun Baik

15/02/2020

Abstract

Firstly, the possibility of dehydrogenating linear and cyclic alkanes catalyzed by 2D layered Transition Metal Dichalcogenide, 1T-TiS$_2$, was investigated with Density Functional Theory. The dehydrogenation mechanisms for cyclohexane and *n*-butane as representative reactants, were explored. The most likely reaction mechanism for C–H was found to occur on an edge-based S–S couple for both C–H activation steps. The first C–H activation reaction exhibited a reaction energy of –14.2, –12.7 and –12.0 kcal/mol for cyclohexane and *n*-butane addition, respectively. In contrast, the second C–H activation on the neighboring C-atom, was found to be comparatively unfavorable, resulting in an increase in energy to 19.6, 22.5 and 19.0 kcal/mol for formation of cyclohexene, 1-butene and 2-butene, respectively. Since there have been no published studies on the dehydrogenation of linear and cyclic alkanes on TiS$_2$ thus far, this study may provide a guideline to further computational or experimental investigations.

Secondly, the electronic structure of a dimeric manganese hydride catalyst supported by β-diketiminate ligands, [(2,6-iPr2PhBDI)Mn(μ-H)]$_2$, was investigated with Density Functional Theory. An apparent triple bond between two manganese centers was anticipated to compensate for the electron-deficient nature of each metal center. However, our calculations interestingly revealed the absence of a multiple bond between the metal centers. In accordance with experimentally determined Heisenberg exchange coupling constants of –10.2 cm$_{-1}$, the calculated J_o value of –10.9 cm$_{-1}$ confirmed that the ground state involves antiferromagnetic coupling between high spin d_5 Mn(II) centers. The effect of steric bulk on the bond order was interrogated via a model study with the least sterically demanding version of the β-diketiminate ligand and was found to be negligible. Mixing between metal- and ligand-based orbitals was alternatively designated as the main cause of the absence of a metal–metal multiple bond. Moreover, the specificity of hydrides providing only s-orbitals affords a relatively close positioning of the metal centers, while bridging ligands including p-orbitals perturb a bonding orbital between metal centers, lengthening the Mn–Mn distance. The proximity of the metal centers in [(2,6-iPr2PhBDI)Mn(μ-H)]$_2$ leads to an increase in Pauli repulsion, resulting in destabilization of the dimer. The accessibility of the monomeric species may be the origin of the catalytic activity that [(2,6-iPr2PhBDI)Mn(μ-H)]$_2$ exhibits.

Table of Contents

Introduction

This thesis describes the efforts and results of two different projects that are based on computational research. The first is a completely theoretical study on the dehydrogenation of linear and cyclic alkanes catalyzed by 2D layered TiS_2, which was investigated by the author of this thesis alone. The second is a collaborative effort between the author of this paper, Changjin Oh, a PhD student at Professor Baik's group, with who the computational part of this research was carried out, Professor Ryan Trovitch from Arizona State University, and Professor John Anderson from The University of Chicago, both of whom performed experiments and measurements supporting the computational investigation. This project concerns the electronic structure of a β-diketiminate manganese dimer with bridging hydrides, which Professor Trovitch and coworkers previously synthesized and used for the first time to catalyze hydrosilylation of alkenes.[1] This research is currently being prepared for publication.

The purpose of this division is to show the different applications of Density Functional Theory and computational modeling. The first investigation is a purely theoretical study to gain insight into the possibilities of performing a certain catalytic reaction and elucidating the potential reaction mechanism. On the other hand, the second is an investigation into the electronic structure of an organometallic compound in order to better understand the origins of the catalytic activity that the compound in question exhibits.

Density Functional Theory

In order to use molecular quantum mechanics to make predictions on a certain chemical system, a solution should be found to the time-independent Schrödinger equation:

$$\hat{H}\psi = E\psi \tag{1}$$

with E being the electronic energy, $\psi = \psi(x_1, x_2, ..., x_n)$ the wavefunction, and $\hat{H}$ the Hamiltonian operator:

$$\hat{H} = \sum_{i=1}^{N}(-\tfrac{1}{2}\nabla_i^2) + \sum_{i=1}^{N} v(\boldsymbol{r}_i) + \sum_{i<j}\frac{1}{r_{ij}} \tag{2}$$

with the "external" potential v acting on electron i due to nuclear charges Z_α being:

$$v(r_i) = -\sum_\alpha \frac{Z_\alpha}{r_{i\alpha}} \tag{.3}$$

The Hamiltonian basically consists of three factors: 1) a kinetic energy term T, 2) a potential energy term describing the electron-nucleus attraction V_{ne} and 3) a second potential energy term for electron-electron repulsion V_{ee}:

$$\hat{H} = T + V_{ne} + V_{ee} \tag{4}$$

There is currently no method in existence that can exactly solve the Schrödinger equation. Instead, the variational principle is used to approach the solution systematically. The variational principle states that the energy that is calculated using trial wavefunctions ψ_{trial} results in an upper bound of the true energy, such that

$$\langle\psi_{trial}|\hat{H}|\psi_{trial}\rangle = E_{trial} \geq E_0 = \langle\psi_0|\hat{H}|\psi_0\rangle \tag{5}$$

and E_{trial} can only equal E_0 if ψ_{trial} exactly matches ψ_0. This means that function ψ_0 will give the lowest energy, E_0. This approach, however, would require searching through all possible N-electron wavefunctions for that system.

The Hartree-Fock method approximates the N-electron wavefunction by taking the antisymmetrized product of N one-electron wavefunctions $\chi_i(x_i)$, also called a Slater determinant, Φ_{SD}, given here as the short-hand notation:

$$\Phi_{SD} = \frac{1}{\sqrt{N!}}det\{\chi_1(r_1)\chi_2(r_2)...\chi_N(r_N)\} \tag{6}$$

The one-electron wavefunctions are spin orbitals, consisting of a spatial orbital term $\varphi_i(r)$ and of spin functions $\alpha(s)$ or $\beta(s)$, which are orthonormal. The variational principle can then be used to find the Slater determinant that gives the lowest energy. The presence of the Fock operator which depends on the spin orbitals/the eigenvalue problem solutions that need to be solved, gives rise to an eigenvalue equation that can only be solved iteratively through a self-consistent field (SCF) process. As mentioned before, due to the fact that the Slater determinant cannot exactly match the ground

state wave function, the calculated energy is always larger than the true ground state energy E_0. The difference between the Hartree-Fock derived energy and the true ground state energy is called the correlation energy E_{HFC}. Contributing to this correlation energy is the dynamical electron correlation, caused by electron–electron repulsion. This is calculated to be too large by the Hartree-Fock procedure, because only the average electrostatic interaction is taken into account. This causes the electrons to move too close to one another. Secondly, there is a non-dynamical correlation, which stems from the Slater determinant not approximating the true ground state, which should ideally be expressed as a linear combination of many different determinants that represent different states. Many higher level methods have been developed in the past to correct these shortcomings that are in principle well-understood.

These post-Hartree-Fock methods can produce highly accurate results, but are practically not useful for models of realistic size, as the computational cost becomes intractable quickly. Whereas the simple Hartree-Fock method scales as N_3, where N is the number of electrons, post-Hartree-Fock methods can scale as high as N_6. By using a quantity such as the electron density, as opposed to wavefunctions, the amount of variables can be reduced to simply 3N, because a density only depends on the 3D space. Furthermore, the electron density is an observable quantity, through methods such as X-Ray Diffraction, which wave functions are not. It can be shown that the electron density intrinsically contains all the key quantities needed to create the Hamiltonian.

Although there are earlier theories that utilize the electron density to calculate the ground state energy, such as the Thomas-Fermi model, the Hohenberg-Kohn theorem proves that the electron density indeed gives rise to a unique functional for $V_{ext}(r)$ and therefore the Hamiltonian $\hat{H}$. The electron density is given in terms of ψ as:

$$\rho(r) \ = \ N \iint |\psi(x_1, x_2, \ldots, x_N)|^2 \, dx_1 dx_2 \ldots dx_N \tag{7}$$

The energy can then be rewritten from equation (2.7) as:

$$E_0[\rho_0] \ = \ \int \rho_0(r) V_{ne} dr \ + \ T[\rho_0] \ + \ E_{ee}[\rho_0] \tag{8}$$

in which the first term is system dependent and the last two terms are system independent and form the Hohenberg-Kohn functional $F_{HK}[\rho_0]$. This Hohenberg-Kohn functional gives the expectation value $\langle \Psi | T + V_{ee} | \Psi \rangle$, the sum of the kinetic energy and electron–electron repulsion. This equation can still never lead to the exact energy, as the exact form of both the kinetic energy $T[\rho]$ and the electron-electron interaction, $E_{ee}[\rho]$, are not explicitly known.

Hohenberg and Kohn postulated a second theorem equivalent to the variational principle, stating that the calculated energy can only be the ground state energy if the density used is the ground state density, ρ_0, expressed as:

$$E_0 \leq E[\rho_{trial}] + E_{ne}[\rho_{trial0}] + E_{ee}[\rho_{trial}] \tag{9}$$

Finally, the ground state energy, E_0 can be expressed as:

$$E_0 = min_{\rho \to N}(F[\rho] + \int \rho(r)V_{Ne}dr) \tag{10}$$

where F[ρ] represents the universal formula $E[\rho] = min_{\rho \to N} \langle \psi | T + V_{ee} | \psi \rangle$, which is defined for all densities originating from antisymmetric wavefunction Ψ and contains the kinetic energy $T[\rho]$, classical Coulomb interaction J[ρ], and non-classical interaction $E_{ncl}[\rho]$, such as self-interaction. Only the Coulomb interaction is explicitly known. Previous attempts had been made at defining the kinetic energy explicitly, but the results of these proved to be unstable and inaccurate. Kohn and Sham set out to solve this problem.

Kohn and Sham implemented a drastic simplification of the model by ignoring electron-electron interactions. This is expressed in Kohn-Sham orbitals as:

$$\rho(r) = 2\sum_i^{occ.}|\psi_i(r)|^2 = \rho_0(r) \tag{11}$$

On the other hand, by using this non-interacting system, Kohn and Sham realized that the true kinetic energy of the true system could not be calculated exactly. Rather, they used a formula that could be used to calculate the kinetic energy of the non-interacting system only:

$$T_s = -\frac{1}{2}\sum_1^N \langle \varphi_i | \nabla^2 | \varphi_i \rangle \tag{12}$$

The difference between the true kinetic energy T and the kinetic energy of the non-interacting system T_s, can then be added to a new term called the exchange-correlation energy, E_{XC}, which also includes the non-classical electrostatic interactions, E_{ncl}. Were the exchange correlation energy to be explicitly known, the Kohn-Sham approach would lead to the exact ground state energy, as opposed to the Hartree-Fock approach. Current research into density functional theory, therefore, focuses largely on the quest for the best approximation of the exchange correlation energy.

This section was summarized from *A Chemist's Guide to Density Functional Theory* by Wolfram Koch and Max C. Holthausen.[2]

1. Dehydrogenation of Linear and Cyclic Alkanes on 2D layered TiS$_2$

1.1 Introduction

Linear and cyclic alkenes, especially α-olefins, are high value reactants in industry, the vast majority of which are produced via steam cracking (SC).[3,4] SC is not a selective process, but rather produces a mixture of different hydrocarbons, making it difficult to precisely tune into market demands for specific chemicals.[5,6] Furthermore, as governments and consumers are pushing industry to search for cleaner, more sustainable solutions, alternatives to the highly energy intensive SC process are becoming increasingly important. Recent decades have seen a rise in the development of homogeneous catalysts that are capable of dehydrogenating alkanes, typically employing transition metals such as iridium, rhodium and ruthenium.[7–12] These catalysts form hydrides which may induce olefin isomerization, decreasing the selectivity towards the desired α-olefins. In 2017, Mindiola and coworkers reported the use of a titanium complex in tandem with a carbene transfer reagent to afford terminal alkenes, as well as some cyclic alkenes, with very high selectivity, since the Ti-complex does not form any hydrides, while using mild conditions.[13] Homogeneous catalysts, however, have some drawbacks, such as the need for solvents in many cases, as well as laborious and energy intensive separation methods required to collect the product in high purity. Employing heterogeneous catalysts instead provides good solutions to a number of these problems.

Metal oxides have been used to dehydrogenate alkanes such as propane and ethane. Cr_2O_3/Al_2O_3 and Pt─Sn/Al_2O_3 are widely used in industry for alkene dehydrogenation.[14] These metals, however, are either expensive or have toxic qualities, making them less favorable than other earth-abundant and less toxic alternatives. Furthermore, metal oxides tend to overoxidize alkanes, as the added value products in these reactions are more reactive under the reaction conditions. This increases selectivity to CO_x-type products.[15–17] One solution to this problem is to use sulfur as a milder oxidant than oxygen.[18,19]

Metal sulfides belong to a class of materials referred to as transition metal chalcogenides (TMCs), usually denoted MX$_2$ (X = S, Se or Te). TMCs have a variety of applications, such as electro- and photocatalysis and energy storage.[20–22] TiS$_2$, amongst others, was found to activate the C–H bond in methane and oxidatively couple carbon to form a new C–C bond in ethylene.[23] Activity and selectivity of these TMC catalysts was determined by the M–S bond strength; materials with stronger M─S bonds exhibited lower –CH$_2$ coupling activation barriers, while the C–H activation barrier

became higher. Unfortunately, this reaction requires temperatures over 1200 K to achieve sufficient yields and selectivities. Since titanium was also employed as a catalyst for alkane dehydrogenation under mild conditions, however, improvement of the TiS2 nanosheet could lead to better activity and selectivity.

As for most TMCs, catalytic activity on TiS_2 occurs on the edge sites, and not on the basal plane. This could limit turnover if the edges site/basal plane ratio is very low.[24–26] Cheon and coworkers found that several TMCs, including TiS_2, can be activated in the basal plane by reaction with Lewis acids such as $AlCl_3$.[27] This could improve the activity of the material as a catalyst. Although Marks and coworkers only probed C–H activation of methane, other literature suggests that larger alkanes, such as propane and isobutane may also be dehydrogenated by TiS_2.[28]

In this study, the potential mechanism of the dehydrogenation of linear and cyclic alkanes was investigated using Density Functional Theory, in order to elucidate the viability of performing this reaction experimentally. The dehydrogenation mechanism was studied on two representative reactants: cyclohexane, representing cyclic alkanes, and *n*-butane, representing linear alkanes. Since there are, to our knowledge, no previous studies on the dehydrogenation of cyclic or linear alkanes on TMDs, this investigation may provide novel insights aiding future investigations into experimentally performing this reaction.

1.2 Theory

1.2.1 Transition Metal Dichalcogenides

Transition Metal Dichalcogenides (TMDs), denoted as MX_2, where X = S, Se or Te, are a class of material consisting of a sandwich-like structure in which the transition metal (TM) is sandwiched between two chalcogen layers. Usually these "sandwich" layers are held together by Van der Waals forces in the bulk material.[29,30] This layered structure also allows for various methods to synthesize TMD nanosheets consisting of several or only one layer, such as exfoliation or vapor deposition.[30–32] TMDs have a variety of applications, including in catalysis, semiconductors and sensors.[20,33,34]

TMDs exist in several naturally occurring phases, the most common being octahedral (1T) and hexagonal (1H). Through phase engineering, alternative, non-thermodynamic phases, also called meta-stable phases, can be accessed, which can give rise to a change in the properties of the TMD.[35] The thermodynamically most stable phase of TiS_2 is the octahedral (1T) phase, referred to as $1T\text{-}TiS_2$ (Fig. 1.2.1).
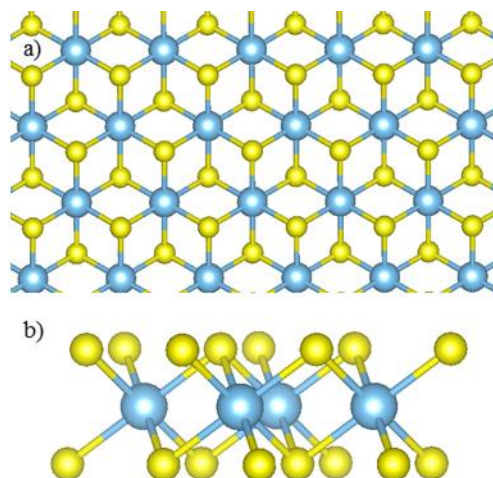
Fig. 1.2.1. The naturally occurring phase of TiS$_2$, octahedral or 1T-TiS$_2$, from a) top view onto the basal plane, and b) side view. Titanium = light blue; sulfur = yellow.

1.2.2 Model

Previous studies on MoS$_2$ nanosheets show that the shape of the nanosheet depends on the edge structure, which in turn is influenced by how sulfur-rich the environment is. In general, the most common edge structures are the zigzag edge and the armchair edge, which also occur for TiS$_2$. The zigzag edge structure is characterized by being S-rich, although S-poor zigzag edges, for example edges where only 50% sulfidation or no sulfidation at all, are also found. For MoS$_2$, the shape of the nanoflake can be influenced/changed by varying the chemical potential from Mo-rich to S-rich, which results in the mixture of zigzag/armchair edges to change to only zigzag edges, changes the nanosheet shape from dodecahedron to hexagon to triangle.

Since reactions of various TMDs with Lewis acids occur on the basal plane of the nanosheet, the edges of these TMDs are likely also Lewis acidic. Furthermore, both Zhu et al. and Li et al. calculated the stability of the occurring TiS$_2$ edge structures under varying chemical potential.[23,36] Both investigations found that, except for very high chemical potential, the 50% sulfided zigzag edge state, ZZ1, is the most stable, as can also be seen in Fig. 1.2.2. For this reason, the calculations on the dehydrogenation mechanism were performed on a TiS$_2$ cluster with exclusively the ZZ1 edge structure. Other edge structures, such as the 100% sulfided edge (ZZ2), the 0% sulfided edge (ZZ0), and the armchair edge (AC), were tested to compare the adsorption energies of the alkanes. Potentially, changing the edge structure could also change the reactivity of the TMD nanosheet.
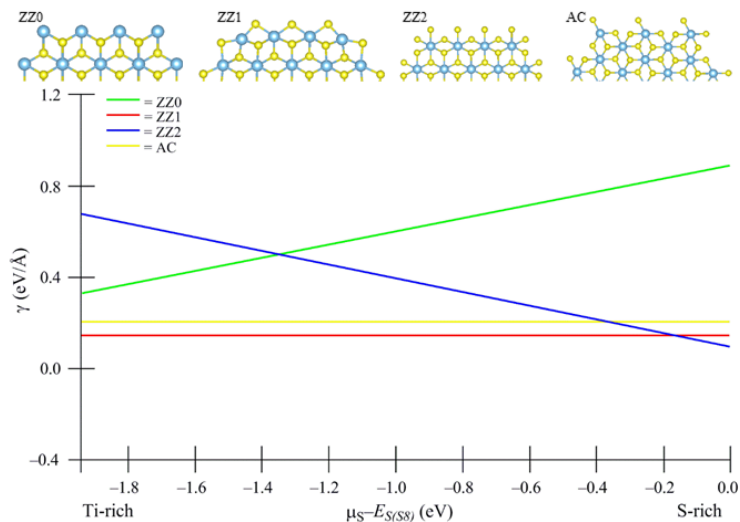
Fig. 1.2.2. The stability of the various 1T-TiS$_2$ edge structures, ZZ0, ZZ1, ZZ2 and AC. The figure is adapted from Li et al.;[36] similar results were also obtained by Zhu et al.[23] The stability was calculated using $\mu_{Ti} + 2\mu_S = E_{TiS_2(NS)}$, with μ_S being determined by the S$_8$ molecule for a S-rich environment, and the bulk Ti phase for a Ti-rich environment.

Zhu et al. mention that the C–H activation, as well as subsequent steps, occur on an S–S couple on the TiS$_2$ edge,[23] however this is unlikely to be the result of atomic S$_2$ adsorption on the edge, due to the above mentioned stability issue. Rather atomic sulfur is required to replenish the S-atoms on the nanosheet edge, as the reaction produces H$_2$S as a product also.

1.2.3 C–H Activation

C–H bond activation is an important chemical process, as it allows for the transformation of alkanes into value-added products in a very direct manner. Alkanes, of course, are widely available, but they are very inert, making C–H activation difficult to achieve. Mostly, production of value-added compounds, such as alcohols and carboxylic acids, uses alkenes as reactants, as they are much more reactive than alkanes. As mentioned, in the introduction, however, alkenes are in turn produced by the highly energy intensive steam cracking process. Therefore, accessing these value-added compounds directly through the naturally occurring alkanes, could be much more efficient and sustainable.

In general, three major pathways to activate C–H bonds can be identified: 1) homolytic cleavage or a radical pathway:

$$R\text{–}H \rightarrow R^{\cdot} + H^{\cdot} \tag{1.1}$$

2) heterolytic cleavage, whereby a proton is abstracted from the alkane:

$$R\text{–}H \rightarrow R\text{:}^{-} + H^{+} \tag{1.2}$$

and 3) heterolytic cleavage with hydride abstraction from the alkane:

10

$$R-H \rightarrow R^+ + H:^- \tag{1.3}$$

Here, these three mechanisms will be described briefly. For a more in depth overview of the various alkane C–H activation pathways, the reader is referred to a review on alkane CH activation pathways with organometallic compounds.[37]

Homolytic Cleavage

C–H bonds undergo homolytic cleavage under attack from a, usually organic, radical. The radicals contain a SOMO, or singly occupied molecular orbital, which can either attack the HOMO or the LUMO of a bond. In the case of a C–H bond, the σ and σ* orbitals are available, but due to the high energy of the σ* orbitals, the SOMO will interact with the σ orbitals, or the HOMO. The radical in this case, acts as an electrophile. One example of this is the oxygen radical often used in biological processes, such as a hydroxyl or alkoxyl radical.[38]

A well-known example of homolytic C–H bond cleavage is the rebound mechanism.[39][ref] The hydrogen is abstracted from the reactant by the oxygen moiety, leaving the alkyl radical. This radical can then attack the newly formed hydroxide moiety, generating an alcohol complex. The rebound mechanism is commonly found in nature with the cytochrome P450 enzyme.[38,40–42]
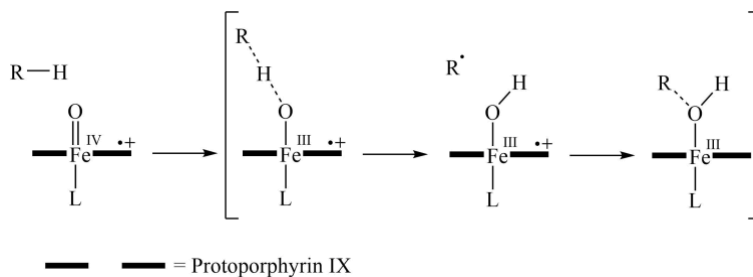
Fig. 1.2.3. The rebound mechanism as a pathway to C–H activation. Adapted from ref. 41.

Heterolytic Cleavage of Proton

Amongst the two heterolytic cleavage pathways, the pathway following proton abstraction is probably more common than that with hydride abstraction. A simple example of heterolytic C–H bond cleavage with proton abstraction is σ-bond metathesis.[43,44] This heterolytic cleavage is often catalyzed by organometallic, M–X type complexes, where X is a heteroatom. This results in M–C and X–H type products.

Fig. 1.2.4. The σ-bond metathesis mechanism as a pathway to heterolytic cleavage via proton abstraction. Adapted from ref. 44.

Heterolytic Cleavage of Hydride

A second heterolytic cleavage pathway of C–H bonds abstracts not a proton, but a hydride. This pathway is usually found for organometallic complexes with extremely electron-poor metal centers.[45] An example of heterolytic cleavage of the C–H bond via hydride abstraction in β-hydride elimination. This usually leads to a metal-hydride, but the hydride can also be concertedly transferred to another substrate shown below in Fig. 1.2.5.[46]
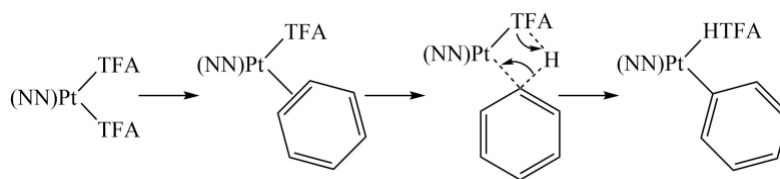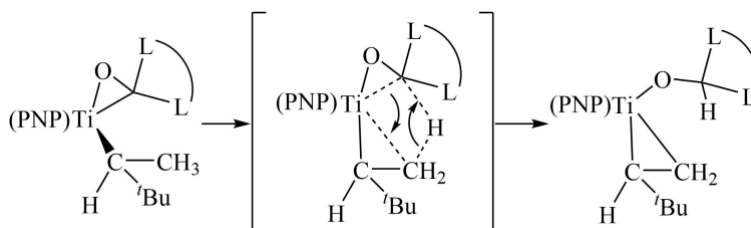

Fig. 1.2.5. The concerted β-hydride elimination-hydride transfer mechanism as a pathway to heterolytic cleavage via hydride abstraction. Adapted from ref. 46.

1.2.4 Proposed Mechanism

The reaction mechanism presented here is based largely on the reaction mechanism explored in the Zhu et al. paper of 2013. Cyclohexane and *n*-butane are used as representative substrates. The proposed mechanism for cyclohexane dehydrogenation is presented in Fig. 1.2.6. The full catalytic cycle is shown in Fig. 1.2.6a), including the expected intermediates and transition states. As shown in Fig. 1.2.6b), there are two basic steps: 1) the first C–H activation step over two S-atoms, and 2) the second C–H activation step of the adsorbed alkyl on another S-atom, which eliminates the alkene and H_2S.
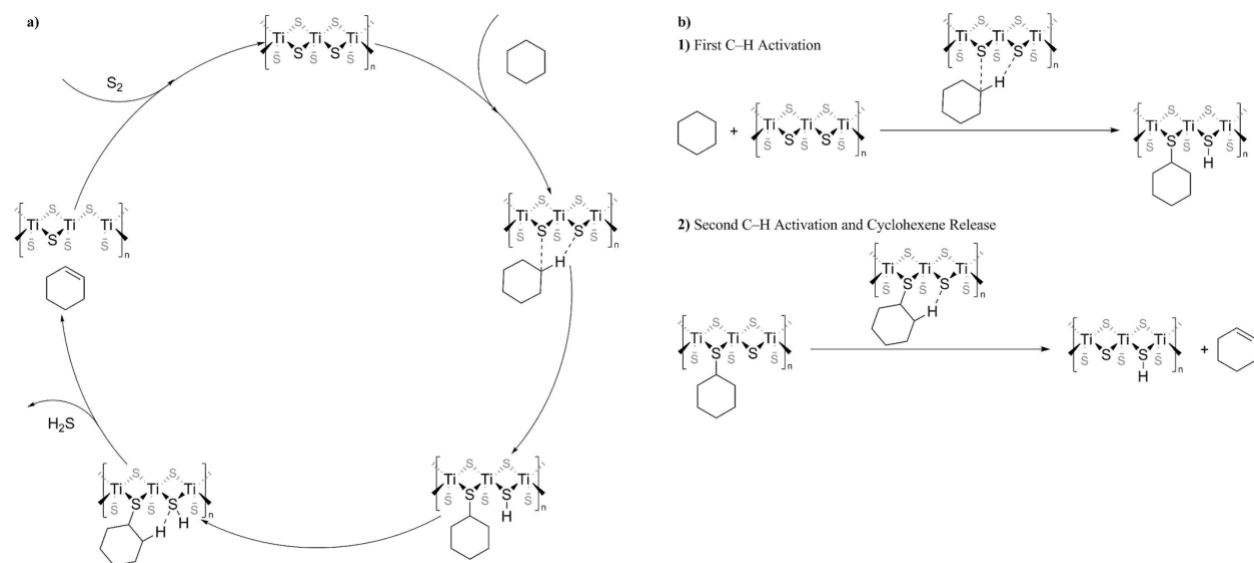
Fig. 1.2.6. a) The proposed catalytic cycle of cyclohexane dehydrogenation to cyclohexene, b) the individual C–H activation steps shown as they were applied in the calculation. The full catalytic cycle, including H_2S production, was not considered. Instead the C–H activation steps were investigated separately. The ZZ1 edge structure of the 1T-TiS_2 nanosheet is depicted schematically, with only the nearest neighbors of the edge-based Ti-atoms showing for clarity.

Cyclohexane is a relatively straightforward substrate; due to its symmetry and the fact that each carbon atom in the cycle has an identical environment, there is only one possible product. Butane dehydrogenation on the other hand, can afford both 1-butene and 2-butene, even when isomerization is not taken into account. Therefore, there are two possible pathways through which to achieve the first C–H activation step, shown in Fig. 1.2.7 a) and b), and three pathways for the second C–H activation, as shown in Fig. 1.2.7 c), d) and e).

Fig. 1.2.7. The possible pathways for butane dehydrogenation, affording 1-butene or 2-butene. The first C–H activation can result in adsorption on a) the C1 position, or b) the C2 position. Subsequently, the second step can lead to the production of 1-butene via C–H activation on c) the C2 position or d) the C1 position, whilst C–H activation on e) the C3 position will lead to 2-butene.

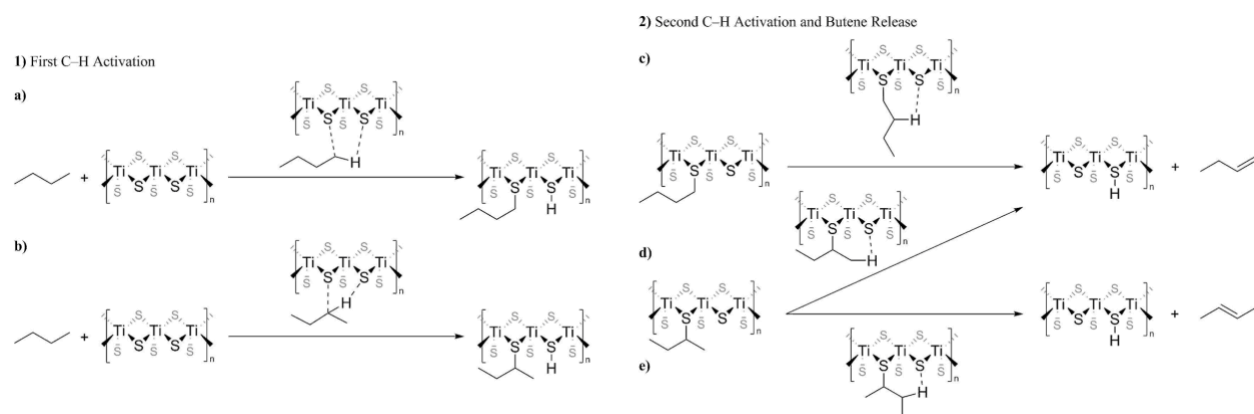As indicated, both of these C–H activations are assumed to occur over two different S-atoms, based on the investigations by Marks and coworkers, and Shan and coworkers.[23,28] This means that a homolytic cleavage or radical mechanism for C–H activation was considered.

1.3 Computational Details

The intermediates and transition states were all located with the density functional based tight binding (DFTB) program as implemented in the Amsterdam Modeling Suite (AMS).[93] The GFN1-xTB functional was used for geometry optimization and single point energy calculation.[47] Recently, Grimme and coworkers have published a second version of the extended tight-binding functional, GFN2-xTB, which is more accurate than the first version;[48] however, this new functional was not available in AMS at the time of this investigation. Extended tight-binding functionals are advantageous over the more common self-consistent charge density functional tight-binding (SCC-DFTB) in that they do not use precalculated integrals, requiring the appropriate parameter files. Instead, extended tight-binding uses an extended Hückel-like Hamiltonian approximation, together with Slater-type orbitals. An energy cutoff of $1.0 \cdot 10_{-5}$ was employed. No periodic boundary conditions were applied to the 1T-TiS$_2$ hexagonal nanosheet cluster. The orbital occupation strategy was set to automatic.

Attempts were made at locating the related transition states by performing a potential energy surface (PES) scan along the reaction coordinate of the expected transition states, and subsequently running a transition state search from an initial guess taken from the PES scan. Unfortunately, this method proved to be unsuccessful, as transition states could not be located from any initial guess. Therefore, transition states were not considered in the discussion.

1.4 Results & Discussion

In this section the dehydrogenation mechanism of the two representative substrates, cyclohexane and *n*-butane, will be presented and discussed. First, the cyclohexane dehydrogenation mechanism will be examined, as it is the more straightforward of the two. Then, the *n*-butane dehydrogenation mechanism will be discussed. Transition states were not located, instead literature and other chemical precedents were used to rationalize which mechanism is most favorable.

1.4.1 Cyclohexane Dehydrogenation Mechanism

Fig. 1.4.1 shows the reaction energy profile of cyclohexane dehydrogenation calculated by DFTB as implemented in AMS. Cyclohexane initially coordinates to the TiS_2 sheet via interaction of a H-atom to an edge-based Ti-atom in **B**, resulting in an elongation of the C–H bond from 1.095 Å to 1.132 Å, shown in Fig. 1.4.2. This coincides with an interaction energy of –10.6 kcal/mol. Further C–H activation yields adduct **C**, which is more stable than **B** by 3.6 kcal/mol, at –14.2 kcal/mol. This is in stark contrast with the findings by Marks and coworkers, who found that the initial C–H activation of methane corresponds to a reaction energy of +3.6 kcal/mol. This addition was also calculated to have an activation barrier of 61.9 kcal/mol.[23] The C–H bond of methane is known to be the strongest bond amongst the hydrocarbons. This could explain why the addition of cyclohexane to the TiS_2 nanosheet leads to a more stable product. Furthermore, although a transition state was not located in this investigation, it is likely that the C–H activation barrier of cyclohexane is lower than that of methane.
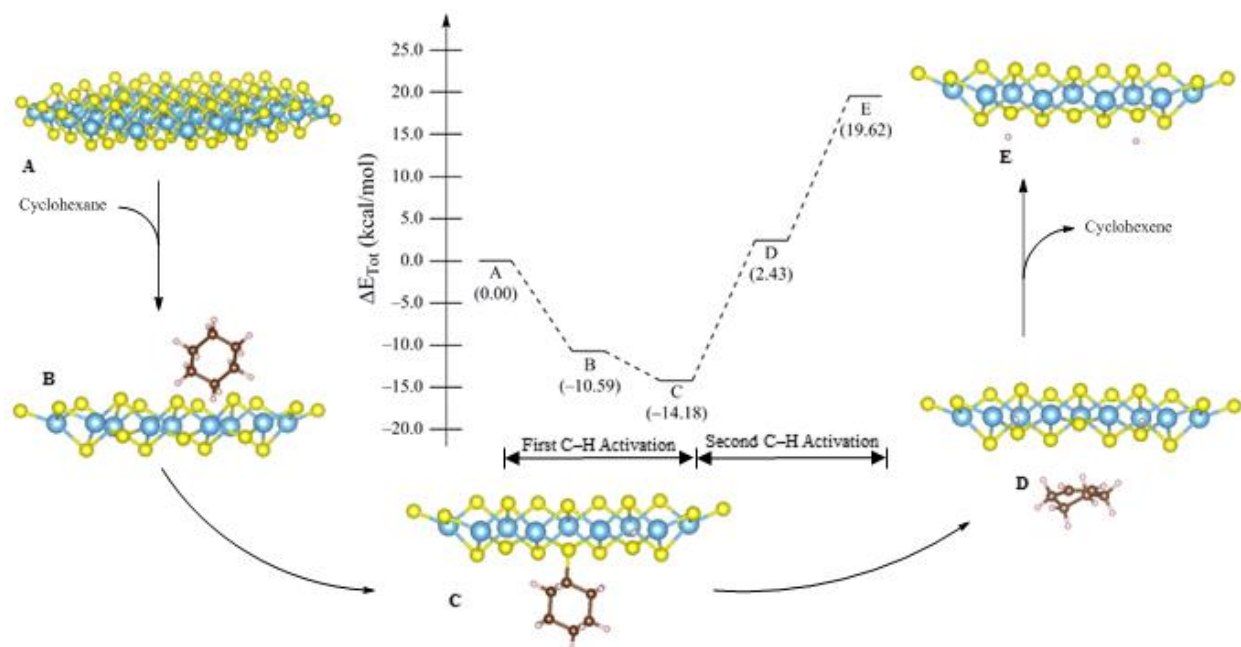

Fig. 1.4.1. The reaction energy profile of cyclohexane dehydrogenation on a 1T-TiS_2 hexagonal nanosheet with ZZ1 edge. The full nanosheet is shown in **A**, but for the other geometries only the first two rows of titanium on the edge where the reaction took place, are shown for clarity. Titanium = light blue; sulfur = yellow; brown = carbon; white = hydrogen.
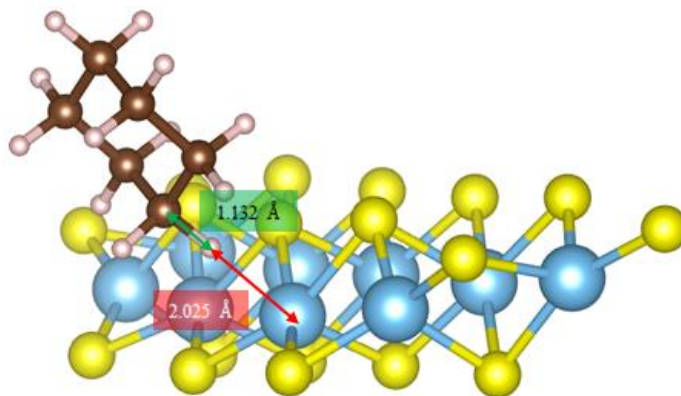
Fig. 1.4.2. C—H bond length and H···Ti distance after coordination of cyclohexane to the 1T—TiS$_2$ nanosheet in **B**, with ΔE_{Tot} = –10.59 kcal/mol. Titanium = light blue; sulfur = yellow; brown = carbon; white = hydrogen.

The second dehydrogenation step was found to be comparatively unfavorable. The thiirane intermediate proposed by Marks and coworkers[23] was found to be highly unfavorable for cyclohexene, shown in Fig. S1.1, at 41.2 kcal/mol. Instead direct release of cyclohexene is likely more favorable for this compound. Therefore, intermediate **D**, with dissociated cyclohexene, was located. The formation of this intermediate is associated with an increase in energy of 16.6 kcal/mol, increasing the energy of **D** to ΔE_{Tot} = 2.4 kcal/mol. Interestingly, the C═C bond in **D** is 1.327 Å, which is shorter than the normal cyclohexane C═C bond at 1.366 Å, by approximately 0.03 Å. While this is not a dramatic change in bond length, it is noteworthy. The reason for the C═C bond shortening remains, as of yet, unknown.

The reaction energy of the final step, cyclohexene elimination affording **E**, was 17.2 kcal/mol, increasing the ΔE_{Tot} to 19.62 kcal/mol. It is well established that cyclohexene is comparatively less stable than cyclohexane. For example, during benzene hydrogenation almost only the fully hydrogenated cyclohexene is observed as the product, and not the partly hydrogenated cyclohexadiene or cyclohexene.[49] Similar observations are made for cyclohexane dehydrogenation on other catalysts.[50] Currently, cyclohexene is commercially produced by Asahi with a Ru–Zn/SiO$_2$ catalyst from benzene hydrogenation;[51] however, this process suffers both from poor yield and poor selectivity, indicating the difficulties of cyclohexene synthesis. It should, therefore, not be surprising that formation of cyclohexene is energetically unfavorable.

In the second C–H activation step the hydrogen was assumed to be adsorbed on another edge-based S-atom than in the first C–H activation step. Conceivably, the second C–H activation step may occur on the same S-atom, directly followed by H$_2$S elimination. H$_2$S production was observed in several experimental investigations on alkane C–H activation on TMDs,[23,28] and may act as a driving

force for the reaction, as H_2S gas production would be entropically favorable. This mechanism was also considered and is shown in the supporting information (Fig. S1.2). Contrary to expectations, however, the release of H_2S results in a sharp increase in the reaction energy of 46.3 kcal/mol. Comparison of the TiS_2 nanosheet before and after H_2S elimination reveals that the TiS_2 nanosheet is strongly destabilized by the removal of a S-atom from the edge. The final product **E**, neglecting H_2S formation, is more stable than final product **G'**, including H_2S formation, by 46.3 kcal/mol. The calculated 1T-TiS_2 edge structure stability already hinted at this, as the ZZ0 edge, containing bare Ti-edge sites, is one of the least stable edge structures, as shown in Fig. 1.2.2.[23,36] This result does not necessarily question the H_2S formation observed in experiments; there could simply be a different mechanism in place leading to H_2S production. Furthermore, addition of elemental sulfur, as mentioned in ref. 23, could drive the release of H_2S from the 1T-TiS_2 edge. Further investigations would be necessary to determine this; however, this was outside of the scope of this research.

1.4.2 Butane Dehydrogenation Mechanism

The reaction energy profile of *n*-butane dehydrogenation is presented in Fig. 1.4.3., showing both the formation of 1-butene and 2-butane. The butane initially coordinates to the edge-based Ti-atom of the TiS_2 nanosheet edge through the C2–H bond in **2**, elongating the bond from 1.095 Å to 1.134 Å, as shown in Fig. 1.4.4. Then, either C1–H activation or C2–H activation can take place to form the butane adducts **3** and **3'**, respectively. Considering that butane interacts with the TiS_2 nanosheet via the C2–H bond, this activation may be easier than C1–H activation. Nevertheless, the reaction energy for **3** is –12.7 kcal/mol, while that for **3'** is –12.0 kcal/mol. This indicates that there is no significant thermodynamic preference for any adduct. Instead, the activation barrier for formation of **3'** may be lower than the activation barrier for **3**, due to the coordination of butane to the nanosheet via the C2–H bond. In order to conclusively determine this, the related transition states should be located and compared. Unfortunately, that was not possible during this investigation.
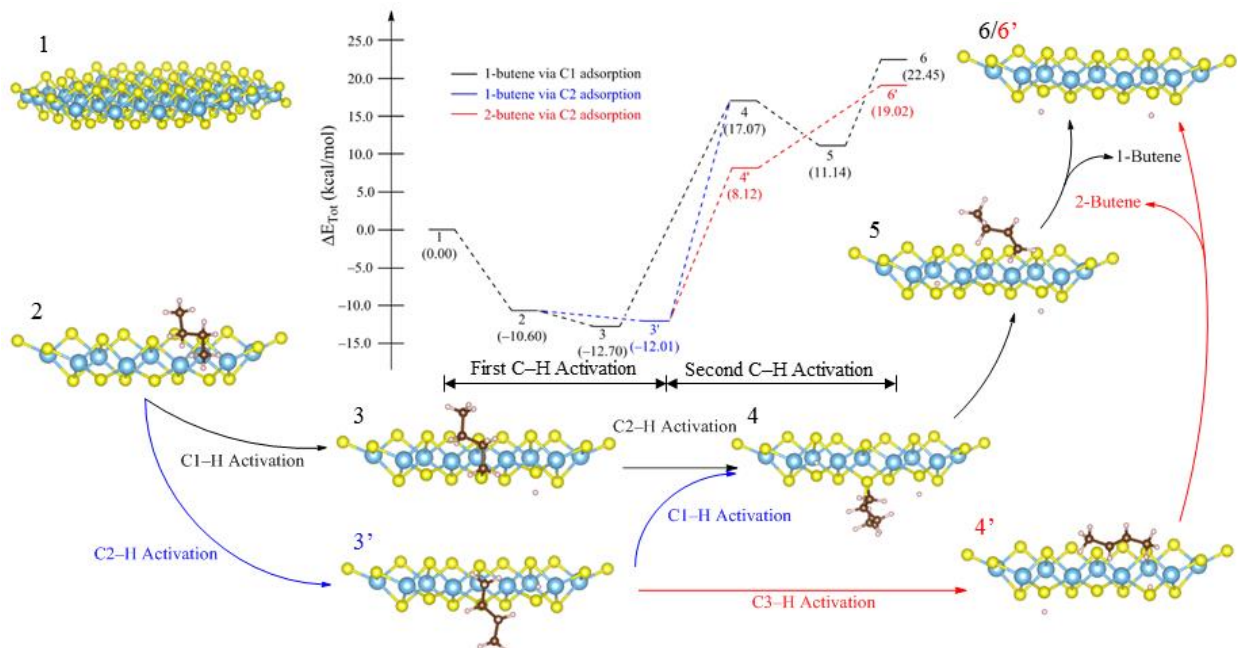
Fig. 1.4.3. The reaction energy profile of butane dehydrogenation on the 1T-TiS$_2$ nanosheet with ZZ1 edge. The full nanosheet is shown in **1**, while only the first two titanium rows on the edge where the reaction takes place, are shown in the other structures for clarity. Titanium = light blue; sulfur = yellow; brown = carbon; white = hydrogen.
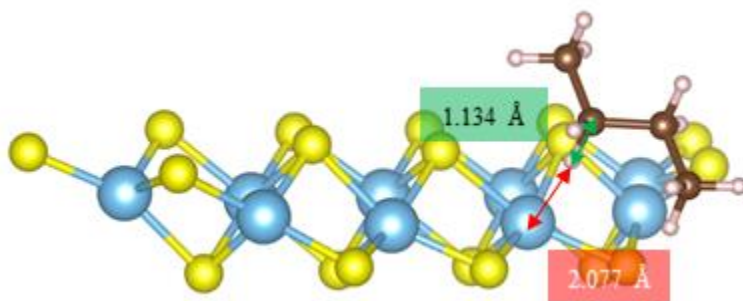
Fig. 1.4.4. C–H bond length and H···Ti distance after coordination of *n*-butane to the 1T-TiS$_2$ nanosheet in **2**, with ΔE_{Tot} = –10.60 kcal/mol. Titanium = light blue; sulfur = yellow; brown = carbon; white = hydrogen.

The second dehydrogenation step from **3** occurs via C2–H activation, affording thiirane intermediate **4** with an increase in energy of 29.8 kcal/mol. Intermediate **4** can also be accessed by **3'** via C1–H activation, coinciding with an energy increase of 29.1 kcal/mol. This is an unexpectedly high energy difference, likely also coinciding with a high energy barrier. The thiirane intermediate **4** is a sterically highly strained conformation, likely contributing to this steep energy increase. A more stable intermediate can be formed by C3–H activation from **3'**, affording **4'** with corresponding increase in energy of 20.1 kcal/mol. This intermediate affords 2-butene directly, without the formation of a thiirane intermediate, explaining the relative stability. An attempt at locating the corresponding thiirane intermediate proved unsuccessful, the resulting geometry of which is shown

18

in Fig. S1.3, and the intermediate was not considered in the final mechanism. The reason why this thiirane is not formed remains unclear.

The formation of the thiirane intermediate **4** seems to be a crucial step in the second C–H activation, yet there are C–H activations occurring on other C-positions imaginable, that may be associated with both lower activation barriers, as well as lower intermediates. This could be, for example, C3–H activation and C4–H activation from **3**, resulting in the corresponding 2-methylthietane and tetrahydrothiophene intermediates shown in Fig. 1.4.5c) and d), respectively. Both of these structures are more stable than thiirane intermediate **4** shown in Fig. 1.4.5a) by –3.1 and –14.1 kcal/mol, respectively. These intermediates, however, would not lead to stable products compared to intermediate **4**. A cyclopropane or cyclobutane would be formed, which are highly strained compounds that are unlikely to be stable compared to 1-butene or 2-butene. Therefore, the formation of these products is not considered likely.
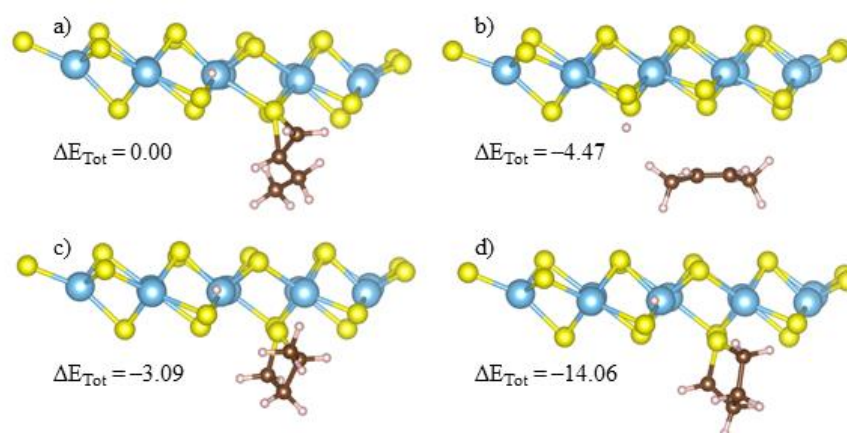
Fig. 1.4.5. The possible heterocycle intermediates afforded after C–H activation from **3**, where a) the expected thiirane intermediate **4** in 1-butene formation, b) the directly dissociated intermediate **4'** in 2-butene formation, c) a 2-methylthietane intermediate afforded after C3–H activation from **3** and d) a tetrahydrothiophene intermediate afforded after C4–H activation from **3**. ΔE_{Tot} in kcal/mol. Titanium = light blue; sulfur = yellow; brown = carbon; white = hydrogen.

Finally, 1-butene dissociates from the TiS_2 edge, allowing the energy to decrease by almost 6 kcal/mol. There appears to be an interaction between 1-butene and the TiS_2 nanosheet. Complete dissociation causes the energy to increase again to 22.5 kcal/mol in **6**, an increase of 11.3 kcal/mol relative to **5**, which is the interaction energy. This is also the case for **4'** and **6'**, which show an increase in energy from 8.1 kcal/mol to 19.0 kcal/mol, corresponding to an interaction energy of 10.9 kcal/mol. This calculated interaction energy is likely an artefact of the calculations being performed

under vacuum. The observed interaction between the 1T-TiS$_2$ sheet and the dissociated butene in **4'** and **5** may disappear when a solvent is added to the nanosheet during the calculation.

The mechanism including H$_2$S production was also analyzed for butane dehydrogenation and is shown in the appendix in Fig. S1.4. Again, the products of this pathway, **7** and **7'**, are significantly destabilized compared to the mechanism shown in Fig. 1.4.3, by 46.3 kcal/mol. This is exactly the same as the destabilization afforded to the cyclohexane dehydrogenation mechanism for H$_2$S production shown in Fig. S1.2, further strengthening the aforementioned suspicion that the TiS2 nanosheet with one edge-based S-atom is responsible for the destabilization.

1.4.3. General Considerations

According to Marks and coworkers, C–H activation occurs over a S–S couple on the 1T-TiS$_2$ edge, whereby the hydrogen is adsorbed on one S-atom and the alkyl is adsorbed on the neighboring one.[23] This would be consistent with a radical pathway of C–H activation. It is also possible for C–H activation to occur on just one S-atom, in a similar fashion to the rebound mechanism.[39] These two modes of adsorption are shown in Fig. 1.4.6. Adsorption on the same S-atom has a higher energy than adsorption on two different S-atoms by 10.1 kcal/mol, clearly indicating that this adsorption mode is not feasible. One argument against the radical mechanism may be drawn from Fig. 1.4.2., where the C–H bond is shown to be elongated and pointing in the direction of an edge-based Ti-atom. This may indicate that titanium participates in C–H cleavage, perhaps via a heterolytic cleavage mechanism by abstracting a hydride. This mechanism is not further explored here, however, as it is not supported by literature.[23,28] Furthermore, the observed H$_2$S production during experimental work, would suggest that the H-atoms are in fact adsorbed on the edge-based S-atoms.

It is not unimaginable that the edge-based S-atoms alone function to homolytically cleave the C–H bond. In TiS$_2$, as in TiO$_2$, the Ti-atoms are in an extremely electron-poor state, having an oxidation state of 4+ and no d-electrons. While the Ti(IV) state is very stable, the Ti-atoms are likely pulling electron density from the electron rich S^{2-}-atoms. This could give the edge-based S-atoms some radical character. In order to verify if this is the case, single point calculations were performed in the Jaguar 9.1 suite of modeling programs to find the spin densities on the 1T-TiS$_2$ model nanosheet. Unfortunately, the calculations were not completed at the time of finishing this work.
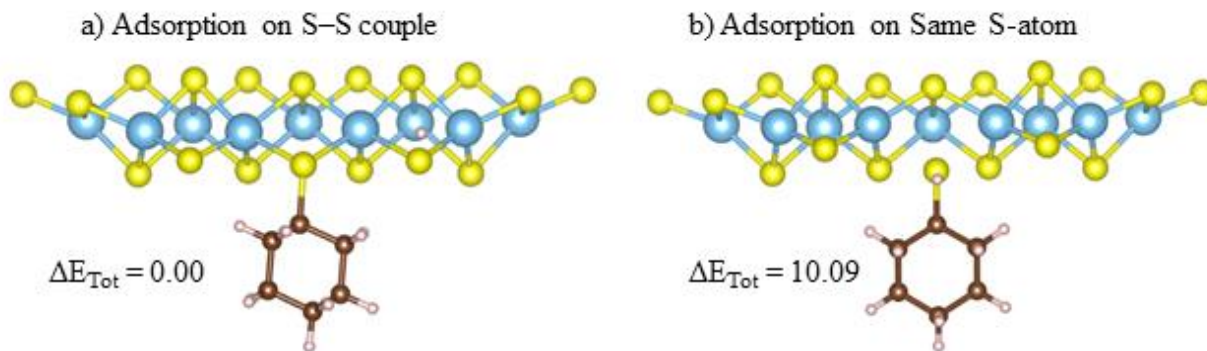
Fig. 1.4.6. Comparison of the products of C–H activation via a) the radical mechanism, and b) the rebound mechanism. ΔE_{Tot} is given in kcal/mol. Titanium = light blue; sulfur = yellow; brown = carbon; white = hydrogen.

The initial C–H activation step for both cyclohexane and *n*-butane dehydrogenation was found to be surprisingly favorable, compared to literature.[23] This may, however, simply be an artefact of the calculation. The calculations were performed in vacuum, rendering the TiS$_2$ nanosheet in a kind of "activated state". During reaction in experimental conditions, the nanosheet would be placed in a solvent or surrounded by a gas. Solvation may give rise to thermodynamically favorable interactions, resulting in a stabilization of the solute, in this case the 1T-TiS$_2$ nanosheet. Therefore, while the current results show a reaction energy of –14.2 kcal/mol in vacuum for **C** formation, adding a solvent may stabilize the bare TiS2 sheet to be more stable than **C**. Similarly, the observed interactions in **B** and **D** may be less significant, due to the TiS$_2$ surface being covered by solvent molecules. The same thing can be said for the dehydrogenation mechanism of *n*-butane.

There are methods to model a solvent: explicitly modeling the solvent by placing solvent molecules around the nanosheet, or implicitly by applying a continuum dielectric.[52] Unfortunately, explicitly modeling the solvent is computationally expensive and requires boundary conditions, which were not applied in the calculations presented here. The implicit solvation model is vastly more efficient than the explicit model, however it is not available in DFTB.[53] Using another computational method, such as VASP or Jaguar 9.1, may provide a solution. This was, however, outside of the scope of this investigation. Nevertheless, it is important to keep these effects in mind when considering the implications of these results. While they may provide an initial understanding of the investigated system, and indicate the feasibility of achieving cyclohexane and *n*-butane dehydrogenation catalyzed by a 1T-TiS$_2$ nanosheet, a model system in vacuum will never fully approximate the experimental results.

The alkene formation in both mechanisms discussed above are accompanied by large reaction energies around 20 kcal/mol. Employing mild conditions in this reaction, as was suggested

to be possible in ref. 11, is unlikely to afford high yields in this system. In fact, Marks and coworkers report the reaction of methane C–H activation taking place at over 1200 K,[23] and Shan and coworkers heat the reaction set-up to more than 800 K to dehydrogenate isobutane over TMDs.[28] Under such reaction conditions, the above mechanism is much more likely to be achieved.

1.5 Conclusion & Outlook

In summary, the possibility of performing cyclohexane and *n*-butane dehydrogenation on a 1T-TiS$_2$ nanosheet were explored with Density Functional Tight-Binding by exploring the energetics of the potential reaction pathways. Initial C–H activation was found to be most favorable on an S–S couple on the TiS$_2$ edge. Subsequently, a second C–H activation takes place on the neighboring C-atom, directly affording the alkene in the case of cyclohexene and 2-butene, but resulting in a thiirane intermediate for the formation of 1-butane. Production of H$_2$S was found to be unfavorable due to the instability that is afforded to the 1T-TiS$_2$ nanosheet after removal of an edge-based S-atom. C–H activation on TiS$_2$ is thought to occur via the homolytic or radical pathway, but further investigation is required to confirm this. This can be investigated, for example, by calculating the spin densities on the edge-based S- and Ti-atoms. Since the calculations were performed in vacuum, solvation effects are not considered in this work. Future investigations may benefit from including solvent effects, to obtain energies that are more accurate to experimental measurements. To our knowledge there is no known experimental literature investigating the dehydrogenation of linear or cyclic alkanes in TiS$_2$; therefore, this work may provide a guideline to future attempts at performing this reaction experimentally or studying it computationally.

In this study, transition states were not located with DFTB. In order to gain a better understanding of the feasibility of these reactions, using a different method to locate transition states, such as the Nudged Elastic Band method, could provide useful insights. Furthermore, employing computational methods such as the Vienna Ab initio Simulation Package, which is known to be more accurate than DFTB, could improve the results obtained in this study.

Future investigations could focus on the activation of the basal plane of TiS$_2$, as mentioned in the introduction. Since layered TMDs such as TiS$_2$ are known to be active only on the edge sites, activating the basal plane could improve the activity of the nanosheet catalyst. Other modifications of the nanosheet, such as oxidation of the edges to form a TiO$_2$/TiS$_2$ are known to impact the electrochemical properties of the nanosheet. The impact of such modifications on the

dehydrogenation of linear and cyclic alkanes could also be of interest. Using these two modifications in tandem, may be able to improve not only the activity of the TiS_2 nanosheet, but also the selectivity.

2. The Electronic Structure of β-Diketiminate Manganese Hydride Dimer

2.1 Introduction

Low-coordinate transition metal complexes have been extensively studied due to the reactivity enabled by their coordinatively and electronically unsaturated structures.[54] It has been widely acknowledged that bulky ligands can stabilize low-coordinate electron-deficient complexes by preventing aggregation.[55] One ubiquitous group of bulky ligands that support electron-deficient metal centers is the β-diketiminate ligand, commonly abbreviated as BDI or nacnac. Practical advantages such as facile synthesis and modification[56] enable systematic studies on β-diketiminate ligands.[57,58] For instance, the Mindiola group reported catalytic carboamination with a titanium complex supported by a β-diketiminate ligand.[59] The Holland group also reported a Fe(II) fluoride β-diketiminate complex that catalyzes the hydrodefluorination of fluorocarbons.[60] Despite extensive investigation on transition metal complexes supported by β-diketiminate ligands, (BDI)Mn complexes have only recently been found to exhibit catalytic activity. Notably, the bridging hydride dimer, [(2,6-*i*Pr2PhBDI)Mn(μ-H)]2 (**1**), has been structurally characterized and found to catalyze the hydrosilylation of alkenes.[1]

Intuitively, one can argue that complex **1**, which has 13 electrons per metal center, would prefer to engage in metal–metal bonding to compensate for its electron deficiency, as shown in Fig. 2.1.1. The existence of a metal–metal triple bond would formally provide three additional electrons to each Mn center, discounting expected weak δ-interactions, leading to a more reasonable electron count of 16. Few dimeric β-diketiminate manganese complexes have been reported;[61–63] however, a detailed analysis of their electronic structures has yet to be reported. In this contribution, the bond orders between the Mn centers of **1** and related complexes featuring bridging p-block elements are explored using a combination of computational and experimental techniques. Given that the coordinatively- and electronically-unsaturated nature of (BDI)Mn complexes has rendered them capable of catalyzing hydrofunctionalization reactions, a main goal of this research was to evaluate the electronic structure of **1** to disclose the origin of its catalytic activity.
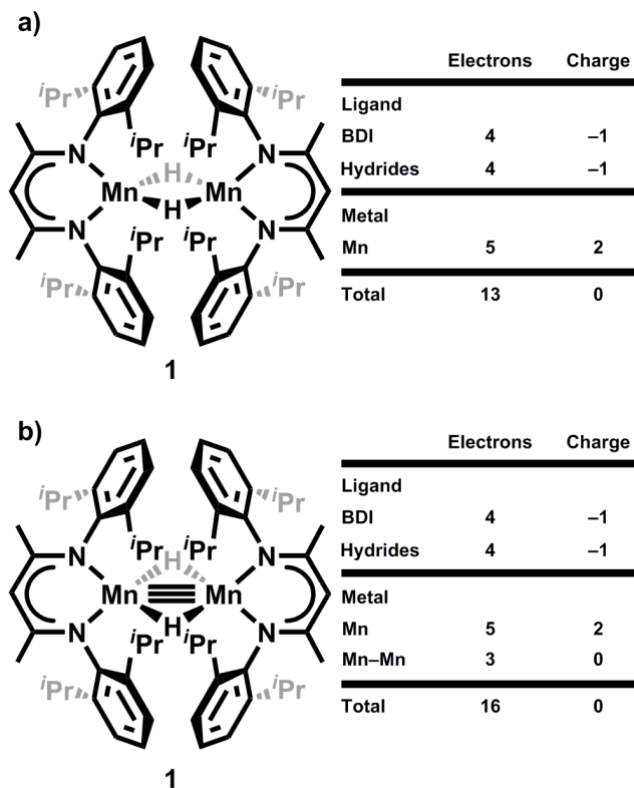
Fig. 2.1.1. Electron-count diagrams of a) **1** excluding metal–metal bonding and b) **1** including a triple bond between the manganese centers.

2.2 Computational Details

All calculations were performed using density functional theory (DFT) as implemented in the Jaguar 9.1 suite of ab initio quantum chemistry programs.[64] The B3LYP functional[65,66] with Grimme's D3[67] dispersion correction (B3LYP-D3) was exploited as the standard, together with the 6-31G** basis set for geometry optimizations. The Los Alamos LACVP** basis including relativistic effective core potential was used to represent manganese.[68–70] In order to obtain more reliable energies, single-point calculations were performed on the optimized geometries using Dunning's correlation-consistent triple-ζ cc-pVTZ(-f) basis set for main group elements and LACV3P** for manganese.[71] The zero-point energy (ZPE), entropic and solvation contributions to the Gibbs energy are obtained from the same level of theory as the geometry optimizations (B3LYP-D3/6-31G**/LACVP**). Energy decomposition was computed with the B3LYP-D3 functional using the Amsterdam Density Functional (ADF 2019) package.[72] The optimized geometries were confirmed to be the local minima on the potential energy surfaces by showing the absence of an imaginary frequency. The solvation calculations utilized self-consistent reaction field (SCRF) approach on the gas phase geometry to model the solvation shell of dielectric constants ε = 2.284 for benzene and ε = 2.397 for toluene. As is

the case for all continuum models, the solvation energies are subject to empirical parametrization of the atomic radii that are used to generate the solute surface.[73] We employed the standard set of optimized radii in Jaguar for H (1.150 Å), C(1.900 Å), N(1.600 Å), O(1.600 Å), F(1.682 Å) and Mn(1.480 Å).

The energy components have been computed with the following protocol. The free energy in solution phase G(sol) has been calculated as follows:

$$G(sol) = G(gas) + Gsolv \tag{2.1}$$

$$G(gas) = H(gas) - TS(gas) \tag{2.2}$$

$$H(gas) = E(SCF) + ZPE \tag{2.3}$$

$$\Delta E(SCF) = \Sigma E(SCF) \text{ for products} - \Sigma E(SCF) \text{ for reactants} \tag{2.4}$$

$$\Delta G(sol) = \Sigma G(sol) \text{ for products} - \Sigma G(sol) \text{ for reactants} \tag{2.5}$$

G(gas) is the gas phase free energy; G(solv) is the free energy of solvation; H(gas) is the gas phase enthalpy; T is the temperature (298.15 K); S(gas) is the gas phase entropy; E(SCF) is the electronic energy derived from the SCF method and ZPE is the zero-point energy.

In principle, multi-reference methods such as CASSCF are required to describe rigorously an antiferromagnetically coupled spin state of the dimer, which is impracticable for systems of this size because of computational demands. In practice, Noodleman's broken symmetry (BS) approach,[74] which makes use of the Heisenberg spin operator formalism to obtain a reasonable electronic structure description of transition metal dimers, provides a working protocol for single reference methods such as DFT employing the unrestricted spin formalism. We closely followed the protocol described elsewhere[75] to obtain the BS orbitals and used the unrestricted spin formalism in all calculations. Essentially, the valence bond descriptions of the molecules were used as initial guesses to generate a molecular wavefunction in terms of localized orbitals that undergo the SCF procedure. The large number of unpaired electrons at the manganese core and the intrinsic electronic flexibility of the transition metals give rise to a number of energetically similar electronic states. Therefore, we used spin densities derived from Mulliken population analysis that have also been employed in many previous studies[75] to confirm that the correct, or at least a reasonable, electronic state had been reproduced.

2.3 Results & Discussion

2.3.1 MO-Diagrams of Ferromagnetically and Antiferromagnetically coupled 1

In order to gain an initial understanding of the electronic structure of **1**, conceptual MO diagrams were constructed (Fig. 2.3.1). Fig. 2.3.1a depicts the MO diagram of $\{[(_{2,6\text{-}i\text{Pr2Ph}}\text{BDI})\text{Mn}]_2\}^{2+}$, which lacks bridging hydride ligands. The in-phase d_{xy}, d_{xz} and $d_{x^2-y^2}$ orbital combinations could interact to form the expected Mn–Mn triple bond based on the electron count. The apparent non-bonding orbitals, the bonding and antibonding combinations of the d_{z^2} and d_{yz} orbitals, are expected to be nearly degenerate, giving rise to four unpaired electrons. This diagram forms the basis of the conceptual molecular orbital diagram of **1**, which is shown in Fig. 2.3.1b. For **1**, the in-phase combination of the d_{xy} orbitals is expected to interact with the out-of-phase combination of the hydride s-orbitals. After taking the bridging hydride ligands into account, four unpaired electrons remain in the weakly interacting d_{z^2} and d_{yz} orbitals. Importantly, the frontier molecular orbital diagram in Fig. 2.3.1b is consistent with the previously reported solution magnetic susceptibility of **1** (5.2 μ_B at 298 K).[1] The electrons initially expected to contribute to a bonding interaction between the metal centers, as shown in Fig. 2.3.1a, are instead redistributed into Mn–H bonds via a σ-bonding as illustrated in Fig. 2.3.1b. This σ-bonding interaction is speculated to reduce the bond order between the two manganese centers to be between 2 and 3. The crystal structure of **1**, however, reveals a Mn–Mn distance of 2.814 Å, which is significantly longer than the bond length expected for a Mn–Mn triple bond.[76,77] Manganese dimers reported to feature Mn–Mn triple bonds are known to possess Mn–Mn distances of approximately 2.2 Å,[78,79] suggesting that the bond order between the Mn centers of **1** is considerably lower than 3.
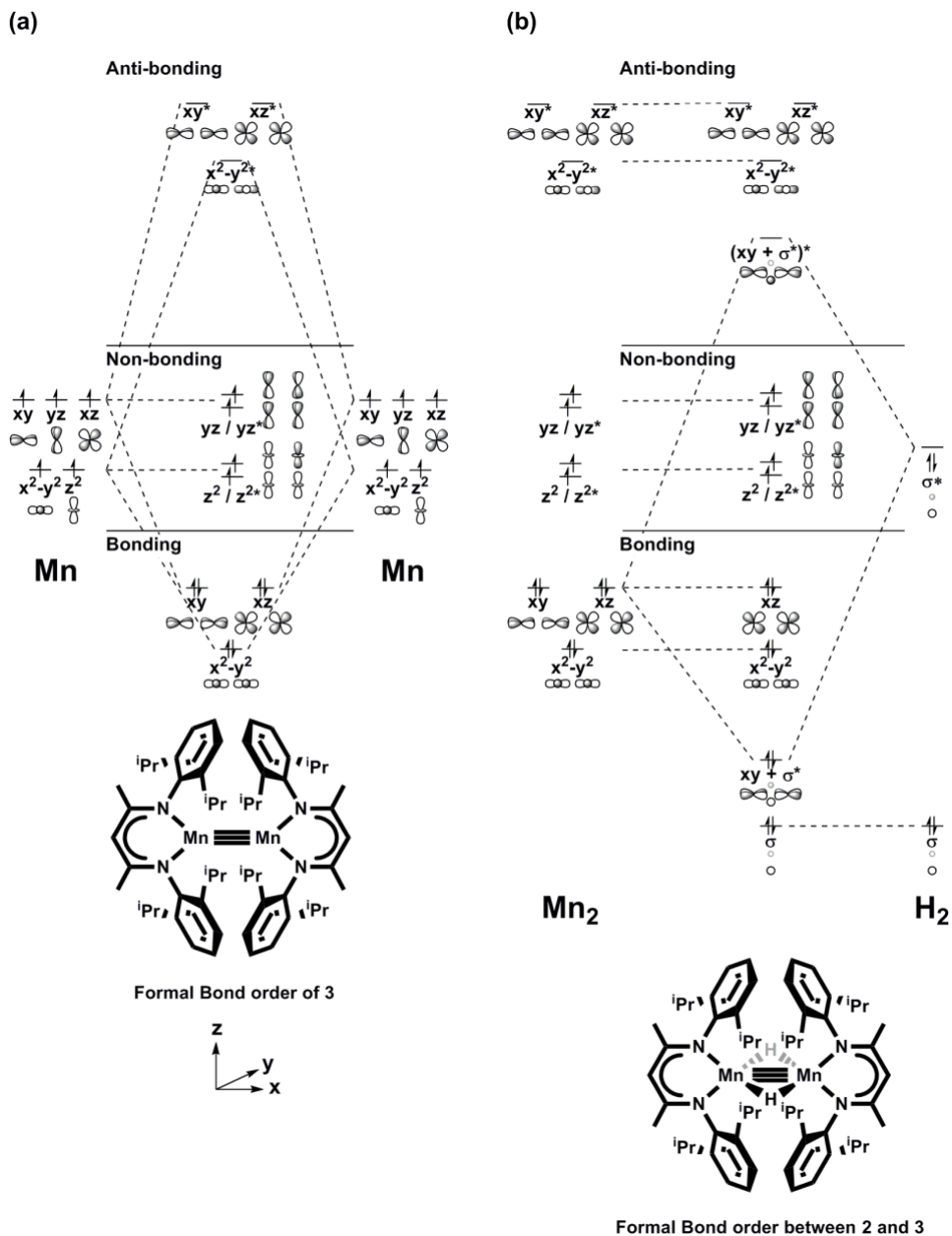
Fig. 2.3.1. Conceptual MO diagrams for a) $\{[(_{2,6\text{-}i\text{Pr2Ph}}BDI)Mn]_2\}_{2+}$ and b) **1**, which features an interaction between the out-of-phase hydride combination and the in-phase d$_{xy}$ orbital combination.

It must be mentioned that the neutral analogue of $\{[(_{2,6\text{-}i\text{Pr2Ph}}BDI)Mn]_2\}_{2+}$, $[(_{2,6\text{-}i\text{Pr2Ph}}BDI)Mn]_2$, was reported by Roesky et al. in 2005 (Fig. 2.3.2).[62] Notably, single crystal X-ray diffraction analysis revealed that $[(_{2,6\text{-}i\text{Pr2Ph}}BDI)Mn]_2$ features staggered BDI ligands and a Mn–Mn distance of 2.721 Å. This distance is shorter than the same distance in **1** (2.814 Å), but still considerably longer than what would be expected for a complex featuring a Mn–Mn triple bond. The contraction of the distance between metal centers was reported to attribute to a bonding interaction between 4s orbitals in metal centers. Instead of having a 3d_6 configuration, the Mn(I) centers adopt a 4$s_1$3d_5 configuration;

28

therefore, two 4s orbitals from each metal center can form an in-phase combination. Further information about the ground state and magnetism of [(2,6-*i*Pr2PhBDI)Mn]2 was gathered by DFT analysis;[62] however, this compound's absence of Mn–Mn multiple bonding had not been investigated.
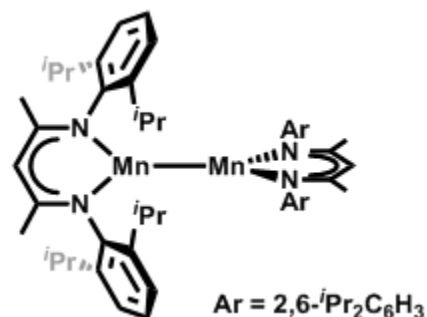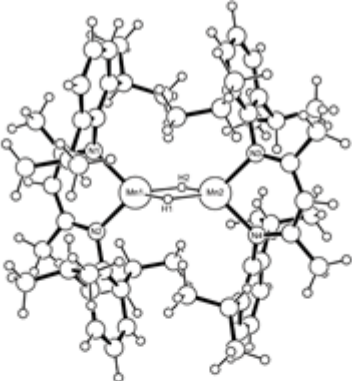
Fig. 2.3.2. The dimeric manganese complex, [(2,6-*i*Pr2PhBDI)Mn]2, reported by Roesky et al.

The X-band (9.4 GHz) electron paramagnetic resonance (EPR) spectrum of **1** was reported in 2018.[1] At 106 K, a superposition of three spin states, S = 1, S = 2 and S = 3, was observed. The spectral analysis via computer simulation showed that the two Mn(II) centers are high spin and are antiferromagnetically coupled with each other. Likewise, we have found the S = 0 state to be the ground state and the electronic energy of the S = 5 state is higher than that of the S = 0 state by 0.9 kcal/mol, implying that the F-coupled state is accessible. Consequently, the spin states in between the two extreme states, S = 1, S = 2, S = 3 and S = 4 states, can be accessed as well at the EPR condition and a certain temperature. Considering the ambient temperature solution magnetic susceptibility data collected for **1** (5.2 μ_B), the observed S = 2 spin state is also the ensemble average value of all possible states accessible at room temperature. Therefore, computational models with ferromagnetic (**1-F**) and antiferromagnetic coupling (**1-AF**) between the metal centers, representing the extreme states, were selected to evaluate.

The optimized geometries of **1-F** and **1-AF** are in good agreement with the crystal structure (**1-CS**), as shown in Table 2.3.1. The computed Mn–Mn distances are 2.871 Å for both **1-F** and **1-AF** cases, which is comparable to that of the crystal structure, 2.814 Å. The tetrahedral-like geometry around the Mn centers and the eclipsed positioning of the β-diketiminate ligands were clearly reproduced. Fig. 2.3.3 shows the structural consistency among the X-ray crystallographic data and the optimized geometries of **1-F** and **1-AF**. The absence of a multiple bond between the manganese centers was observed, with Mayer bond orders of 0.21 and 0.27 for **1-F** and **1-AF**, respectively.

Table 2.3.1. Optimized structural parameters of the dimanganese complexes **1-F**, **1-AF** and **1-CS**

	1-F	1-AF	1-CS
	calc.	calc.	exp.
Spin-Coupling	F	AF	–
Mn1–H1 (Å)	1.897	1.834	1.791
Mn1–H2 (Å)	1.919	1.923	1.938
Mn1–N1 (Å)	2.099	2.103	2.086
Mn1–N2 (Å)	2.116	2.110	2.098
∠H1–Mn1–N2 (°)	116.9	120.5	121.1
∠N2–Mn1–N1 (°)	90.1	90.5	91.5
∠N1–Mn1–H2 (°)	121.9	119.8	118.3
∠H2–Mn1–H1 (°)	82.2	80.5	82.1
τ_4 Mn1	0.86	0.85	0.85
Mn1–Mn2 (Å)	2.871	2.871	2.814
∠Mn1–H1–Mn2 (°)	97.5	99.6	97.9
Spin-Densities[a] Mn1	4.91	4.75	–
Spin-Densities[a] Mn2	4.91	−4.75	–
Mayer Bond Order for Mn–Mn	0.21	0.27	–
Relative E_{SCF}[b] (kcal mol^{-1})	0.90	0	–

[a]Mulliken spin-density.
[b]The relative energies (kcal mol^{-1}) are referenced to the AF-coupled state.
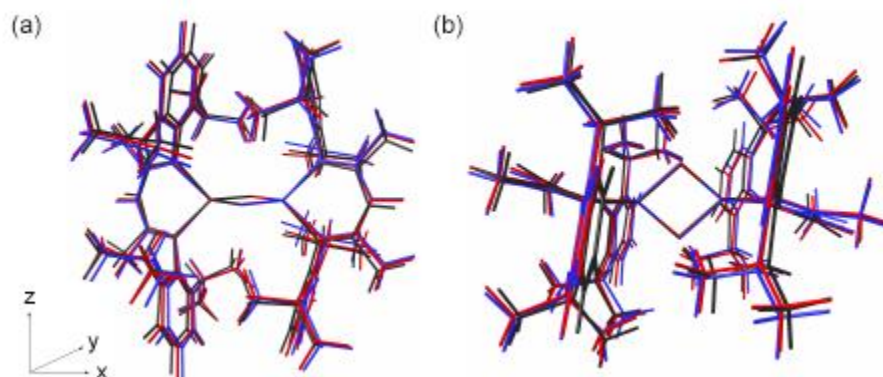
Fig. 2.3.3. Overlay of the structures of **1-CS** in black, **1-F** in blue, and **1-AF** in red: (a) the xz-plane view and (b) the orthogonal view along the z-axis.

To investigate the lack of a Mn–Mn multiple bond, the MO-diagrams of **1-F** and **1-AF**, shown in Fig. 2.3.4, were analyzed. The MO-diagrams were simplified by adopting a local D_{2h} symmetry. In total, 12 MOs comprising 10 metal-based orbitals and 2 hydride-based orbitals are presented. As expected, the in-phase combination of the d_{xy} orbitals interacts with the out-of-phase combination of

hydride orbitals to afford a bonding and antibonding combination for both **1-F** and **1-AF**. Furthermore, an interaction between the bonding combination of the d_{z^2} orbitals and the in-phase combination of hydride orbitals is observed, generating a low-lying bonding orbital and high-lying antibonding orbital.

The left-hand side of Fig. 2.3.5. illustrates the **1-F** MOs. The β-orbitals of **1-F** are higher in energy than the corresponding α-orbitals due to the absence of exchange interaction.[80,81] On the other hand, both spin orbitals are paired up in **1-AF**, with MOs derived from Noodleman's broken symmetry approach, shown on the right-hand side of Fig. 2.3.4. Interestingly, the metal d_{xz} orbitals are higher in energy than expected. Isosurface plots of the in-phase and out-of-phase combinations of the d_{xz} orbitals are shown in Fig. 2.3.5a for **1-F** and 2.4.5b for **1-AF**. The metal d_{xz} orbitals are mixed with ligand-based orbitals via σ-bonding. The ligand-based orbitals are antibonding with respect to the metal-based orbitals, destabilizing the MOs. The corresponding bonding combinations are much lower in energy, and not depicted.
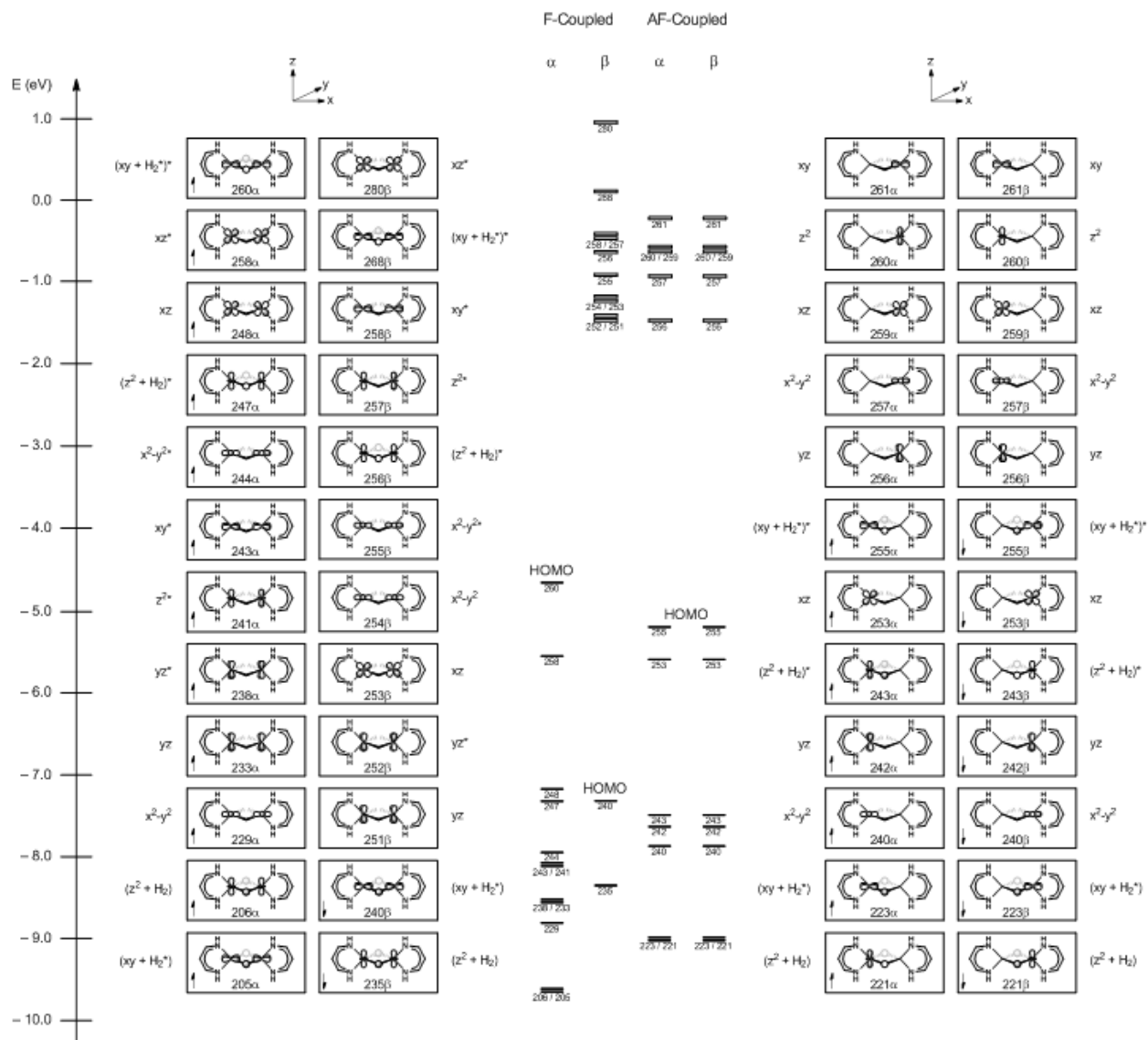
Fig. 2.3.4. MO-diagrams of ferro- (1-F) and antiferromagnetically-coupled (1-AF) Mn centers in 1.
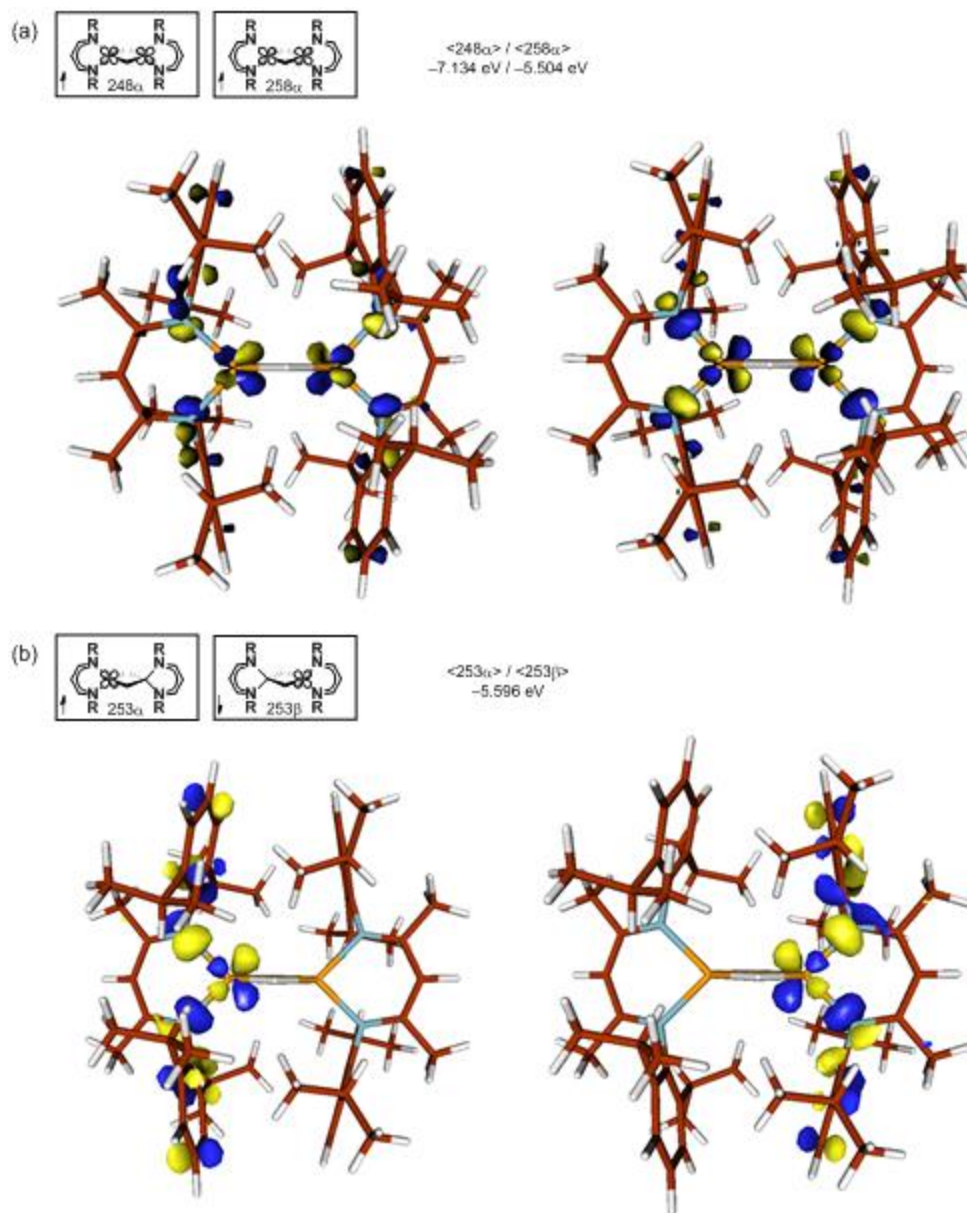
Fig. 2.3.5. Isosurface plots (isodensity = 0.05 au) of the metal d$_{xz}$-based MOs of **1**: a) metal–metal in-phase, and out-of-phase α-spin, **1-F** b) α-spin and β-spin, **1-AF**.

2.3.2 Determination of J_o for 1

According to Noodleman's description, the Heisenberg exchange coupling constant, J_o, can be directly calculated from the energy difference between a high-spin state and a broken symmetry state.[74] In the broken-symmetry approach, the energy difference between the high spin state and the broken symmetry state is:

$$E(S_{max}) - E(BS) = -S_{max}(S_{max} + 1) J_o \tag{2.6}$$

where S_{max} is the maximum number of unpaired electrons per monomeric unit. Here, each manganese center has five unpaired d-electrons; therefore, the high spin state is a sextet. The coupling constant is sensitive to the distance between metal centers, as well as the number of electrons shared by the metal centers. Therefore, probing J_o values will be the best way to assess the interaction between metal centers. Using equation (2.6) the Heisenberg exchange coupling constant was determined to be $J_o = -10.9$ cm^{-1}. This is lower by a factor 10 than the J_o-value determined by Roesky and co-workers, at -110 cm^{-1} using the B3LYP functional,[62] in which a Mn–Mn single bond is formed by the Mn-based 4s-orbitals. Jones and co-workers synthesized a similar compound, $(L*Mn)_2$ ($L*$ = -N(AR*)SiMe$_3$)), which also shows a single Mn–Mn bond arising from σ-interactions.[82] The calculated J_o-value was reported by the Jones' group to be -47.5 cm^{-1}, which is still significantly stronger than the one calculated here.

The Broken Symmetry approach does not distinguish between direct magnetic exchange interactions and indirect magnetic exchange interactions, such as superexchange. Bridging hydrides are capable of mediating strong superexchange interactions between metal centers due to the small size of the ion and the symmetry of the s-orbital. Calculating superexchange explicitly with DFT requires the use of a multi-reference calculation, such as Complete Active Space SCF (CASSCF),[83] which is computationally expensive for a complex of the size of **1**. Nevertheless, it is expected that the superexchange is at least partially responsible for the calculated J_o value.

With a computed J_o value in hand, attempts were made to determine this value experimentally using two complementary techniques by Professor Trovitch of Arizona State University and Professor John Anderson of the University of Chicago. In the initial contribution by Trovitch and coworkers, **1** was found to exhibit an ambient temperature magnetic moment of 5.2 μB at 298 K (Evans Method); however, variable temperature data had not been collected.[1] Therefore, a sample of **1** was analyzed by SQUID magnetometry between 1.8–300 K by Anderson and coworkers. At room temperature the xT value is 4.5 cm^{3}K/mol (6muB), which is significantly below the spin-only value for two noninteracting S = 5/2 Mn(II) centers (χT_{S0} = 8.75), indicating antiferromagnetic coupling between the Mn centers, a multiply-bonded complex with a lower overall spin state, or some intermediate case. Upon cooling, the χT of **1** decreases slightly, indicative of weak antiferromagnetic coupling (Fig. 2.3.6).
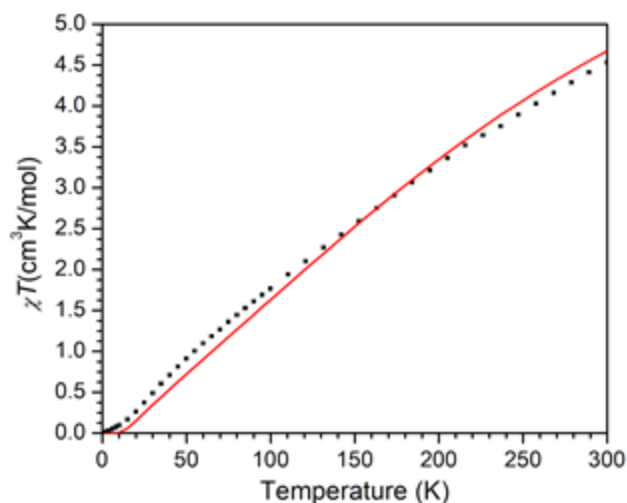
Fig. 2.3.6. Temperature-dependent χT vs. T data for **1** collected under an applied field of 0.1 T. The red line is the fit where g is fixed at 2.05, as outlined in the text. The measurements were performed by Professor Anderson and coworkers.

The data collected at 0.1 T was modeled using either the DAVE or PHI programs.[84,85] The two Mn centers of **1** were treated as isotropic, spin-only (S_{Mn} = 5/2) centers and presumed to be identical given their crystallographic equivalence. The best fit was acquired with a g-value of 1.82 (± 0.25) and an antiferromagnetic J_o coupling of –15 cm^{-1} (± 0.1 cm^{-1}, normalized to $2J_o$ convention). Constraining the fit to the g value of 2.05 previously determined by EPR spectroscopy resulted in a slightly poorer but still reasonable fit with J_o = –20 cm^{-1} (± 0.1 cm^{-1}). The value of g is within error in both fits, and either fit provides a consistent J_o value of –15 to –20 cm^{-1}.

To determine the isotropic exchange coupling, J_o, by X-band EPR spectroscopy, Trovitch and coworkers have carried out measurements of **1** at six different temperatures between 4 K and 106 K. Fig. 2.3.7a shows the temperature variation of the EPR intensity of the signals occurring around 180 mT (B_1) and 60 mT (B_2) (see Fig. 2.3.7b). The EPR signals at B_1 and B_2 belong to the S = 1 and S = 2 spin manifolds, respectively. They were identified by simultaneously simulating the EPR spectra of **1** at different temperatures. At 4 K (Fig. 2.3.7b), the spectrum was simulated considering a superposition of two spin manifolds, S = 1 and S = 2. The parameters used to fit the EPR spectra of **1** (see EPR spectroscopy section) were within experimental error of those reported earlier by Mukhopadhyay et al.[8] The value of J_o can be obtained by fitting the experimental data in Fig. 2.3.7a using equation (2.13) (see EPR spectroscopy section in the appendix), which accounts for the Boltzmann populations of the energy levels associated with the S = 0, S = 1, S = 2, S = 3, S = 4 and S = 5 spin manifolds. A value of –9.5 cm^{-1} was obtained when all data points were included in the fit. If

the data point corresponding to the EPR signal at B_1 and measured at 80 K is not included in the fit (see figure caption for details), a value of –10.8 cm^{-1} was obtained. Using the average of the two values, Trovitch and coworkers determined from the temperature dependence of the X-band EPR spectrum of **1** that J_o = –10.2 ± 0.7 cm^{-1}. Taken both SQUID and EPR data, our computational and the experimental efforts of Professors Trovitch and Anderson to determine J_o are consistent with weak antiferromagnetic coupling between the Mn centers of **1**.
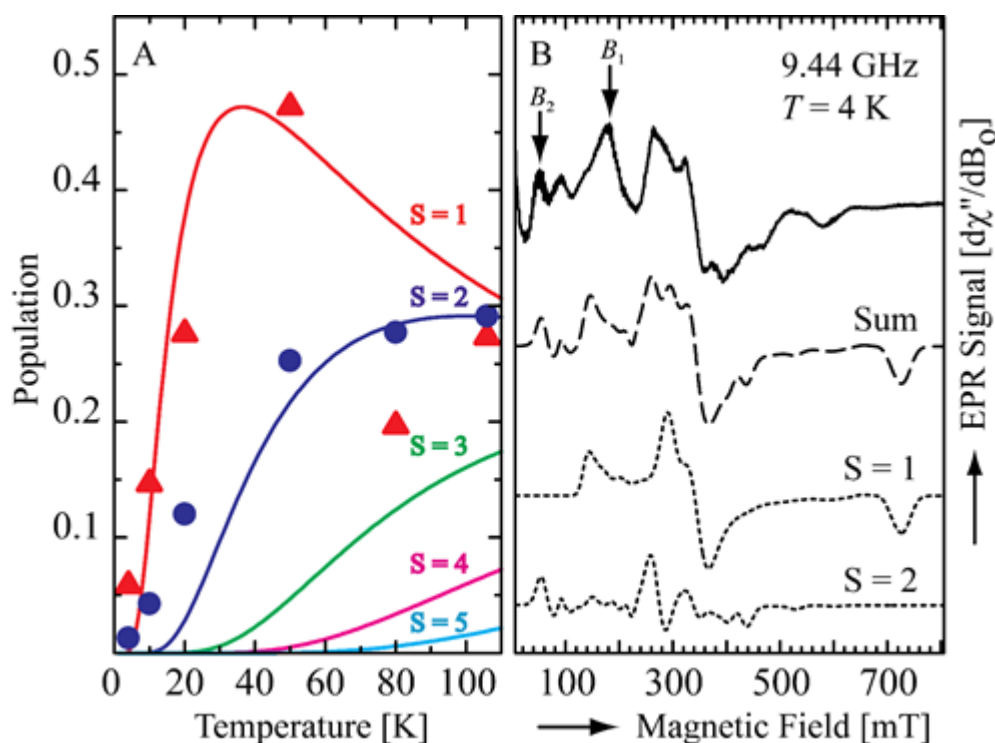
Fig. 2.3.7. a) Signal intensity times temperature as a function of temperature for the EPR signals around 180 mT (B_1) (red triangles) and 60 mT (B_2) (blue circles) present in the EPR spectra of **1**. Temperature dependence of Boltzman populations corresponding to S = 1 (red line), S = 2 (blue line), S = 3 (green line), S = 4 (magenta line) and S = 5 (cyan line) spin manifolds. These curves were calculated using Eq. 13 with the value of J_o that best fit the available experimental data. It can be noticed that the population corresponding to the EPR signal at B_1 and measured at 80 K deviates significantly from the fit. b) The X-band EPR spectrum of **1** at 4 K. The solid line is the experimental spectrum, and the dashed line is the sum of the simulated spectra for S = 1 and S = 2 dimer spin states (dotted lines). The EPR signals marked with arrows as B_1 and B_2 were identified as originating from the S = 1 and S = 2 dimer spin states, respectively. This spectrum did not show well-resolved 55Mn hyperfine couplings. However, multiline patterns corresponding to the hyperfine couplings (~3.6 mT) of two equivalent Mn(II) ions were observed in the EPR spectrum at 20 K (not shown). The measurements were performed by Professor Trovitch and coworkers.

2.3.3 Influence of Steric Bulk

We initially hypothesized that the sterically bulky β-diketiminate ligands preclude the formation of a metal–metal multiple bond as described in the literature.[1,62,77,82] Bulky groups attached

to the β-diketiminate ligand may sterically prohibit the proximal positioning of two metal centers, despite the metal centers being within the range for interaction.[86] In this regard, the lower than anticipated bond order between the metal centers was proposed to be attributed to steric hindrance in bulky β-diketiminate ligands. To validate this proposition, a model compound supported by the most sterically simplified version of the β-diketiminate ligand, of which all substituents are replaced with hydrogen atoms, was modeled. Fig. 2.3.8. depicts the model compound, **2**.

2
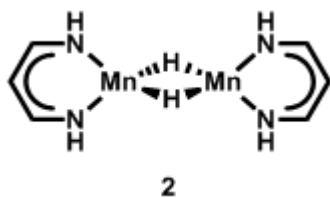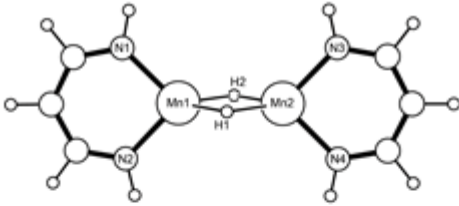
Fig. 2.3.8. The model compound **2**.

Calculations on **2** reproduced a nearly identical MO diagram to that of the full compound, **1** (Fig. S2.1). A structural comparison between the full and model compound is presented in Table 2.3.2. The Mn–Mn bond length of the model compound was calculated to be 2.816 and 2.789 Å for **2-F** and **2-AF**. The metal centers were moved apart from each other by only 0.06 Å and 0.08 Å for ferro- and antiferromagnetically coupled states, respectively. The corresponding Mayer bond orders are 0.21 and 0.24, which are comparable to the bond orders of 0.21 and 0.27 for **1-F** and **1-AF**. The steric effect, therefore, is small enough for **1-F** and **1-AF** to retain their bond orders.

Table 2.3.2 Comparison between optimized geometries of the full complex, **1**, and the model compound **2**.

	1-F	1-AF	2-F	2-AF
Spin-Coupling	F	AF	F	AF
Mn1–H1 (Å)	1.897	1.834	1.889	1.847
Mn1–H2 (Å)	1.919	1.923	1.894	1.856
Mn1–N1 (Å)	2.099	2.103	2.069	2.067
Mn1–N2 (Å)	2.116	2.110	2.069	2.067
∠H1–Mn1–N2 (°)	116.9	120.5	121.9	121.6
∠N2–Mn1–N1 (°)	90.1	90.5	91.4	91.5
∠N1–Mn1–H2 (°)	121.9	119.8	120.7	121.1
∠H2–Mn1–H1 (°)	82.2	80.5	83.7	82.3
τ₄ Mn1	0.86	0.85	0.83	0.83
Mn1–Mn2 (Å)	2.871	2.871	2.816	2.789
∠Mn1–H1–Mn2 (°)	97.5	99.6	96.2	97.7
Spin-Densities[a] Mn1	4.91	4.75	4.87	4.73
Spin-Densities[a] Mn2	4.91	−4.75	4.87	−4.73
Mayer Bond Order for Mn–Mn	0.21	0.27	0.21	0.24
Relative E$_{ΔΔ}$[b] (kcal mol⁻¹)	0.90	0	4.24	0

[a]Mulliken spin-density.
[b]The relative energies (kcal mol⁻¹) are referenced to the AF-coupled states.

The irrelevance of steric hindrance caused by the ligand to the bond order between the metal centers led us to consider the fundamental basis for the absence of a multiple bond between the Mn centers. Interaction between the metal d-orbitals and ligand-based orbitals may be an intrinsic reason for the unexpectedly low Mn–Mn bond order. The β-diketiminate ligand has a bite angle of around 90° (Table 2.3.1 and 2.3.2) and a π-conjugated system, which affords thorough mixing between the metal- and ligand-based orbitals.

As previously shown for **1**, the d$_{xz}$ orbitals are mixed with the orbitals of the nitrogen atoms of the β-diketiminate ligands (Fig. S2.5). The metal d$_{xy}$ orbitals also interact with the β-diketiminate-based orbitals (Fig. 2.3.9a and c), as well as with the hydride-based orbitals (Fig. 2.3.9b and d). Electrons supposed to occupy bonding orbitals between the metal centers are dispersed to metal–ligand interactions, resulting in the attenuation of the metal–metal bond.[86,87]

Despite adopting the broken symmetry approach, the d_{xy} and d_{z^2} orbitals contain delocalized counterparts (Fig. 2.3.9c and d, Fig. 2.3.10c and d). Considering weak δ-interactions with the d_{z^2} orbitals, we posited that the Mn–Mn bond order around 0.2 is mainly attributed to the d_{xy} orbitals. The MO diagram for the ferromagnetically coupled state, **2-F**, corroborates this postulation (Fig. S2.1). The α-orbitals consist of pairs of orbitals composed of a bonding combination and the corresponding antibonding combination, which compensate each other. The remaining bonding combinations in the β-orbitals coincide with the d_{xy} and d_{z^2} orbitals in the antiferromagnetically

coupled state, which contain residual moieties on the Mn-center on which an MO is not localized, as shown in Fig. 2.3.9c and d and Fig. 2.3.10c and d. Furthermore, hydride orbitals are incorporated in the d_{xy} and the d_{z^2} orbitals, presumably indicating the presence of a superexchange interaction mediated by bridging hydrides.
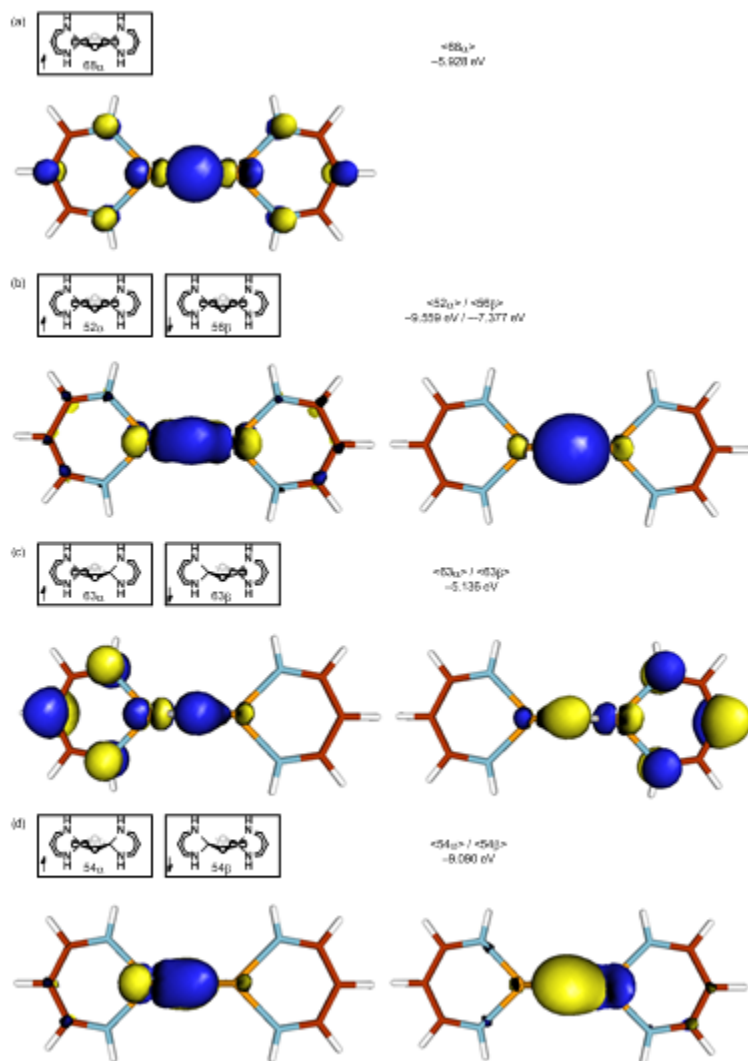
Fig. 2.3.9. Isosurface plots (isodensity = 0.05 au) of the metal d_{xy}-based MOs of **2**: a) **2-F**, <68α>, b) **2-F**, <52α> and <56β>, c) **2-AF**, <63α> and <63β>, and d) **2-AF**, <54α> and <54β>.
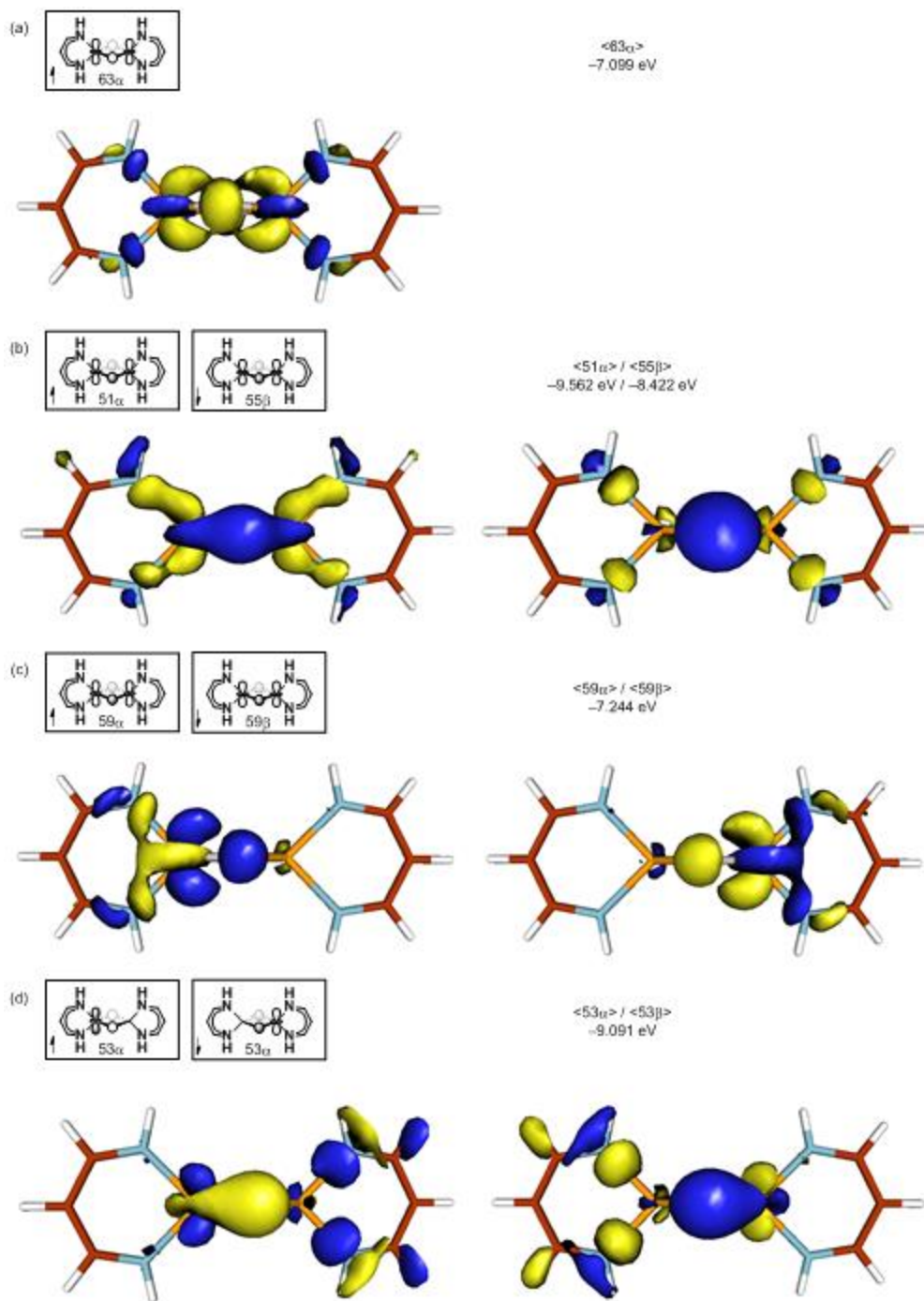
Fig. 2.3.10. Isosurface plots (isodensity = 0.05 au) of the metal d_{z^2}-based MOs of **2**: a) **2-F**, <63α>, b) **2-F**, <51α> and <55β>, c) **2-AF**, <59α> and <59β>, and d) **2-AF**, <53α> and <53β>.

2.3.4 Extension to Ligands with *p*-orbitals

Catalytic nitrile dihydroboration with **1** was recently reported by the Trovitch group.[94] The proposed mechanism involves an Mn(II) intermediate similar to **1**, in which bridging hydrides are replaced with bridging imino groups. This intermediate is far more stable than **1** by 22.51 kcal/mol. The Mn–Mn distance is also elongated from 2.814 Å to 3.082 Å. The dissimilarity was proposed to be attributed to a fundamental difference in orbitals. The bonding combination between the metal centers in **2** interacts through bridging ligands. Spherical 1*s*-orbitals in hydrides enable the in-phase combination of metal *d*-orbitals, while *p*-orbitals having a node will preclude mediation of the bonding interaction between the metal centers. The out-of-phase combination will solely be allowed with *p*-orbitals.

To evaluate this proposition, interactions between the Mn centers were further investigated by substituting bridging ligands in which *p*-orbitals are available, fluorides and hydroxides, for the bridging hydrides, of which the respective model compounds **3** and **4** are shown in Fig. 2.3.11. The structural disparity induced by the availability of *p*-orbitals is highlighted in Table 2.4.3. The most remarkable difference is the elongated Mn–Mn distance from 2.789 Å to 3.074 Å and 3.100 Å in conjunction with the decrease in the Mayer bond order from 0.24 to 0.02 and 0.03 in **3** and **4,** respectively. Similar patterns for mixing metal- and BDI ligand-based orbitals were observed, except for the incorporation of *p*-orbitals. All metal *d*-orbitals were mixed with *p*-orbitals, implying that the degree of the Mn–Mn interaction is decreased. The d_{xy} orbitals assigned as the main factor to the bonding interaction between the metal centers are depicted in Fig. 2.3.12 and Fig. 2.3.13. The p_x and p_y orbitals are mixed to interact with the d_{xy} orbitals. Bonding interactions between the metal centers via bridging ligands are symmetrically forbidden as we anticipated. As a consequence, the Mn–Mn bond strength is attenuated, resulting in the increase in Mn–Mn distance.
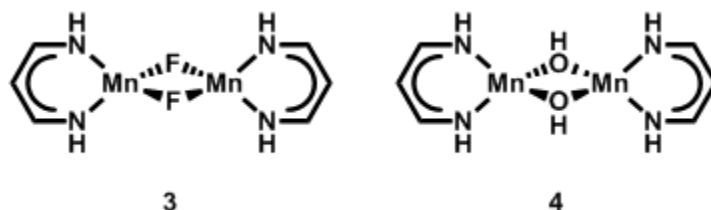
Fig. 2.3.11. The model compound with bridging fluorides, **3**, and the model compound with bridging hydroxides, **4**.
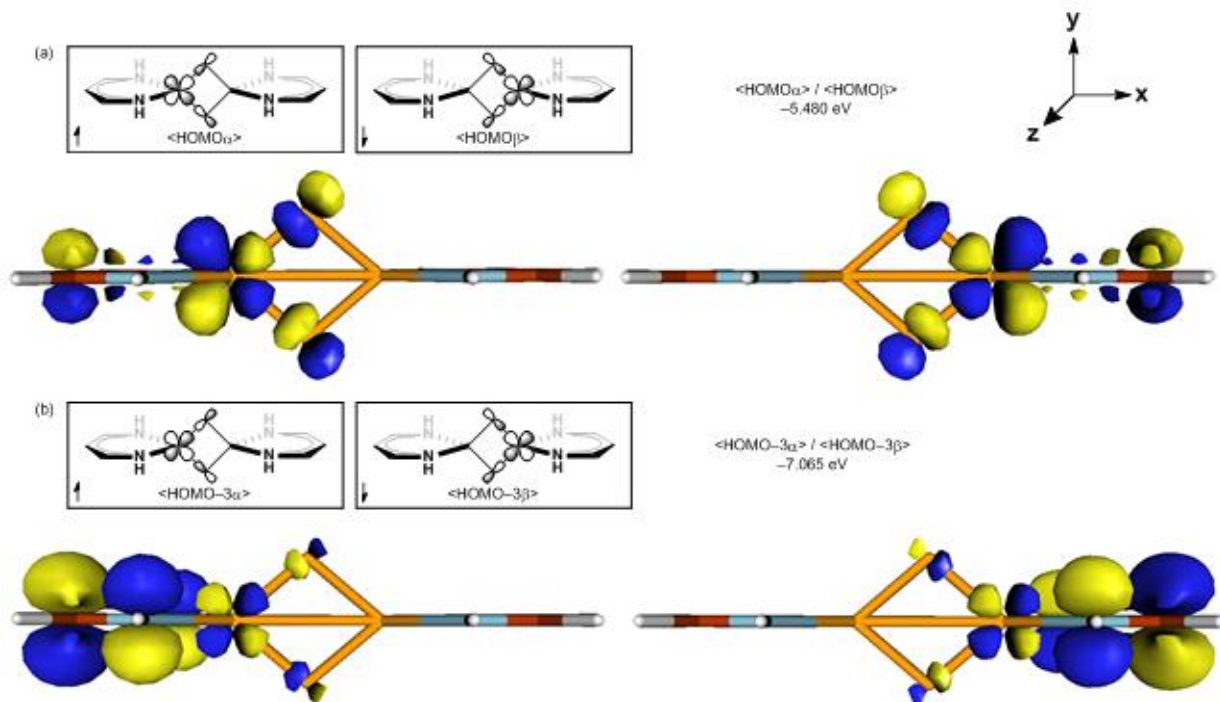
Fig. 2.3.12. Isosurface plots (isodensity = 0.05 au) of the metal d_{xy}-based MOs of **3**: (a) HOMO, (b) HOMO–3. To clearly visualize directions of orbitals, the Cartesian coordinate system consistently adopted is rotated 90 degrees in counterclockwise along the X-axis, as shown in the upper right corner.
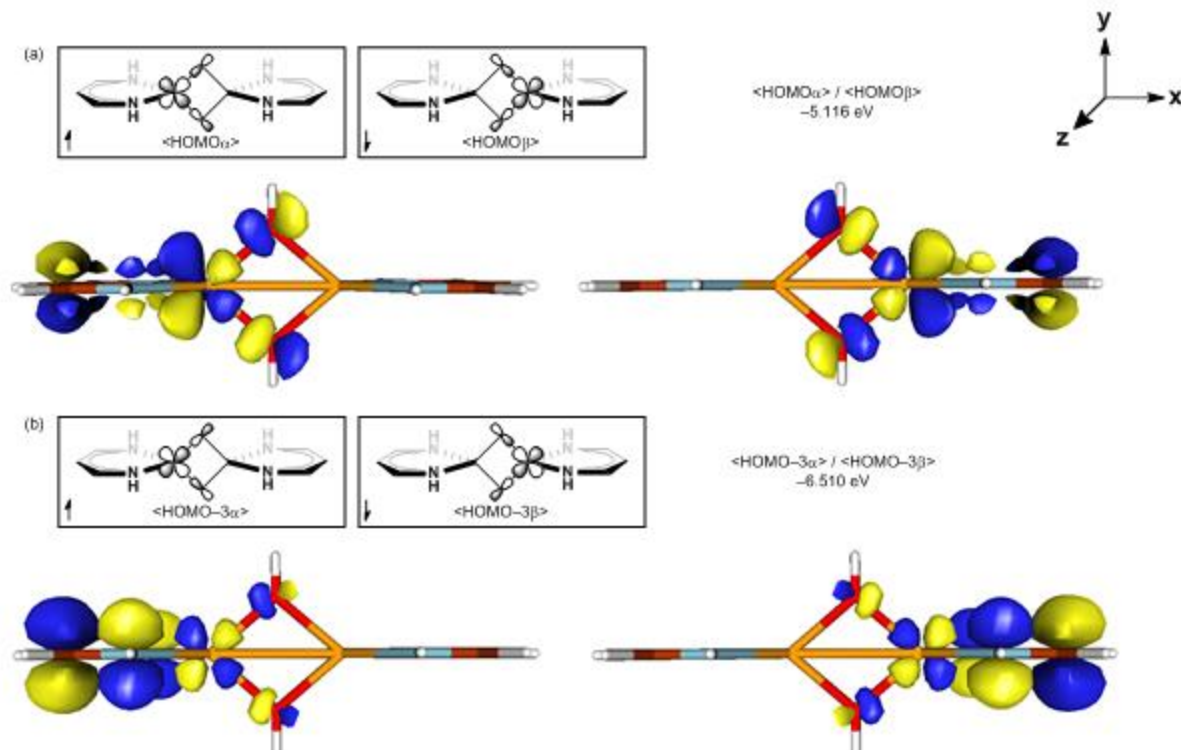
Fig. 2.3.13. Isosurface plots (isodensity = 0.05 au) of the metal d$_{xy}$-based MOs of **4**: (a) HOMO, (b) HOMO–3. To clearly visualize directions of orbitals, the Cartesian coordinate system consistently adopted is rotated 90 degrees in counterclockwise by the X-axis and shown at the upper right corner.

Table 2.3.3 Comparison of structural parameters of the optimized geometries of the model compound **2**, **3**, and **4**
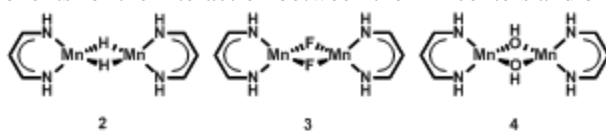
	2	3	4
Spin-Coupling	AF	AF	AF
Mn1–H1(O1, F1) (Å)	1.847	2.019	2.043
Mn1–H2(O2, F2) (Å)	1.856	2.019	2.043
Mn1–N1 (Å)	2.067	2.076	2.101
Mn1–N2 (Å)	2.067	2.077	2.102
∠H1(O1, F1)–Mn1–N2 (°)	121.6	121.8	130.0
∠N2–Mn1–N1 (°)	91.5	92.4	90.6
∠N1–Mn1–H2(O2, F2) (°)	121.1	121.7	122.6
∠H2(O2, F2)–Mn1–H1(O1, F1) (°)	82.3	80.8	81.3
τ$_4$ Mn1	0.83	0.82	0.76
Mn1–Mn2 (Å)	2.789	3.074	3.100
∠Mn1–H1(O1, F1)–Mn2 (°)	97.7	99.2	98.7
Spin-Densities[a] Mn1	4.73	4.81	4.80
Spin-Densities[a] Mn2	–4.73	–4.81	–4.80
Mayer Bond Order for Mn–Mn	0.24	0.02	0.03

[a]Mulliken spin-density.

The lengthening of the distance between the metal centers presumably accounts for the stabilization effect with *p*-orbitals. Table 2.3.4 describes the fragment analysis of the three model

compounds, **2**, **3**, and **4**. The compounds were fragmentized into three parts, one manganese subunit, the other manganese subunit and the bridging ligands. Large electron densities located on the bridging anions give rise to an immense repulsion in the core composed of the Mn centers and bridging ligands. Due to the enlarged core structure of **3**, the Pauli repulsion term is decreased by 22.5 kcal/mol compared to **2**. On the contrary, the elongated Mn–Mn bond decreases the extent of electrostatic interaction in **3**; however, the electrostatic terms do not exceed the repulsion terms, rendering **3** more stable than **2**. At first glance, the computed interaction components of **4** seem contradictory, but they can be explained. The size of hydroxides is much larger than that of hydrides or fluorides; therefore, the Pauli repulsion term of **4** is 10.0 kcal/mol higher than that of **2** due to proximity. Electrostatic interactions are understandably strengthened. Consequently, degrees of stabilization through non-orbital interactions in **3** and **4** are nearly identical. Despite the longer distances, magnitudes of orbital interactions in **3** and **4** are greater than that in **2**. The participation of *p*-orbitals probably contributes to the greater orbital interactions. The penalties in non-orbital interaction and orbital interactions of **2** gives rise to electronic destabilization. Dimerization involves a stabilization in enthalpy and disadvantage in entropy. The penalties in interaction terms of **2** can partially offset the stabilizing effect in enthalpy of the dimerization. As a result, the electronic energy of the dimer is lower by 32.5 kcal/mol than that of two equivalents of the corresponding monomer in the case of **2**, while **3** and **4** show greater energy differences of 41.9 and 50.0 kcal/mol, respectively. Taking into account entropy penalties, the monomer-dimer Gibbs energy differences in **2**, **3**, and **4** at room temperature diminish to 18.6, 28.3 and 35.8 kcal/mol, respectively. Furthermore, in benzene solution, the energy difference at room temperature of **2** becomes 4.1 kcal/mol, while that of **3** and **4** stays at 16.5 and 24.6 kcal/mol, which is far more difficult to attain. In accordance with the model study, **1-AF**, the fluoride congener of **1**, [($_{2,6-iPr2Ph}$BDI)Mn(μ-F)]$_2$ (**5**), and the hydroxide congener of **1**, [($_{2,6-iPr2Ph}$BDI)Mn(μ-OH)]$_2$ (**6**) are lower in energy than their corresponding monomers by 7.1, 22.6 and 28.8 kcal/mol, respectively.

Table 2.3.4. Computed components for the interaction between the Mn centers and bridging ligands in **2**, **3** and **4.**

(in kcal/mol)	2	3	4	Δ_1 (3 − 2)	Δ_2 (4 − 2)
Mn–Mn (Å)	2.789	3.074	3.100	–	–
Pauli repulsion (PR)	278.93	256.47	288.91	−22.46	9.98
Electrostatic interaction (EI)	−618.85	−608.69	−639.48	10.16	−20.63
Non-orbital interaction (PR + EI)	−339.92	−352.22	−350.58	−12.30	−10.65
Orbital interaction	−395.21	−400.01	−431.05	−4.80	−35.84

Synthesis of the Hydroxide-Bridged Dimer.[1] To support the calculations conducted on model compound **4** and full hydroxide complex **6**, attempts to synthesize the latter were made by Trovitch and coworkers. Upon dissolving **1** in THF solution, the slow addition of a second THF solution containing two equivalents of H_2O resulted in the liberation of H_2 gas and a light yellow product identified as **6**. The magnetic susceptibility of **6** was analyzed by the Gouy method and determined to be 7.4 μ_B at 291 K. Notably, the infrared spectrum of this complex was found to exhibit a hydroxide OH stretch at 3,695 cm^{-1} that shifted to 2,726 cm^{-1} when D_2O was employed in the synthesis (**6-**d_2).

To confirm the identity of **6** and obtain an experimental Mn–Mn bond distance, single crystals were grown from THF at 238 K and X-ray diffraction data was collected. The crystal structure of **6** (Fig. 2.3.14) features an inversion center, eclipsed BDI ligands, and a relatively long Mn1–Mn1A distance of 3.1426(9) Å. This distance is consistent with the calculated distance of 3.189 Å and a full comparison of the experimental and computational bond distances is provided in Table 2.3.5.
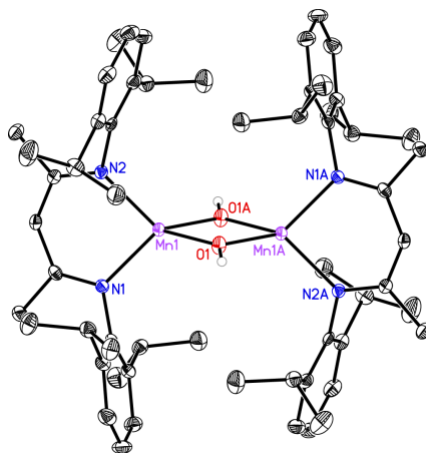
Fig. 2.3.14. Solid state structure of **6** at 30% probability ellipsoids. From Professor Trovitch and coworkers.

[1] The synthesis and characterization of this compound were carried out by Professor Trovitch and coworkers.

Table 2.3.5. Experimental and calculated metrical parameters of **6**
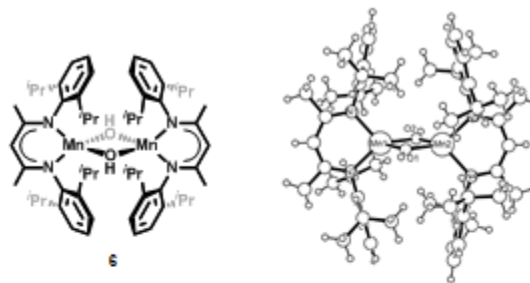
	6 exp.	6 calc.
Spin-Coupling	–	AF
Mn1–O1 (Å)	2.037	2.056
Mn1–O2 (Å)	2.054	2.071
Mn1–N1 (Å)	2.106	2.107
Mn1–N2 (Å)	2.108	2.119
∠O1–Mn1–N2 (°)	127.0	125.0
∠N2–Mn1–N1 (°)	91.3	89.2
∠N1–Mn1–O2 (°)	120.5	124.5
∠O2–Mn1–O1 (°)	79.6	78.9
τ_4 Mn1	0.80	0.78
Mn1–Mn2 (Å)	3.142	3.189
∠Mn1–O1–Mn2 (°)	100.4	101.2
Spin-Densities[a] Mn1	–	4.80
Spin-Densities[a] Mn2	–	–4.80

[a] Mulliken spin-density.

2.4 Conclusion

DFT calculations were performed on the ferromagnetically and antiferromagnetically coupled manganese dimer, $[(_{2,6\text{-iPr2Ph}}BDI)Mn(\mu\text{-H})]_2$, in order to elucidate interactions between the metal centers. Whereas the electron count suggests a formal bond order of 3, the calculated bond order is much lower at 0.21 and 0.27, for **1-F** and **1-AF** respectively. The total energies of **1-F** and **1-AF** show that the antiferromagnetically coupled complex is the ground state, for which a coupling value $J_o = -10.9$ cm$_{-1}$ was calculated. This is in accordance with experimental data, which afforded $J_o = -15 \pm 0.1$ cm$_{-1}$ or $J_o = -20 \pm 0.1$ cm$_{-1}$ by SQUID and $J_o = -10.2 \pm 0.7$ cm$_{-1}$ by EPR spectroscopy. The influence of steric bulk on the decreased bond order was ruled out by calculations on model compounds **2-F** and **2-AF**, which show near identical bond orders to **1-F** and **1-AF**. Analysis of the molecular orbitals reveals that extensive mixing of the metal d_{xy}- and d_{xz}-orbitals with the ligand-based orbitals prevents direct orbital overlap of the metal centers, reducing the bond order. The d_{xy} orbitals are likely the major contributor to bonding interaction due to the presence of residual moiety in the broken-symmetry orbitals. A stable analogue of **1** comprising an increased Mn–Mn distance reported by the Trovitch group led us to further investigate the effect of bridging p-orbitals. The p-orbitals

symmetrically prohibit the in-phase combination of metal d-orbitals as well as interact with all metal d-orbitals, resulting in the lengthening of the Mn–Mn bond. Fragment analysis revealed that both non-orbital interactions and orbital interactions stabilize dimeric compounds with bridging ligands with p-orbitals. To corroborate our calculations, the congener of **1** with bridging hydroxides was synthesized and characterized.

Acknowledgements

Firstly, I would like to thank Professor Mu-Hyun Baik for taking me on and giving me a chance, even though I had no prior experience with computational modeling. I have learnt much throughout my time here and I could not have done that without your guidance. Secondly, I want to thank Hong Ki Kim and Jun-Hyeong Kim for teaching me molecular modeling and always being prepared to answer even my most stupid questions. I would also like to thank Professor Marc-Etienne Moret for agreeing to let me come all the way to South Korea for my research project and helping me iron out all the technical details and difficulties related to a plan like this. I want to thank all the members of the Baik group, but in particular Eunji Lee, Hanna Lee, Yerin Park and Suyeon Kim, for welcoming me into the group and to Korea. Without your friendship and help, my time and experiences here in Korea would not be remembered as fondly as they will be now. Lastly, the Institute for Basic Science(IBS-R010-D1) is acknowledged for supporting this research.

References

(1)   Mukhopadhyay, T. K.; Flores, M.; Groy, T. L.; Trovitch, R. J. A β-Diketiminate Manganese Catalyst for Alkene Hydrosilylation: Substrate Scope, Silicone Preparation, and Mechanistic Insight. *Chem. Sci.* **2018**, *9* (39), 7673–7680.

(2)   Koch, W.; Holthausen, M. C. A Chemist's Guide to Density Functional Theory. 2001. https://doi.org/10.1002/3527600043.

(3)   Tullo, A. H. Celanese Takes an Ethanol Plunge. *Chem. Eng. News* **2011**, *89* (43), 20–21.

(4)   Tullo, A. H. Refining Chemicals | April 23, 2007 Issue - Vol. 85 Issue 17 | Chemical & Engineering News https://cen.acs.org/articles/85/i17/Refining-Chemicals.html (accessed Jan 7, 2020).

(5)   Sadrameli, S. M. Thermal/catalytic Cracking of Hydrocarbons for the Production of Olefins: A State-of-the-Art Review I: Thermal Cracking Review. *Fuel* **2015**, *140*, 102–115.

(6)   Ren, T.; Patel, M.; Blok, K. Olefins from Conventional and Heavy Feedstocks: Energy Use in Steam Cracking and Alternative Processes. *Energy* **2006**, *31* (4), 425–451.

(7)   Kumar, A.; Bhatti, T. M.; Goldman, A. S. Dehydrogenation of Alkanes and Aliphatic Groups by Pincer-Ligated Metal Complexes. *Chem. Rev.* **2017**, *117* (19), 12357–12384.

(8)   Kumar, A.; Goldman, A. S. Recent Advances in Alkane Dehydrogenation Catalyzed by Pincer Complexes. In *The Privileged Pincer-Metal Platform: Coordination Chemistry & Applications*; van Koten, G., Gossage, R. A., Eds.; Springer International Publishing: Cham, 2016; pp 307–334.

(9)   Dobereiner, G. E.; Crabtree, R. H. Dehydrogenation as a Substrate-Activating Strategy in Homogeneous Transition-Metal Catalysis. *Chem. Rev.* **2010**, *110* (2), 681–703.

(10)   Maguire, J. A.; Boese, W. T.; Goldman, A. S. Photochemical Dehydrogenation of Alkanes Catalyzed by Trans-Carbonylchlorobis(trimethylphosphine)rhodium: Aspects of Selectivity and Mechanism. *Journal of the American Chemical Society*. 1989, pp 7088–7093. https://doi.org/10.1021/ja00200a030.

(11)   Six, C.; Gabor, B.; Görls, H.; Mynott, R.; Philipps, P.; Leitner, W. Inter- and Intramolecular Thermal Activation of sp3 C−H Bonds with Ruthenium Bisallyl Complexes. *Organometallics* **1999**, *18* (17), 3316–3326.

(12)   Gupta, M.; Hagen, C.; Kaska, W. C.; Cramer, R. E.; Jensen, C. M. Catalytic Dehydrogenation of Cycloalkanes to Arenes by a Dihydrido Iridium P−C−P Pincer Complex. *Journal of the American Chemical Society*. 1997, pp 840–841. https://doi.org/10.1021/ja962560x.

(13)   Solowey, D. P.; Mane, M. V.; Kurogi, T.; Carroll, P. J.; Manor, B. C.; Baik, M.-H.; Mindiola, D. J. A New and Selective Cycle for Dehydrogenation of Linear and Cyclic Alkanes under Mild Conditions Using a Base Metal. *Nat. Chem.* **2017**, *9* (11), 1126–1132.

(14)   Weckhuysen, B. M.; Schoonheydt, R. A. Alkane Dehydrogenation over Supported Chromium Oxide Catalysts. *Catal. Today* **1999**, *51* (2), 223–232.

(15)   Tang, P.; Zhu, Q.; Wu, Z.; Ma, D. Methane Activation: The Past and Future. *Energy Environ. Sci.* **2014**, *7* (8), 2580–2591.

(16)   Heracleous, E.; Lemonidou, A. A. Reaction Pathways of Ethane Oxidative and Non-Oxidative Dehydrogenation on γ-Al2O3 Studied by Temperature-Programmed Reaction (TP-Reaction). *Catal. Today* **2006**, *112* (1), 23–27.

(17)   Copéret, C. C-H Bond Activation and Organometallic Intermediates on Isolated Metal Centers on Oxide Surfaces. *Chem. Rev.* **2010**, *110* (2), 656–680.

(18)   LINSTORM; P. Nist Chemistry Webbook, Nist Standard Reference Database Number 69. *J. Phys. Chem. Ref. Data, Monograph* **1998**, *9*, 1–1951.

(19)   Stull, D. R.; Westrum, E. F.; Sinke, G. C. The Chemical Thermodynamics of Organic Compounds. **1969**.

(20)   Chhowalla, M.; Shin, H. S.; Eda, G.; Li, L.-J.; Loh, K. P.; Zhang, H. The Chemistry of Two-

Dimensional Layered Transition Metal Dichalcogenide Nanosheets. *Nat. Chem.* **2013**, *5* (4), 263–275.

(21)   Nguyen, T. P.; Choi, S.; Jeon, J.-M.; Kwon, K. C.; Jang, H. W.; Kim, S. Y. Transition Metal Disulfide Nanosheets Synthesized by Facile Sonication Method for the Hydrogen Evolution Reaction. *J. Phys. Chem. C* **2016**, *120* (7), 3929–3935.

(22)   Jariwala, D.; Sangwan, V. K.; Lauhon, L. J.; Marks, T. J.; Hersam, M. C. Emerging Device Applications for Semiconducting Two-Dimensional Transition Metal Dichalcogenides. *ACS Nano* **2014**, *8* (2), 1102–1120.

(23)   Zhu, Q.; Wegener, S. L.; Xie, C.; Uche, O.; Neurock, M.; Marks, T. J. Sulfur as a Selective "Soft" Oxidant for Catalytic Methane Conversion Probed by Experiment and Theory. *Nat. Chem.* **2013**, *5* (2), 104–109.

(24)   Jaramillo, T. F.; Jørgensen, K. P.; Bonde, J.; Nielsen, J. H.; Horch, S.; Chorkendorff, I. Identification of Active Edge Sites for Electrochemical H2 Evolution from MoS2 Nanocatalysts. *Science* **2007**, *317* (5834), 100–102.

(25)   Li, Y.; Wang, H.; Xie, L.; Liang, Y.; Hong, G.; Dai, H. MoS2 Nanoparticles Grown on Graphene: An Advanced Catalyst for the Hydrogen Evolution Reaction. *J. Am. Chem. Soc.* **2011**, *133* (19), 7296–7299.

(26)   Li, H.; Tsai, C.; Koh, A. L.; Cai, L.; Contryman, A. W.; Fragapane, A. H.; Zhao, J.; Han, H. S.; Manoharan, H. C.; Abild-Pedersen, F.; et al. Activating and Optimizing MoS2 Basal Planes for Hydrogen Evolution through the Formation of Strained Sulphur Vacancies. *Nat. Mater.* **2016**, *15* (1), 48–53.

(27)   Han, J. H.; Kim, H. K.; Baek, B.; Han, J.; Ahn, H. S.; Baik, M.-H.; Cheon, J. Activation of the Basal Plane in Two Dimensional Transition Metal Chalcogenide Nanostructures. *J. Am. Chem. Soc.* **2018**, *140* (42), 13663–13671.

(28)   Wang, G.; Li, C.; Shan, H. Highly Efficient Metal Sulfide Catalysts for Selective Dehydrogenation of Isobutane to Isobutene. *ACS Catal.* **2014**, *4* (4), 1139–1143.

(29)   Lv, R.; Robinson, J. A.; Schaak, R. E.; Sun, D.; Sun, Y.; Mallouk, T. E.; Terrones, M. Transition Metal Dichalcogenides and beyond: Synthesis, Properties, and Applications of Single- and Few-Layer Nanosheets. *Acc. Chem. Res.* **2015**, *48* (1), 56–64.

(30)   Chhowalla, M.; Liu, Z.; Zhang, H. Two-Dimensional Transition Metal Dichalcogenide (TMD) Nanosheets. *Chem. Soc. Rev.* **2015**, *44* (9), 2584–2586.

(31)   Han, J. H.; Kwak, M.; Kim, Y.; Cheon, J. Recent Advances in the Solution-Based Preparation of Two-Dimensional Layered Transition Metal Chalcogenide Nanostructures. *Chem. Rev.* **2018**, *118* (13), 6151–6188.

(32)   Bosi, M. Growth and Synthesis of Mono and Few-Layers Transition Metal Dichalcogenides by Vapour Techniques: A Review. *RSC Adv.* **2015**.

(33)   Yuan, H.; Kong, L.; Li, T.; Zhang, Q. A Review of Transition Metal Chalcogenide/graphene Nanocomposites for Energy Storage and Conversion. *Chin. Chem. Lett.* **2017**, *28* (12), 2180–2194.

(34)   Wang, Y.-H.; Huang, K.-J.; Wu, X. Recent Advances in Transition-Metal Dichalcogenides Based Electrochemical Biosensors: A Review. *Biosens. Bioelectron.* **2017**, *97*, 305–316.

(35)   Xiao, Y.; Zhou, M.; Liu, J.; Xu, J.; Fu, L. Phase Engineering of Two-Dimensional Transition Metal Dichalcogenides. *Science China Materials* **2019**, *62* (6), 759–775.

(36)   Li, S. N.; Liu, J. B.; Liu, B. X. First Principles Study of Nanostructured TiS2 Electrodes for Na and Mg Ion Storage. *J. Power Sources* **2016**, *320*, 322–331.

(37)   Crabtree, R. H. Organometallic Alkane CH Activation. *J. Organomet. Chem.* **2004**, *689* (24), 4083–4091.

(38)   Pierre, J.-L.; Thomas, F. Homolytic C–H Bond Cleavage (H-Atom Transfer): Chemistry for a Paramount Biological Process. *C. R. Chim.* **2005**, *8* (1), 65–74.

(39)   Groves, J. T.; McClusky, G. A. Aliphatic Hydroxylation via Oxygen Rebound. Oxygen Transfer

Catalyzed by Iron. *J. Am. Chem. Soc.* **1976**, *98* (3), 859–861.

(40)   Groves, J. T. Key Elements of the Chemistry of Cytochrome P-450: The Oxygen Rebound Mechanism. *J. Chem. Educ.* **1985**, *62* (11), 928.

(41)   Ogliaro, F.; Harris, N.; Cohen, S.; Filatov, M.; de Visser, S. P.; Shaik, S. A Model "Rebound" Mechanism of Hydroxylation by Cytochrome P450: Stepwise and Effectively Concerted Pathways, and Their Reactivity Patterns. *J. Am. Chem. Soc.* **2000**, *122* (37), 8977–8989.

(42)   Schöneboom, J. C.; Cohen, S.; Lin, H.; Shaik, S.; Thiel, W. Quantum Mechanical/Molecular Mechanical Investigation of the Mechanism of C–H Hydroxylation of Camphor by Cytochrome P450cam: Theory Supports a Two-State Rebound Mechanism. *Journal of the American Chemical Society*. 2004, pp 4017–4034. https://doi.org/10.1021/ja039847w.

(43)   Tenn, W. J.; Young, K. J. H.; Oxgaard, J.; Nielsen, R. J.; Goddard, W. A.; Periana, R. A. Heterolytic CH Activation and Catalysis by an O-Donor Iridium–Hydroxo Complex. *Organometallics*. 2006, pp 5173–5175. https://doi.org/10.1021/om060657e.

(44)   Young, K. J. H.; Meier, S. K.; Gonzales, J. M.; Oxgaard, J.; Goddard, W. A.; Periana, R. A. Heterolytic CH Activation with a Cyclometalated Platinum(II) 6-Phenyl-4,4'-Di-Tert-Butyl-2,2-Bipyridine Complex. *Organometallics* **2006**, *25* (20), 4734–4737.

(45)   Rocchigiani, L.; Budzelaar, P. H. M.; Bochmann, M. Heterolytic Bond Activation at Gold: Evidence for Gold(iii) H-B, H-Si Complexes, H-H and H-C Cleavage. *Chem. Sci.* **2019**, *10* (9), 2633–2642.

(46)   Kurogi, T.; Won, J.; Park, B.; Trofymchuk, O. S.; Carroll, P. J.; Baik, M.-H.; Mindiola, D. J. Room Temperature Olefination of Methane with Titanium-Carbon Multiple Bonds. *Chem. Sci.* **2018**, *9* (13), 3376–3385.

(47)   Grimme, S.; Bannwarth, C.; Shushkov, P. A Robust and Accurate Tight-Binding Quantum Chemical Method for Structures, Vibrational Frequencies, and Noncovalent Interactions of Large Molecular Systems Parametrized for All Spd-Block Elements (Z = 1–86). *Journal of Chemical Theory and Computation*. 2017, pp 1989–2009. https://doi.org/10.1021/acs.jctc.7b00118.

(48)   Bannwarth, C.; Ehlert, S.; Grimme, S. GFN2-xTB - an Accurate and Broadly Parametrized Self-Consistent Tight-Binding Quantum Chemical Method with Multipole Electrostatics and Density-Dependent Dispersion Contributions. https://doi.org/10.26434/chemrxiv.7246238.v1.

(49)   Saeys, M.; -F. Reyniers, M.; Neurock, M.; Marin, G. B. Ab Initio Reaction Path Analysis of Benzene Hydrogenation to Cyclohexane on Pt(111)†. *The Journal of Physical Chemistry B*. 2005, pp 2064–2073. https://doi.org/10.1021/jp049421j.

(50)   Koel, B. E.; Blank, D. A.; Carter, E. A. Thermochemistry of the Selective Dehydrogenation of Cyclohexane to Benzene on Pt Surfaces. *J. Mol. Catal. A Chem.* **1998**, *131* (1), 39–53.

(51)   Nagahara, H.; Ono, M.; Konishi, M.; Fukuoka, Y. Partial Hydrogenation of Benzene to Cyclohexene. *Applied Surface Science*. 1997, pp 448–451. https://doi.org/10.1016/s0169-4332(97)00325-5.

(52)   Tomasi, J.; Menucci, B.; Cammi, R. Quantum Mechanical Continuum Solvation Models. *ChemInform*. 2005. https://doi.org/10.1002/chin.200542292.

(53)   Ryu, H.; Park, J.; Kim, H. K.; Park, J. Y.; Kim, S.-T.; Baik, M.-H. Pitfalls in Computational Modeling of Chemical Reactions and How To Avoid Them. *Organometallics* **2018**, *37* (19), 3228–3239.

(54)   Power, P. P. Stable Two-Coordinate, Open-Shell (d1-d9) Transition Metal Complexes. *Chem. Rev.* **2012**, *112* (6), 3482–3507.

(55)   Power, P. P. Some Highlights from the Development and Use of Bulky Monodentate Ligands. *J. Organomet. Chem.* **2004**, *689* (24), 3904–3919.

(56)   Holland, P. L. Electronic Structure and Reactivity of Three-Coordinate Iron Complexes. *Acc. Chem. Res.* **2008**, *41* (8), 905–914.

(57)   Chen, C.; Bellows, S. M.; Holland, P. L. Tuning Steric and Electronic Effects in Transition-Metal β-Diketiminate Complexes. *Dalton Trans.* **2015**, *44* (38), 16654–16670.

(58)   Webster, R. L. β-Diketimine Complexes of the First Row Transition Metals: Applications in Catalysis. *Dalton Trans.* **2017**, *46* (14), 4483–4498.

(59)   Basuli, F.; Aneetha, H.; Huffman, J. C.; Mindiola, D. J. A Fluorobenzene Adduct of Ti(IV), and Catalytic Carboamination to Prepare Alpha,beta-Unsaturated Imines and Triaryl-Substituted Quinolines. *J. Am. Chem. Soc.* **2005**, *127* (51), 17992–17993.

(60)   Vela, J.; Smith, J. M.; Yu, Y.; Ketterer, N. A.; Flaschenriem, C. J.; Lachicotte, R. J.; Holland, P. L. Synthesis and Reactivity of Low-Coordinate iron(II) Fluoride Complexes and Their Use in the Catalytic Hydrodefluorination of Fluorocarbons. *J. Am. Chem. Soc.* **2005**, *127* (21), 7857–7870.

(61)   Chai, J.; Zhu, H.; Fan, H.; Roesky, H. W.; Magull, J. Structurally Characterized Neutral Monoalkyl and -Aryl Complexes of Manganese(II). *Organometallics* **2004**, *23* (6), 1177–1179.

(62)   Chai, J.; Zhu, H.; Stückl, A. C.; Roesky, H. W.; Magull, J.; Bencini, A.; Caneschi, A.; Gatteschi, D. Synthesis and Reaction of [[HC(CMeNAr)2]Mn]2 (Ar = 2,6-iPr2C6H3): The Complex Containing Three-Coordinate manganese(I) with a Mn-Mn Bond Exhibiting Unusual Magnetic Properties and Electronic Structure. *J. Am. Chem. Soc.* **2005**, *127* (25), 9201–9206.

(63)   Yao, S.; Xiong, Y.; Driess, M. Facile Metalation of Silicon and Germanium Analogues of Thiocarboxylic Acids with a manganese(II) Hydride Precursor. *Chemistry* **2012**, *18* (36), 11356–11361.

(64)   Bochevarov, A. D.; Harder, E.; Hughes, T. F.; Greenwood, J. R.; Braden, D. A.; Philipp, D. M.; Rinaldo, D.; Halls, M. D.; Zhang, J.; Friesner, R. A. Jaguar: A High-Performance Quantum Chemistry Software Program with Strengths in Life and Materials Sciences. *Int. J. Quantum Chem.* **2013**, *113* (18), 2110–2142.

(65)   Becke, A. D. Density-Functional Exchange-Energy Approximation with Correct Asymptotic Behavior. *Phys. Rev. A Gen. Phys.* **1988**, *38* (6), 3098–3100.

(66)   Lee, C.; Yang, W.; Parr, R. G. Development of the Colle-Salvetti Correlation-Energy Formula into a Functional of the Electron Density. *Phys. Rev. B Condens. Matter* **1988**, *37* (2), 785–789.

(67)   Grimme, S.; Antony, J.; Ehrlich, S.; Krieg, H. A Consistent and Accurate Ab Initio Parametrization of Density Functional Dispersion Correction (DFT-D) for the 94 Elements H-Pu. *J. Chem. Phys.* **2010**, *132* (15), 154104.

(68)   Hay, P. J.; Wadt, W. R. Ab Initio Effective Core Potentials for Molecular Calculations. Potentials for the Transition Metal Atoms Sc to Hg. *J. Chem. Phys.* **1985**, *82* (1), 270–283.

(69)   Wadt, W. R.; Hay, P. J. Ab Initio Effective Core Potentials for Molecular Calculations. Potentials for Main Group Elements Na to Bi. *J. Chem. Phys.* **1985**, *82* (1), 284–298.

(70)   Hay, P. J.; Wadt, W. R. Ab Initio Effective Core Potentials for Molecular Calculations. Potentials for K to Au Including the Outermost Core Orbitals. *J. Chem. Phys.* **1985**, *82* (1), 299–310.

(71)   Dunning, T. H. Gaussian Basis Sets for Use in Correlated Molecular Calculations. I. The Atoms Boron through Neon and Hydrogen. *J. Chem. Phys.* **1989**, *90* (2), 1007–1023.

(72)   te Velde, G.; Bickelhaupt, F. M.; Baerends, E. J.; Fonseca Guerra, C.; van Gisbergen, S. J. A.; Snijders, J. G.; Ziegler, T. Chemistry with ADF. *J. Comput. Chem.* **2001**, *22* (9), 931–967.

(73)   Rashin, A. A.; Honig, B. Reevaluation of the Born Model of Ion Hydration. *J. Phys. Chem.* **1985**, *89* (26), 5588–5593.

(74)   Noodleman, L. Valence Bond Description of Antiferromagnetic Coupling in Transition Metal Dimers. *J. Chem. Phys.* **1981**, *74* (10), 5737–5743.

(75)   Dunietz, B. D.; Beachy, M. D.; Cao, Y.; Whittington, D. A.; Lippard, S. J.; Friesner, R. A. Large Scale Ab Initio Quantum Chemical Calculation of the Intermediates in the Soluble Methane Monooxygenase Catalytic Cycle. *J. Am. Chem. Soc.* **2000**, *122* (12), 2828–2839.

(76)   Nguyen, T.; Sutton, A. D.; Brynda, M.; Fettinger, J. C.; Long, G. J.; Power, P. P. Synthesis of a Stable Compound with Fivefold Bonding between Two chromium(I) Centers. *Science* **2005**, *310*

(5749), 844–847.

(77)   Fohlmeister, L.; Liu, S.; Schulten, C.; Moubaraki, B.; Stasch, A.; Cashion, J. D.; Murray, K. S.; Gagliardi, L.; Jones, C. Low-Coordinate Iron(I) and Manganese(I) Dimers: Kinetic Stabilization of an Exceptionally Short Fe▯Fe Multiple Bond. *Angew. Chem. Int. Ed.* **2012**, *51* (33), 8294–8298.

(78)   Bernal, I.; Korp, J. D.; Herrmann, W. A.; Serrano, R. Syntheses of Metal Carbonyls, XVI1). Metal-Metal Multiple Bonds: Synthesis, Crystal and Molecular Structure of Tri-μ-Carbonyl-bis[(η5-pentamethylcyclopentadienyl)manganese](Mn ≡ Mn) – The First Manganese-Manganese Triple Bond. *Chem. Ber.* **1984**, *117* (2), 434–444.

(79)   Ashley, A. E.; Cooper, R. T.; Wildgoose, G. G.; Green, J. C.; O'Hare, D. Homoleptic Permethylpentalene Complexes: "Double Metallocenes" of the First-Row Transition Metals. *J. Am. Chem. Soc.* **2008**, *130* (46), 15662–15677.

(80)   Nolting, W.; Ramakanth, A. *Quantum Theory of Magnetism*; Springer, Berlin, Heidelberg, 2009.

(81)   Dzyaloshinsky, I. A Thermodynamic Theory of "weak" Ferromagnetism of Antiferromagnetics. *J. Phys. Chem. Solids* **1958**, *4* (4), 241–255.

(82)   Hicks, J.; Hoyer, C. E.; Moubaraki, B.; Li Manni, G.; Carter, E.; Murphy, D. M.; Murray, K. S.; Gagliardi, L.; Jones, C. A Two-Coordinate manganese(0) Complex with an Unsupported Mn-Mg Bond: Allowing Access to Low Coordinate Homo- and Heterobimetallic Compounds. *J. Am. Chem. Soc.* **2014**, *136* (14), 5283–5286.

(83)   Fink, K.; Wang, C.; Staemmler, V. Superexchange and Spin- Orbit Coupling in Chlorine-Bridged Binuclear Cobalt (II) Complexes. *Inorg. Chem.* **1999**, *38* (17), 3847–3856.

(84)   Azuah, R. T.; Kneller, L. R.; Qiu, Y.; Tregenna-Piggott, P. L. W.; Brown, C. M.; Copley, J. R. D.; Dimeo, R. M. DAVE: A Comprehensive Software Suite for the Reduction, Visualization, and Analysis of Low Energy Neutron Spectroscopic Data. *J. Res. Natl. Inst. Stand. Technol.* **2009**, *114* (6), 341–358.

(85)   Chilton, N. F.; Anderson, R. P.; Turner, L. D.; Soncini, A.; Murray, K. S. PHI: A Powerful New Program for the Analysis of Anisotropic Monomeric and Exchange-Coupled Polynuclear D- and F-Block Complexes. *J. Comput. Chem.* **2013**, *34* (13), 1164–1175.

(86)   Cordero, B.; Gómez, V.; Platero-Prats, A. E.; Revés, M.; Echeverría, J.; Cremades, E.; Barragán, F.; Alvarez, S. Covalent Radii Revisited. *Dalton Trans.* **2008**, No. 21, 2832–2838.

(87)   Nayak, S. K.; Rao, B. K.; Jena, P. Equilibrium Geometries, Electronic Structure and Magnetic Properties of Small Manganese Clusters. *J. Phys. Condens. Matter* **1999**, *10* (48), 10863.

(88)   Hansen, S.; Müller-Warmuth, W. J. R. Pilbrow: Transition Ion Electron Paramagnetic Resonance, Clarendon Press, Oxford 1990. ISBN 0-19-855214-9. 717 Seiten, Preis: £85.-. *Berichte der Bunsengesellschaft für physikalische Chemie*. 1991, pp 1307–1307. https://doi.org/10.1002/bbpc.19910951036.

(89)   Dowsing, R. D.; Gibson, J. F.; Goodgame, M.; Hayward, P. J. Electron Spin Resonance Studies of Some manganese(II) Complexes with Heterocyclic Ligands. *J. Chem. Soc. A* **1969**, No. 0, 187–193.

(90)   Dowsing, R. D.; Gibson, J. F.; Goodgame, M.; Hayward, P. J. Electron Spin Resonance Studies of Some Complexes of manganese(II) with Chelating Ligands. *J. Chem. Soc. A* **1970**, No. 0, 1133–1138.

(91)   Bencini, A.; Gatteschi, D. Electron Paramagnetic Resonance of Exchange Coupled Systems. 1990. https://doi.org/10.1007/978-3-642-74599-7.

(92)   Stoll, S.; Schweiger, A. EasySpin, a Comprehensive Software Package for Spectral Simulation and Analysis in EPR. *J. Magn. Reson.* **2006**, *178* (1), 42–55.

(93)   AMS DFTB 2019.3, SCM, Theoretical Chemistry, Vrije Universiteit, Amsterdam, The Netherlands, http://www.scm.com

(94)   Nguyen, T. T., Kim, J. H., Kim, S., Oh, C., Flores, M., Groy, T. L., Baik, M.-H., Trovitch, R. J. Scope and mechanism of nitrile dihydroboration mediated by a β-diketiminate manganese hydride catalyst. *Chem. Comm.* **2020**, *in press*.

Appendix
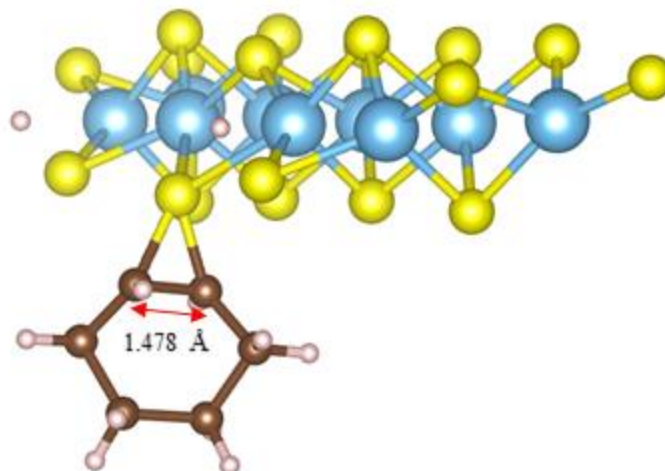
Figure S1.1. Thiirane intermediate of cyclohexane. The C–C bond of the carbon atoms participating in the thiirane cycle is shortened slightly from 1.498 Å to 1.478 Å, but is longer than the typical C = C bond at 1.340 Å. The total energy of the complex ΔE_{Tot} = 41.16 kcal/mol.
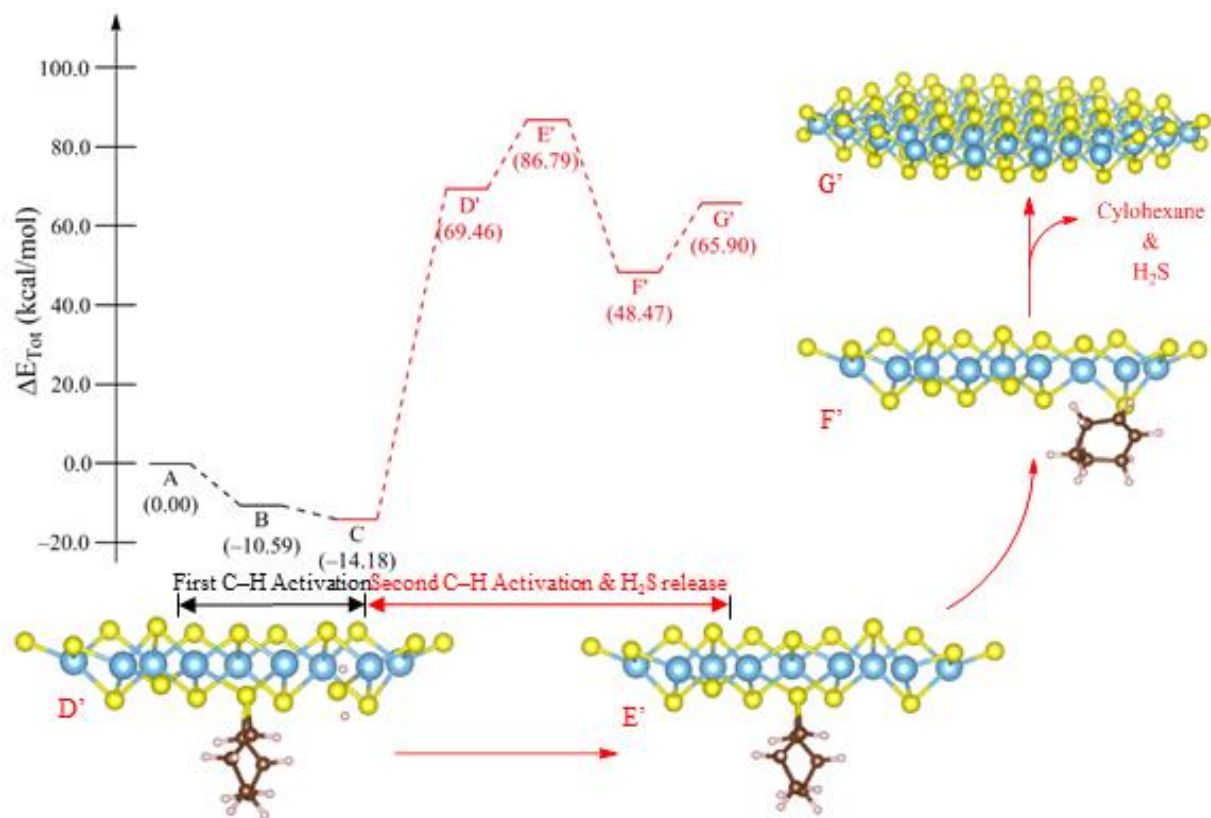
Figure S1.2. The reaction energy profile of cyclohexane dehydrogenation including H₂S production. The part of the profile given in red is the part that differs from the reaction energy profile given in Fig. 1.3.1. Only the geometries of the differing reaction steps are shown. ΔE_{Tot} given in kcal/mol.
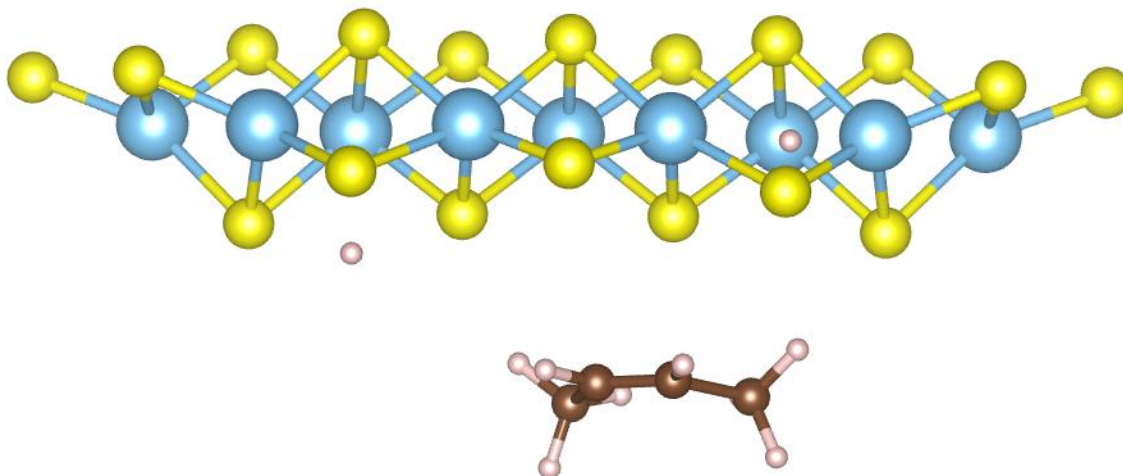
Figure S1.3. Geometry of 5', which was excluded from the energy diagram in Fig. 3.x due to the direct release of 2-butene without formation of a thiirane intermediate. ΔE_{Tot} = 8.89 kcal/mol, which is 0.77 kcal/mol higher than that of 4'.
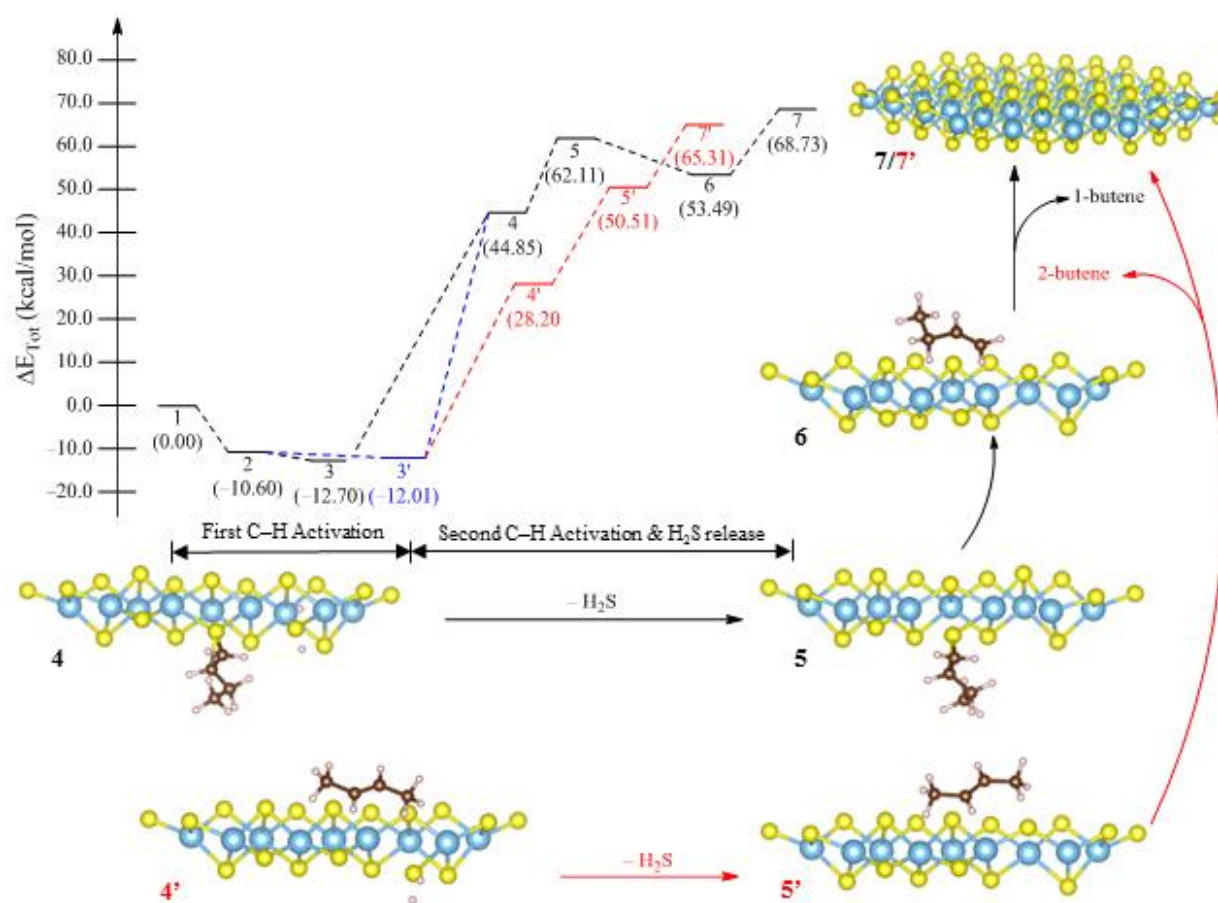
Figure S1.4. The reaction energy profile of butane dehydrogenation including H_2S production. Steps 4–7 and 4'–7' differ from the reaction energy profile given in Fig. 1.4.3. Only the geometries of the differing reaction steps are shown. ΔE_{Tot} given in kcal/mol.

Table S1.1. Energies of the optimized geometries

Compound name	Energy in kcal/mol
Cyclohexane Dehydrogenation	
A	-199969.4814
Cyclohexane	-12039.48167
B	-212019.5494
C	-212023.1428
D	-212006.5362
E	-200650.5883
Cyclohexene	-11338.75824
H2S removed mechanism	
D'	-211939.501
E'	-208929.2972
F'	-208967.6193
G'	-197611.4315
H2S	-2992.873591
Cyclohexane thiirane intermediate	-211967.808

Butane Dehydrogenation

1	-199969.4814
butane	-8699.179545
2	-208679.2637
3	-208681.3596
4	-208651.5919
5	-208657.5181
6/6'	-200650.5883
1-butene	-7995.621202
3'	-208680.6692
4'	-208660.5366
2-butene	-7999.050036

H2S removed Mechanism

4	-208623.8075
5	-205613.6794
6	-205622.2992
7/7'	-197611.4315
4'	-208640.4613

5'	-205625.2816
H2S	-2992.873591
dissociated thiirane intermediate	-208659.7686
2-methylthietane	-208318.1831
tetrahydrothiophene	-208329.1519
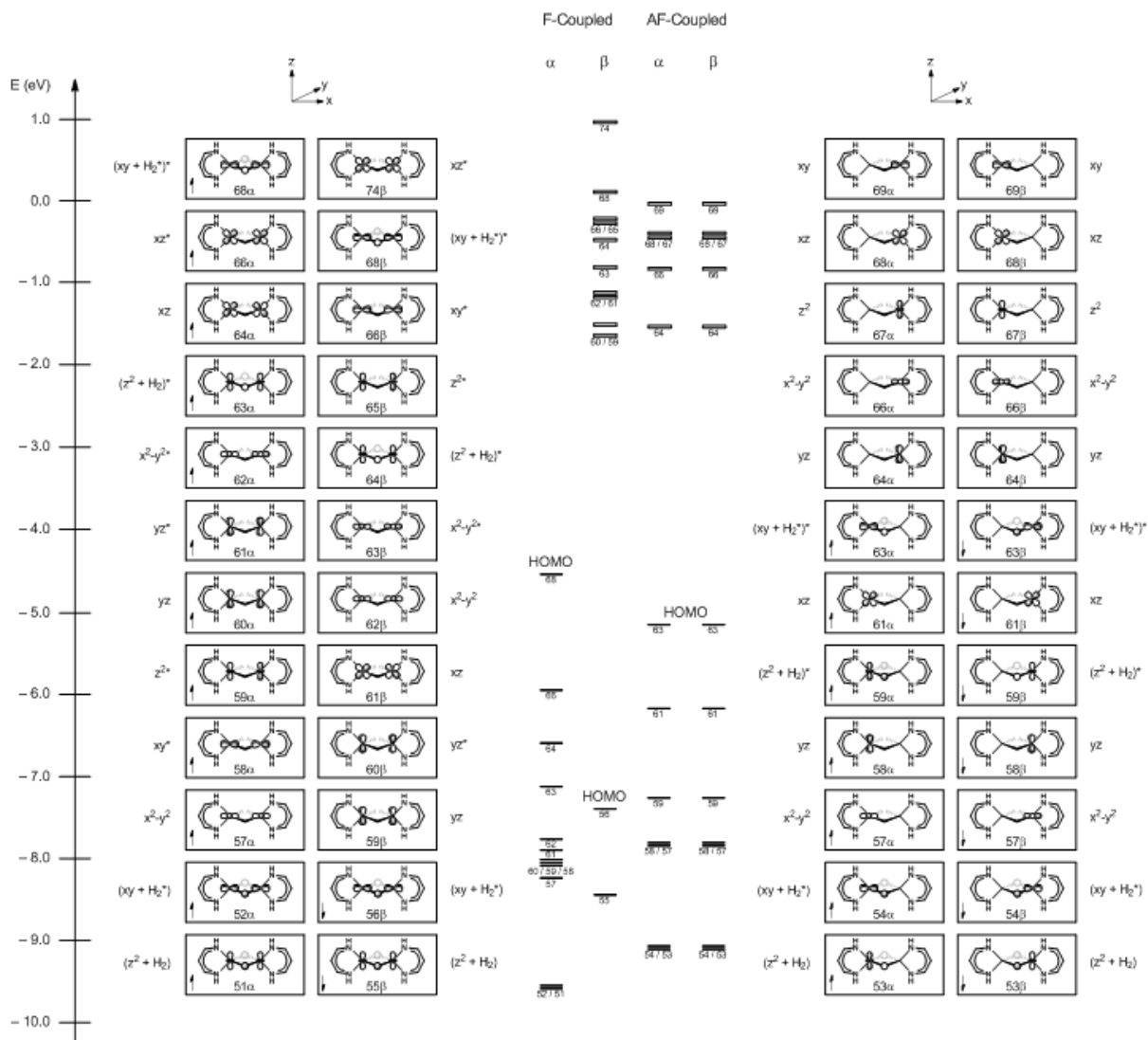
Figure S2.1. The MO-diagrams of ferro (**2-F**)- and antiferromagnetically (**2-AF**) coupled manganese centers of the model compound.
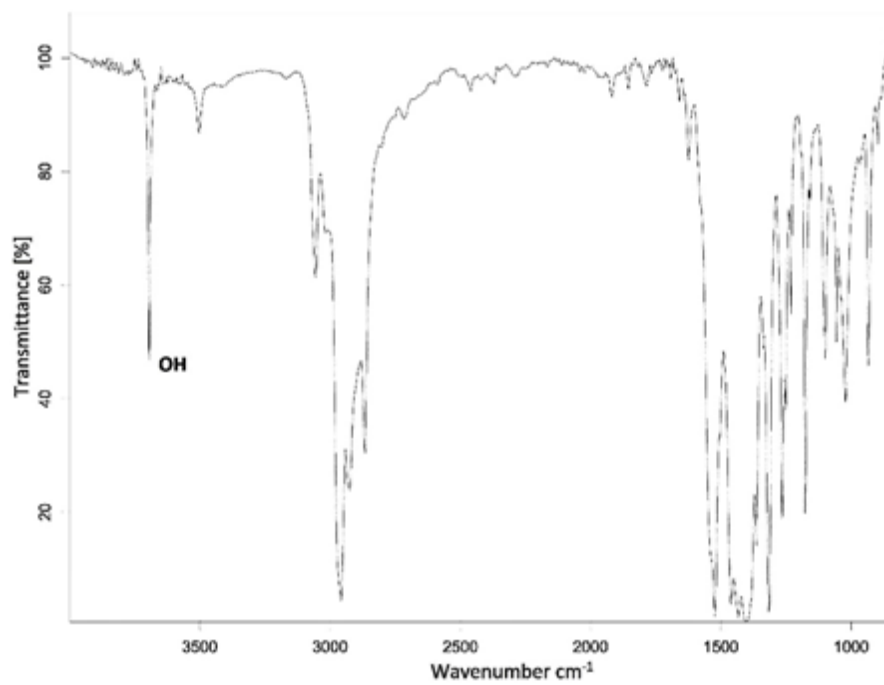
Figure S2.2. Solid-state infrared spectrum of **4** in KBr.
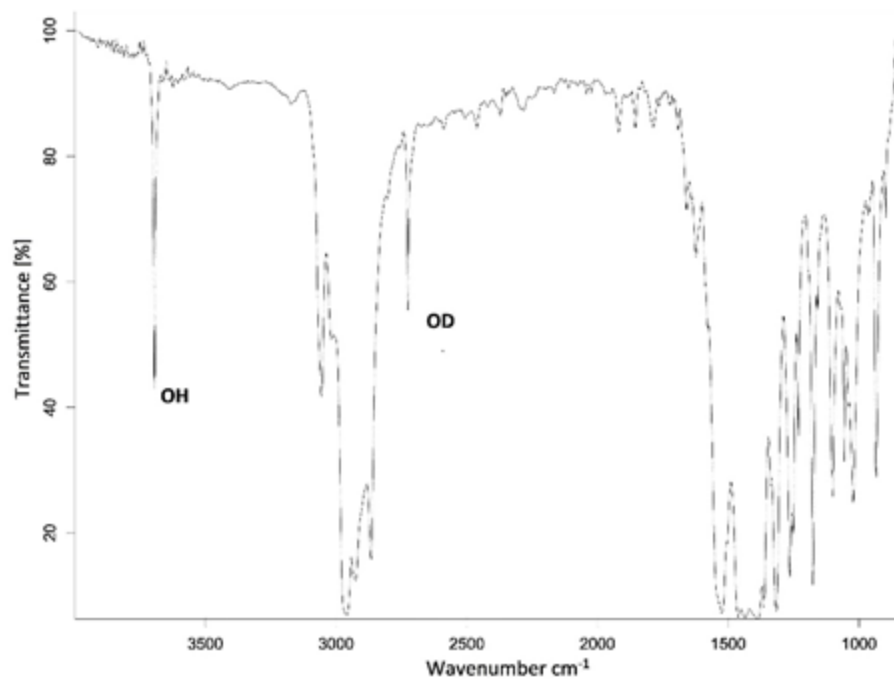
Figure S2.3. Solid-state infrared spectrum of **4-*d₂*** in KBr.

CRYSTALLOGRAPHIC DATA

Table S2.1. Crystallographic data for **4**.

	4
chemical formula	$C_{58}H_{84}Mn_2N_4O_2$
formula weight	979.17
crystal dimensions	0.193 x 0.134 x 0.073
crystal system	monoclinic
space group	C 1 2/c 1
a (Å)	22.969(3)
b (Å)	14.6534(17)
c (Å)	16.1143(19)
α (deg)	90
β (deg)	91.558(2)
γ (deg)	90
V (Å^3)	5421.6(11)
Z	4
T (°C)	123.00(10)
ρcalcd (g cm^{-3})	1.200
μ (mm^{-1})	0.509

reflections collected	22387
data/restraints/parameters	4978/0/312
R_1 [I > 2σ(I)]	0.0560
wR_2 (all data)	0.01464
Goodness-of-fit	1.028
Largest peak, hole (eÅ^{-3})	0.800, -0.294
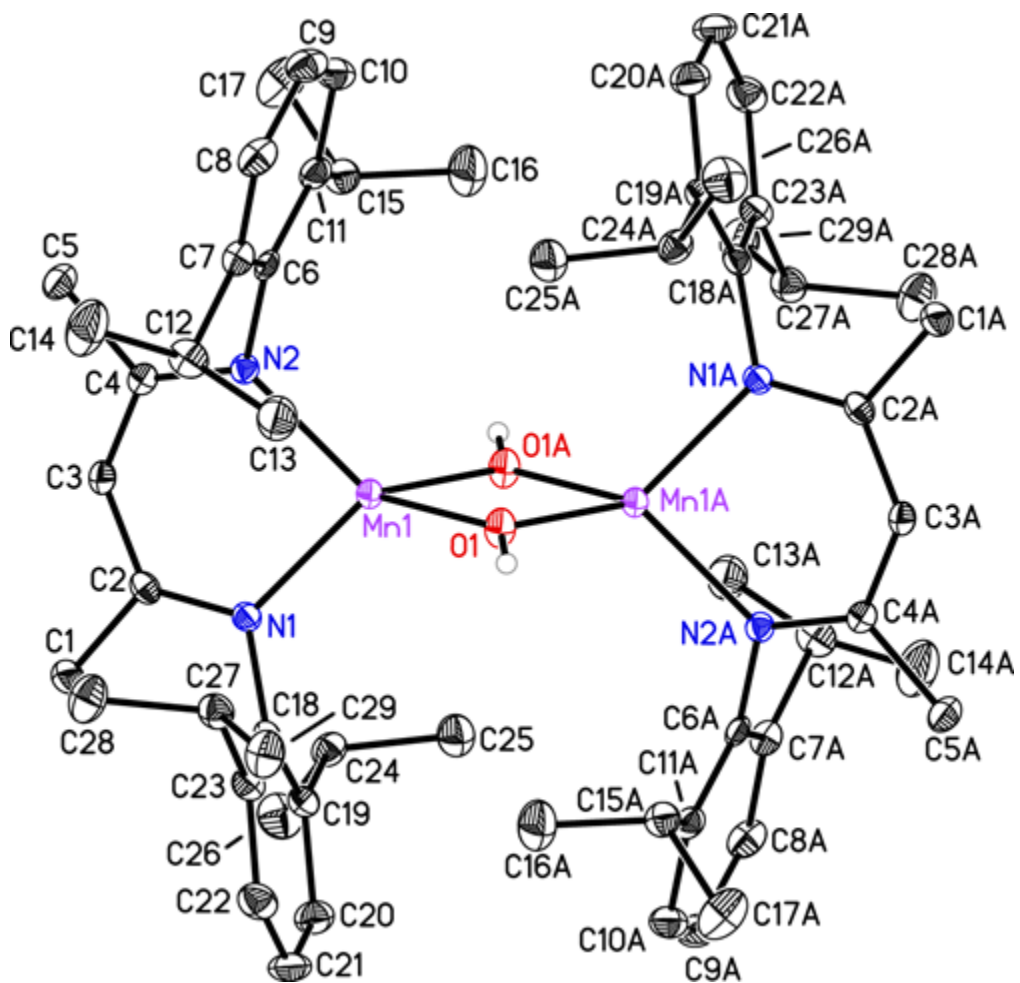
Figure S2.4. The molecular structure of **6** shown at 30% probability ellipsoids. Hydrogen atoms other than the hydroxyl hydrogens are omitted for clarity.

Table S2.2. Bond distances (Å) and angles (°) for **6**.

Mn1-O1	2.038(2)	C3-C4	1.404(4)	C15-C17	1.529(4)
Mn1-O1A	2.054(2)	C4-C5	1.514(4)	C18-C19	1.401(4)
Mn1-N2	2.106(2)	C6-C11	1.401(4)	C18-C23	1.403(4)
Mn1-N1	2.108(2)	C6-C7	1.411(4)	C19-C20	1.391(4)
Mn1-Mn1A	3.1426(9)	C7-C8	1.382(4)	C19-C24	1.511(4)
O1-Mn1A	2.054(2)	C7-C12	1.516(4)	C20-C21	1.382(5)
O1-H1	0.71(4)	C8-C9	1.382(5)	C21-C22	1.381(5)
N1-C2	1.338(4)	C9-C10	1.374(5)	C22-C23	1.396(4)
N1-C18	1.442(4)	C10-C11	1.404(4)	C23-C27	1.526(4)
N2-C4	1.333(4)	C11-C15	1.509(4)	C24-C25	1.523(4)
N2-C6	1.444(3)	C12-C13	1.497(5)	C24-C26	1.527(4)
C1-C2	1.509(4)	C12-C14	1.526(5)	C27-C29	1.520(4)
C2-C3	1.398(4)	C15-C16	1.510(5)	C27-C28	1.528(4)

O1-Mn1-O1A	79.64(10)	C2-C3-C4	130.5(3)	C16-C15-C17	109.8(3)
O1-Mn1-N2	126.96(9)	N2-C4-C3	124.5(3)	C19-C18-C23	121.8(3)
O1A-Mn1-N2	120.82(9)	N2-C4-C5	120.2(2)	C19-C18-N1	120.5(3)
O1-Mn1-N1	121.34(9)	C3-C4-C5	115.2(2)	C23-C18-N1	117.7(3)
N2-Mn1-N1	91.34(9)	C11-C6-C7	121.0(3)	C20-C19-C18	117.6(3)
O1-Mn1-Mn1A	40.01(6)	C11-C6-N2	120.0(3)	C20-C19-C24	120.4(3)
O1A-Mn1-Mn1A	39.63(6)	C7-C6-N2	119.0(2)	C18-C19-C24	122.0(3)
N2-Mn1-Mn1A	136.44(7)	C8-C7-C6	118.3(3)	C21-C20-C19	121.6(3)
N1-Mn1-Mn1A	132.01(7)	C8-C7-C12	120.7(3)	C22-C21-C20	120.1(3)
Mn1-O1-Mn1A	100.37(10)	C6-C7-C12	121.0(3)	C21-C22-C23	120.6(3)
Mn1-O1-H1	134.(3)	C9-C8-C7	121.7(3)	C22-C23-C18	118.2(3)
Mn1A-O1-H1	120.(3)	C10-C9-C8	119.7(3)	C22-C23-C27	120.4(3)
C2-N1-C18	116.5(2)	C9-C10-C11	121.3(3)	C18-C23-C27	121.4(3)
C2-N1-Mn1	121.27(18)	C6-C11-C10	118.1(3)	C19-C24-C25	111.1(3)
C18-N1-Mn1	122.24(17)	C6-C11-C15	122.0(3)	C19-C24-C26	113.4(3)
C4-N2-C6	116.5(2)	C10-C11-C15	119.8(3)	C25-C24-C26	109.3(3)
C4-N2-Mn1	121.75(19)	C13-C12-C7	110.7(3)	C29-C27-C23	113.3(3)
C6-N2-Mn1	121.69(17)	C13-C12-C14	111.2(3)	C29-C27-C28	110.2(3)
N1-C2-C3	124.5(3)	C7-C12-C14	113.3(3)	C23-C27-C28	111.4(3)
N1-C2-C1	120.1(3)	C11-C15-C16	112.1(3)		
C3-C2-C1	115.4(3)	C11-C15-C17	111.6(3)		

Table S2.3 Cartesian coordinates for the optimized geometries.

```
=============================

1-AF

=============================

 Mn   2.723259926   0.824722528  12.543914795

  N   3.887879372   0.666488707  10.799892426

  N   3.460014582   2.772720098  12.880367279

  C   5.064144135   1.534524441   8.808556557

  H   5.911763668   0.850557327   8.911772728

  H   5.429588795   2.483291388   8.412200928

  H   4.389215946   1.084841847   8.074536324

  C   4.365243435   1.730086923  10.144470215

  C   4.293539047   3.053894281  10.611359596

  H   4.670341015   3.803340435   9.927321434

  C   3.985392094   3.521960497  11.901403427

  C   4.345005989   4.978389263  12.168677330

  H   3.459956884   5.568307400  12.425725937

  H   4.819912910   5.428940773  11.295402527

  H   5.030352592   5.057542801  13.016942024

  C   4.234164238  -0.623694599  10.276488304

  C   5.392911911  -1.267320633  10.766880035

  C   5.752461433  -2.502396107  10.216547966

  H   6.651829720  -3.001324415  10.569527626

  C   4.970459461  -3.105708122   9.234244347

  H   5.256266117  -4.071871758   8.826091766

  C   3.812052727  -2.472949505   8.784880638

  H   3.198408365  -2.956530094   8.030085564
```

C   3.433377981 -1.219584703   9.279064178

C   2.197012186 -0.508449376   8.744483948

H   2.264858484   0.545280099   9.030405998

C   2.087917089 -0.569703221   7.210132599

H   2.994596958 -0.197626114   6.719680786

H   1.245449901   0.043066509   6.869757652

H   1.910429239 -1.590525389   6.854077816

C   0.933463693 -1.077190280   9.404288292

H   0.843040466 -2.149357796   9.214534760

H   0.038474958 -0.585174143   9.006937981

H   0.947939694 -0.926411450 10.487932205

C   6.275850773 -0.619523764 11.828928947

H   5.791349411   0.312518388 12.132932663

C   7.665275574 -0.259779751 11.268526077

H   8.211827278 -1.157352209 10.954485893

H   8.269366264   0.244941548 12.031515121

H   7.590364456   0.407842070 10.403627396

C   6.386680126 -1.498150110 13.088532448

H   5.399063587 -1.669793129 13.529095650

H   7.018249989 -1.013940454 13.841498375

H   6.831005573 -2.474926472 12.863499641

C   3.477206707   3.360208035 14.191028595

C   4.580194950   3.091203690 15.036626816

C   4.660137177   3.775711298 16.254352570

H   5.506322384   3.603894234 16.912418365

C   3.655318022   4.654827118 16.652698517

H   3.729692459   5.168573856 17.608024597

C   2.547202110   4.863219738 15.834165573

H   1.763609886   5.538743973   16.162830353

C   2.444401264   4.238729000   14.586422920

C   1.244848251   4.478616714   13.675973892

H   1.592563748   4.406781197   12.640219688

C   0.187305465   3.383984327   13.881717682

H   0.590559185   2.384060383   13.698792458

H   -0.657394409   3.530301571   13.198658943

H   -0.192136094   3.408232450   14.905031204

C   0.617593944   5.872742653   13.842415810

H   -0.123525098   6.045802593   13.054263115

H   1.371374607   6.666098118   13.779226303

H   0.100025460   5.975197315   14.803177834

C   5.651125431   2.078735828   14.631503105

H   5.161210537   1.330195785   13.997261047

C   6.766755104   2.727599382   13.786391258

H   7.230671883   3.558458805   14.332783699

H   6.384165287   3.111719608   12.836611748

H   7.548455715   1.994514704   13.555451393

C   6.270657063   1.338413358   15.829651833

H   6.931971073   0.541727662   15.474370003

H   5.504181385   0.885029554   16.463342667

H   6.879261017   2.004920721   16.453489304

H   2.666523218 -0.398741841   13.908930779

Mn   0.792243481 -0.839476883   13.865617752

N   -0.352500141 -0.713256121   15.618695259

N   0.018167496 -2.764876604   13.475522995

C   -1.417024851 -1.634999633   17.647844315

H   -2.237399101 -0.911937118   17.634937286

H   -1.796644568   -2.586536884   18.024570465

H   -0.674796999   -1.250488162   18.353822708

C   -0.808314323   -1.794061065   16.263944626

C   -0.789680183   -3.099305391   15.746174812

H   -1.166612267   -3.863494873   16.413692474

C   -0.531620622   -3.526739597   14.429781914

C   -0.965319335   -4.952763557   14.112009048

H   -0.112021357   -5.577094078   13.829085350

H   -1.459100366   -5.409837246   14.971342087

H   -1.656705499   -4.967281342   13.264945984

C   -0.666819453   0.565637052   16.186496735

C   -1.850969315   1.216812849   15.770269394

C   -2.174355984   2.446363926   16.354120255

H   -3.092500448   2.950199366   16.061647415

C   -1.331068397   3.041102409   17.290906906

H   -1.587972641   4.005691528   17.721416473

C   -0.152305633   2.399810076   17.667505264

H   0.506763875   2.873837709   18.389680862

C   0.189200625   1.147271752   17.145105362

C   1.442826271   0.422856539   17.616077423

H   1.372075558   -0.618019998   17.286918640

C   1.588037848   0.422477573   19.148714066

H   0.696820319   0.022324594   19.644823074

H   2.444503784   -0.193679824   19.445463181

H   1.761980414   1.430787921   19.540189743

C   2.687404394   1.023831844   16.951824188

H   2.800291777   2.078541040   17.213314056

H   3.587826967   0.491607636   17.278890610

H   2.632238388   0.948400140 15.862202644

C   -2.796150208   0.574331522 14.758543015

H   -2.301861525 -0.323811442 14.376114845

C   -4.117366791   0.133612975 15.420475006

H   -4.667429924   0.997019410 15.816075325

H   -4.764116764 -0.367468774 14.690443039

H   -3.943960905 -0.563121796 16.247520447

C   -3.058948040   1.491202235 13.549945831

H   -2.125327110   1.722031355 13.025933266

H   -3.738167048   1.003698826 12.841667175

H   -3.521736622   2.439509392 13.849021912

C   -0.035238743 -3.295195580 12.141819954

C   -1.130793333 -2.934744596 11.323457718

C   -1.277495742 -3.582622051 10.091491699

H   -2.128217697 -3.346311092   9.458933830

C   -0.339580476 -4.514632225   9.654276848

H   -0.465950519 -5.003281116   8.691364288

C   0.774359524 -4.803474426 10.441666603

H   1.509082556 -5.515166283 10.079120636

C   0.941680670 -4.216554165 11.700363159

C   2.141942024 -4.546646118 12.581286430

H   1.797381401 -4.556851864 13.620863914

C   3.214173794 -3.453293085 12.461477280

H   2.829015732 -2.465684891 12.727757454

H   4.061096191 -3.667037964 13.123560905

H   3.586320162 -3.399039030 11.437404633

C   2.754142761 -5.928000927 12.299305916

H   3.500983000 -6.167337894 13.064215660

H   1.994938731 -6.718652725 12.308190346

H   3.262361050 -5.957069397 11.328470230

C -2.138832092 -1.881517529 11.782865524

H -1.635170579 -1.249294758 12.524551392

C -3.345923185 -2.530765057 12.493032455

H -3.848127604 -3.247920990 11.829577446

H -3.036736727 -3.062603951 13.399840355

H -4.076170444 -1.767771602 12.788366318

C -2.612570286 -0.960233629 10.643782616

H -3.279227495 -0.188231006 11.043437958

H -1.766740680 -0.459230095 10.159399986

H -3.174954891 -1.507267714 9.873669624

H   0.854536891 0.375603378 12.488962173

============================

1-F

============================

Mn   2.671803474 0.852670729 12.490572929

N   3.818702459 0.752598703 10.735632896

N   3.467709541 2.769609213 12.901445389

C   4.910710812 1.681708217 8.726149559

H   5.720894337 0.947361887 8.743853569

H   5.304716110 2.631563902 8.361642838

H   4.172456264 1.310466051 8.008293152

C   4.285784721 1.835643530 10.103071213

C   4.285179138 3.132756710 10.639356613

H   4.679800034 3.900930882 9.987278938

C   4.027441502 3.541218281 11.961607933

C   4.475242138   4.956397533   12.304807663

H   3.628104925   5.582898140   12.600613594

H   4.972789764   5.423869610   11.453719139

H   5.166706085   4.947731495   13.151801109

C   4.140941143   -0.523024678   10.166646957

C   5.330584049   -1.164894581   10.578188896

C   5.654015064   -2.397552013   10.000674248

H   6.573797226   -2.897888660   10.293680191

C   4.810429096   -2.998595715   9.068494797

H   5.068974972   -3.964457273   8.642462730

C   3.629978657   -2.362248659   8.689413071

H   2.973408699   -2.839536667   7.967588902

C   3.286135912   -1.109664559   9.208888054

C   2.027221203   -0.390689790   8.743893623

H   2.110193729   0.658124089   9.043516159

C   1.853051424   -0.426140249   7.215332985

H   2.748556376   -0.068588853   6.695405483

H   1.010511756   0.207723603   6.917748928

H   1.641325593   -1.438813448   6.854476452

C   0.793345571   -0.970080972   9.447222710

H   0.688210070   -2.035237312   9.229771614

H   -0.115008712   -0.457725883   9.110843658

H   0.859580755   -0.853029728   10.533177376

C   6.277973175   -0.514968455   11.582695007

H   5.825974941   0.428055555   11.900961876

C   7.640460968   -0.184587017   10.941470146

H   8.157869339   -1.093238115   10.612242699

H   8.290218353   0.326662451   11.661228180

H   7.525976658   0.468788147   10.069944382

C   6.452149391   -1.380911231   12.844446182

H   5.503914356   -1.479093790   13.383210182

H   7.182960987   -0.926739872   13.522748947

H   6.809565544   -2.387342691   12.599396706

C   3.523333788   3.278803110   14.242914200

C   4.601836205   2.892033577   15.071432114

C   4.751220703   3.539504051   16.303815842

H   5.589219093   3.284565687   16.945384979

C   3.835867643   4.499703884   16.727920532

H   3.969275236   4.991714001   17.688098907

C   2.732208729   4.808269978   15.933427811

H   2.010015011   5.536923885   16.287418365

C   2.559464931   4.215018749   14.678866386

C   1.362334847   4.544312477   13.795164108

H   1.688283920   4.487686634   12.751071930

C   0.267997593   3.483949900   13.989418030

H   0.630473971   2.479186058   13.751456261

H   -0.591633022   3.686851025   13.341468811

H   -0.077847376   3.477636576   15.024568558

C   0.796555817   5.955436707   14.019454002

H   0.036744885   6.177681923   13.262604713

H   1.578108072   6.720655918   13.952299118

H   0.313947380   6.050115585   14.999222755

C   5.595108986   1.820183158   14.624698639

H   5.084404469   1.190010309   13.886574745

C   6.813735008   2.446966410   13.916029930

H   7.338432312   3.143229961   14.583712578

H   6.512851238   2.995301962   13.016328812

H   7.523511410   1.669037580   13.610248566

C   6.045417309   0.899006605   15.773317337

H   6.707091331   0.117602140   15.388413429

H   5.188005924   0.411756456   16.248107910

H   6.604663372   1.441962004   16.546426773

H   2.683315277   -0.404635459   13.911099434

Mn   0.805982828   -0.810366452   13.903335571

N   -0.378743798   -0.683536828   15.634849548

N   0.057366755   -2.757213116   13.541716576

C   -1.566665173   -1.570334554   17.611032486

H   -2.419714451   -0.895732582   17.488563538

H   -1.927594304   -2.524074793   17.998777390

H   -0.913980842   -1.112457037   18.359687805

C   -0.841849327   -1.754872084   16.287576675

C   -0.763022125   -3.073596239   15.809884071

H   -1.141019702   -3.830943108   16.484001160

C   -0.453390241   -3.523976088   14.514476776

C   -0.795325458   -4.981770039   14.232871056

H   0.098182477   -5.557085991   13.972415924

H   -1.266093493   -5.446041107   15.100775719

H   -1.476902127   -5.061697483   13.381791115

C   -0.736009181   0.600672007   16.162553787

C   -1.883837461   1.242033243   15.646853447

C   -2.263738632   2.471304178   16.196428299

H   -3.152323961   2.971508026   15.819621086

C   -1.515659451   3.065657377   17.210014343

H   -1.818929911   4.025234699   17.620775223

C   -0.365286022   2.436151743   17.684257507

H   0.221536726   2.914273262   18.463090897

C   0.036967251   1.192207456   17.185176849

C   1.280205846   0.496707708   17.724319458

H   1.212778091   -0.564095318   17.466312408

C   1.411077380   0.593820274   19.253839493

H   0.500905991   0.258173347   19.762702942

H   2.242953539   -0.029780760   19.599021912

H   1.618118048   1.618657827   19.581098557

C   2.530660391   1.054210305   17.030046463

H   2.605964899   2.134234190   17.177345276

H   3.437582493   0.591615558   17.436269760

H   2.508802176   0.862937927   15.952391624

C   -2.720525980   0.600898802   14.544276237

H   -2.271984339   -0.368488997   14.312418938

C   -4.166992188   0.342251450   15.004279137

H   -4.684883595   1.276411295   15.249761581

H   -4.739534855   -0.155971676   14.213606834

H   -4.192633152   -0.296929091   15.893575668

C   -2.674927235   1.437691450   13.251806259

H   -1.651842594   1.498376369   12.865639687

H   -3.303877115   0.986403108   12.476373672

H   -3.036721945   2.458283901   13.421918869

C   0.051804427   -3.334108591   12.226818085

C   -1.054256558   -3.078983068   11.380638123

C   -1.121762395   -3.762099743   10.161383629

H   -1.968234301   -3.600421190   9.501749039

C   -0.108445838   -4.633192539   9.766963959

H   -0.177289844   -5.150106907   8.813285828

C   1.001994967   -4.826228142   10.585482597

H   1.794547796   -5.491831303   10.258756638

C   1.097348452   -4.196300983   11.830956459

C   2.299563169   -4.419299126   12.741021156

H   1.966029882   -4.293903828   13.775897026

C   3.368593216   -3.350142717   12.472782135

H   2.980901241   -2.340833902   12.638648033

H   4.229299068   -3.486568451   13.136781693

H   3.718240261   -3.409909248   11.440908432

C   2.899464130   -5.829868793   12.626521111

H   3.659247398   -5.977481842   13.401626587

H   2.134154081   -6.604590416   12.746504784

H   3.389828682   -5.987958908   11.659235954

C   -2.148167372   -2.093954802   11.792525291

H   -1.668890238   -1.323177934   12.407609940

C   -3.230115414   -2.765833378   12.663347244

H   -3.686181545   -3.607966185   12.128779411

H   -2.821552753   -3.136826515   13.606157303

H   -4.024293423   -2.050643206   12.906935692

C   -2.812569618   -1.388134241   10.599057198

H   -3.490684509   -0.607726276   10.958464622

H   -2.073226929   -0.919453859   9.945858955

H   -3.412110090   -2.080074787   9.995950699

H   0.794907331   0.451902509   12.499654770

==============================

2-F

==============================

Mn -0.321517855   0.011642214   0.006508314

N -1.776808619   1.482091904   0.019861802

N -1.759084225 -1.476462483   0.007912308

C -3.081608295   1.243887782   0.033342633

C -3.709584951 -0.009433459   0.034285914

H -4.793556213 -0.015896661   0.045610305

C -3.066557407 -1.255232453   0.021262357

H   1.072514415   0.015487185 -1.264904499

Mn   2.480552435 -0.000146741 -0.009902298

N   3.923375607 -1.482787967 -0.016694520

N   3.928359509   1.476670742 -0.010384298

C   5.229835987 -1.254671335 -0.015669178

C   5.867259026 -0.005931515 -0.013270819

H   6.951242924 -0.007798287 -0.013577412

C   5.234044552   1.244906425 -0.011087477

H   1.087765574   0.003412989   1.261625767

H -1.574066758   2.477013826   0.022404615

H -1.542908669 -2.468556881 -0.000701239

H -3.753349781   2.108015060   0.044237174

H -3.727649689 -2.127635002   0.022633223

H   5.901741505   2.112210512 -0.009822653

H   5.894956589 -2.123934031 -0.017124245

H   3.719981194   2.470474958 -0.008545796

H   3.712369442 -2.475991011 -0.017730325

==============================

3-AF

==============================

Mn   1.536853433 -0.002816108 -0.001331776

 N   2.972986221   0.000087639 -1.501008272

 N   2.974089861   0.000694503   1.497483253

 C   4.277062416   0.003426941 -1.256575942

 C   4.905618191   0.005635753 -0.002449264

 H   5.989875793   0.008472881 -0.002815822

 C   4.277950287   0.004376190   1.252161145

Mn -1.537081838 -0.002371454   0.004037745

 N -2.976122141 -0.000347435   1.500521302

 N -2.970732212   0.001017200 -1.498311281

 C -4.279667854   0.003420433   1.253032446

 C -4.905416489   0.005662850 -0.002446291

 H -5.989673138   0.008590785 -0.004443366

 C -4.275086880   0.004362116 -1.255763531

 H   2.774727345 -0.000902191 -2.496736526

 H   2.776460648   0.000534205   2.493336678

 H   4.952751637   0.004815585 -2.118042469

 H   4.954297066   0.006510354   2.113108397

 H -4.949654579   0.006347666 -2.118106842

 H -4.957302570   0.004796400   2.112959623

 H -2.770867586   0.000758979 -2.493713379

 H -2.780195236 -0.001358095   2.496700525

 F   0.000245807   1.306462526 -0.000070002

 F -0.000061872 -1.311558604   0.001761840

==============================

3-MONO

====================================

Mn   1.507197499   -0.003370051   -0.085591353

N   2.996810436   0.000157701   -1.529242516

N   2.918253422   0.001207822   1.430596828

C   4.297786236   0.003774119   -1.263846159

C   4.898715019   0.005701877   0.002641021

H   5.982365608   0.008601150   0.030895056

C   4.231933117   0.004367821   1.235117912

H   2.815907240   -0.000589643   -2.528762579

H   2.684020042   0.000723898   2.418947220

H   4.987904549   0.005391237   -2.113263607

H   4.875191212   0.006218741   2.120393991

F   -0.288707703   -0.008372472   -0.152356222

====================================

4-AF

====================================

Mn   1.550173759   0.005637465   -0.003861207

N   3.028614521   0.001033878   -1.496230245

N   3.028241396   -0.000922114   1.490118265

C   4.332232952   -0.006864399   -1.255720258

C   4.962634087   -0.011964817   -0.002629475

H   6.047181129   -0.018586395   -0.002487958

C   4.331793308   -0.008805839   1.250522971

Mn   -1.550244927   0.004598741   0.005929548

N   -3.031670332   0.001425642   1.495236874

N   -3.025042534   -0.001666134   -1.491274357

C   -4.334794521   -0.006542944   1.252018332

```
C    -4.962541103   -0.011686628   -0.002410997

H    -6.047086239   -0.017930008   -0.004732670

C    -4.329101563   -0.008932894   -1.254224658

H     2.830842972    0.003998750   -2.492306709

H     2.829401255   -0.000638854    2.486014843

H     5.008523941   -0.009872790   -2.117779255

H     5.007816792   -0.013523866    2.112822533

H    -5.003360748   -0.013358828   -2.117872953

H    -5.012847424   -0.009492698    2.112704515

H    -2.824199200   -0.000880627   -2.486753702

H    -2.835917950    0.003556580    2.491733551

O     0.000469001   -1.325718284    0.001859942

O    -0.000213242    1.335972667    0.003626881

H    -0.003302211    2.296551228   -0.001357182

H    -0.001865991   -2.286303997   -0.001777300
```

============================

4-MONO

============================

```
Mn    1.546733618    0.115695909    0.058089212

N     2.914332628    0.010028411   -1.493124723

N     3.064009428   -0.044520084    1.470407128

C     4.226371765   -0.119435579   -1.324185133

C     4.917951584   -0.201275960   -0.109383322

H     5.995775223   -0.303461105   -0.165871158

C     4.350570202   -0.164141998    1.173425078

H     2.667340040    0.043301772   -2.477492332

H     2.904947996   -0.043748718    2.473585367
```

H   4.848714352 -0.168287382 -2.223345041

H   5.059186459 -0.243141830   2.004181623

O -0.260846406   0.307220459   0.374086410

H -0.978728175   0.373132557 -0.262217581

===============================

5-AF

===============================

Mn 2.719877005   1.042344928 12.477032661

N   3.809989214   0.909979761 10.707489014

N   3.509817600   2.942745447 12.816307068

C   5.105800152   1.690071583   8.764772415

H   5.946949959   1.005831838   8.918498039

H   5.487339497   2.620483637   8.340620995

H   4.446351051   1.212521672   8.033736229

C   4.386816502   1.935944915 10.079250336

C   4.419280529   3.248795986 10.583409309

H   4.876586437   3.986155987   9.936060905

C   4.081319809   3.700364351 11.872106552

C   4.449725628   5.140879154 12.191756248

H   3.553193331   5.744490147 12.362701416

H   5.019533157   5.590867043 11.376927376

H   5.043724537   5.196135044 13.108016014

C   4.019946098 -0.411122143 10.201565742

C   5.119856358 -1.153603077 10.687289238

C   5.300953388 -2.452569962 10.201221466

H   6.140710354 -3.043339014 10.558252335

C   4.409079552 -3.007998466   9.286142349

H   4.554579258   -4.026412487   8.935008049

C   3.325607538   -2.262741327   8.824928284

H   2.635404110   -2.709167719   8.115844727

C   3.124095917   -0.946342528   9.251395226

C   1.989888072   -0.092543110   8.695844650

H   2.246118069   0.955541134   8.875207901

C   1.811813593   -0.267480165   7.178141594

H   2.755542517   -0.121621110   6.640983105

H   1.085863471   0.458760738   6.796307087

H   1.435227990   -1.265084267   6.928054810

C   0.669508278   -0.368612111   9.431565285

H   0.386652380   -1.417692661   9.316908836

H   -0.132107690   0.253888547   9.015081406

H   0.732604444   -0.153163478 10.501447678

C   6.084502697   -0.561618626 11.713168144

H   5.822972775   0.491889924 11.847434044

C   7.544500828   -0.611714959 11.230275154

H   7.902581215   -1.642170310 11.126756668

H   8.200135231   -0.105280988 11.947765350

H   7.662677765   -0.119588174 10.258891106

C   5.932906628   -1.242541671 13.087256432

H   4.920454502   -1.121106744 13.481073380

H   6.635409832   -0.806318820 13.807605743

H   6.144157887   -2.315740585 13.019341469

C   3.384614706   3.491204262 14.133076668

C   4.367858410   3.162303448 15.098508835

C   4.246834278   3.734517336 16.369754791

H   4.987899780   3.515707731 17.131275177

C   3.174794197   4.567175865   16.688453674

H   3.097555399   4.991379738   17.686372757

C   2.197888613   4.845026970   15.736586571

H   1.356801271   5.477642059   16.003299713

C   2.288068056   4.325366020   14.441611290

C   1.222483397   4.630443096   13.393140793

H   1.657528043   4.445333004   12.407305717

C   0.028246114   3.674289703   13.542283058

H   0.331000149   2.627953529   13.454502106

H   -0.721760035   3.867536306   12.766060829

H   -0.447294921   3.799048662   14.517781258

C   0.758597136   6.095819950   13.416649818

H   0.100568131   6.296109200   12.564237595

H   1.606067538   6.787666798   13.363411903

H   0.192651972   6.331166744   14.324665070

C   5.505996227   2.193203449   14.758059502

H   5.056509972   1.364478707   14.194305420

C   6.591345787   2.819523096   13.856530190

H   7.011361599   3.716195107   14.327669144

H   6.213290215   3.089597225   12.870417595

H   7.410575390   2.106110096   13.707101822

C   6.192214489   1.584665298   15.992357254

H   6.875520229   0.789299011   15.676692009

H   5.478705406   1.152633190   16.695188522

H   6.791160107   2.331307173   16.527688980

Mn   0.751344442 -1.041787744   13.921784401

N   -0.293775678 -0.950545251   15.714181900

N   -0.051008798 -2.934325457   13.556325912

C   -1.540016770   -1.758022666   17.673875809

H   -2.363847733   -1.042917848   17.577985764

H   -1.932548523   -2.689483404   18.085485458

H   -0.833568454   -1.324774623   18.388843536

C   -0.878025770   -1.982005358   16.326866150

C   -0.958982885   -3.276271343   15.783856392

H   -1.423284888   -4.020913601   16.417823792

C   -0.641384482   -3.701338291   14.480291367

C   -1.046089411   -5.124111176   14.125711441

H   -0.164694592   -5.746035576   13.941617966

H   -1.627989292   -5.578615665   14.929413795

H   -1.639654279   -5.143736839   13.207883835

C   -0.462075830   0.362045109   16.258510590

C   -1.577702880   1.126778245   15.844652176

C   -1.706490993   2.425534725   16.346086502

H   -2.554285526   3.033565760   16.040996552

C   -0.749988973   2.962244034   17.205926895

H   -0.854593098   3.982175112   17.566764832

C   0.342466414   2.194187403   17.601808548

H   1.086035848   2.625257015   18.265508652

C   0.494986206   0.876302302   17.158491135

C   1.646988869   0.008408807   17.650930405

H   1.414299250   -1.029125571   17.393762589

C   1.814192414   0.079534210   19.179237366

H   0.875206769   -0.139721379   19.699224472

H   2.565393686   -0.645177245   19.512294769

H   2.150796175   1.070303559   19.503622055

C   2.960941792   0.373756021   16.943080902

H   3.208174467   1.424290299   17.119300842

H   3.782222033   -0.244866997   17.325498581

H   2.902266026   0.216779038   15.862737656

C   -2.605686426   0.560632050   14.867069244

H   -2.392978191   -0.503840506   14.736573219

C   -4.043162346   0.675334811   15.402070045

H   -4.359952927   1.719984889   15.496718407

H   -4.742959023   0.180853367   14.718985558

H   -4.142657757   0.206111073   16.386781693

C   -2.480309010   1.220044732   13.479643822

H   -1.482443571   1.078917027   13.055589676

H   -3.212151527   0.790080428   12.785403252

H   -2.668833494   2.297714233   13.541609764

C   0.067339122   -3.451033831   12.225824356

C   -0.907759070   -3.083062172   11.266448021

C   -0.797365606   -3.631816864   9.983868599

H   -1.533371568   -3.382133722   9.226904869

C   0.263077915   -4.471176624   9.645720482

H   0.335754365   -4.871947289   8.637825012

C   1.235560894   -4.784456730   10.590963364

H   2.066451311   -5.424179077   10.310093880

C   1.148627877   -4.298419952   11.899306297

C   2.200133562   -4.652534962   12.945676804

H   1.750036955   -4.515648842   13.931964874

C   3.393978119   -3.688988924   12.860116959

H   3.089243412   -2.646704435   12.982643127

H   4.131056786   -3.912650824   13.640579224

H   3.885801077   -3.773809433   11.889226913

C   2.666460752 -6.114543915 12.856964111

H   3.311318874 -6.356202602 13.708791733

H   1.818227410 -6.807543278 12.862837791

H   3.246934175 -6.304066658 11.947397232

C   -2.022166491 -2.091917276 11.619813919

H   -1.557998061 -1.296755075 12.218042374

C   -3.144122839 -2.711788893 12.480248451

H   -3.584526539 -3.578370571 11.972793579

H   -2.791618586 -3.026710272 13.462524414

H   -3.942324400 -1.977183104 12.640605927

C   -2.657069206 -1.416689992 10.393536568

H   -3.319707394 -0.609123647 10.722007751

H   -1.909218311 -0.985880554   9.725485802

H   -3.267211914 -2.121540546   9.816007614

F   2.743005037 -0.523192227 13.788331985

F   0.728154540   0.520799339 12.606398582

==============================

5-MONO

==============================

Mn   0.003867419 -0.856813848 13.718017578

N   -0.626605213 -0.843976736 15.665466309

N   -0.306164235 -2.877095938 13.586372375

C   -1.571308613 -1.673946023 17.769773483

H   -2.393242359 -0.949891925 17.772716522

H   -1.917009592 -2.602671862 18.226522446

H   -0.779167652 -1.246157169 18.393356323

C   -1.075214028 -1.895308375 16.354587555

C   -1.135098696   -3.204744339   15.837500572

H   -1.514294505   -3.958556414   16.516099930

C   -0.794520378   -3.662279844   14.548759460

C   -1.017084599   -5.130415916   14.242775917

H   -0.073800318   -5.613143921   13.965880394

H   -1.446245193   -5.660016537   15.094870567

H   -1.685733438   -5.240487576   13.382472038

C   -0.648384452   0.473894387   16.222747803

C   -1.739448667   1.322105527   15.928804398

C   -1.700964212   2.638617992   16.401039124

H   -2.528185129   3.307448864   16.179430008

C   -0.616232872   3.107951403   17.135852814

H   -0.603272200   4.134350300   17.492176056

C   0.461109132   2.264267921   17.401983261

H   1.309868574   2.646417856   17.961053848

C   0.468729913   0.940711319   16.952785492

C   1.681761026   0.040757220   17.162939072

H   1.345260262   -0.997892976   17.089307785

C   2.342447281   0.212684602   18.539127350

H   1.612805128   0.094773479   19.346916199

H   3.129831791   -0.536024868   18.677022934

H   2.808982611   1.197418213   18.650037766

C   2.706682444   0.266859561   16.032516479

H   3.082861900   1.295647502   16.049539566

H   3.558604479   -0.415684760   16.127548218

H   2.257891178   0.107100464   15.044000626

C   -2.902539968   0.847074270   15.064360619

H   -2.768312454   -0.225431755   14.888234138

C   -4.261256695   1.030057073   15.761696815

H   -4.487356663   2.088164806   15.933702469

H   -5.066203594   0.617405713   15.143542290

H   -4.283173561   0.522536874   16.732229233

C   -2.875990868   1.544419646   13.688637733

H   -1.919720054   1.389892936   13.177405357

H   -3.675354719   1.153680801   13.047799110

H   -3.030056238   2.623986721   13.797701836

C   -0.020174906   -3.390725136   12.281807899

C   -0.986143231   -3.245422602   11.261565208

C   -0.653215766   -3.667202950   9.969600677

H   -1.381759763   -3.558460712   9.170741081

C   0.597125530   -4.210506916   9.689635277

H   0.837561607   -4.531352520   8.679745674

C   1.546949744   -4.329457283   10.703135490

H   2.525746584   -4.737179756   10.469073296

C   1.261596203   -3.923293591   12.009590149

C   2.326822519   -3.964589119   13.100245476

H   1.817623615   -3.975064516   14.068413734

C   3.176745653   -2.679020405   13.051771164

H   2.552206278   -1.780632257   13.134909630

H   3.907399893   -2.655962944   13.868033409

H   3.716205120   -2.606183529   12.101071358

C   3.222262859   -5.211674690   13.038788795

H   3.889996290   -5.241208553   13.906460762

H   2.625027180   -6.129370689   13.035715103

H   3.853495598   -5.219675541   12.143706322

C   -2.335095882   -2.588812113   11.535321236

H -2.413246632 -2.430121183 12.616118431

C -3.515036106 -3.482762814 11.118472099

H -3.529280901 -3.652927399 10.036242485

H -3.467831850 -4.460904598 11.609345436

H -4.465803146 -3.010905027 11.390215874

C -2.411548853 -1.203720450 10.859609604

H -3.364179850 -0.715904951 11.097478867

H -1.599072695 -0.547926843 11.190375328

H -2.346256018 -1.300151825 9.769816399

F   0.083910331   0.445152700 12.448922157

============================

6-AF

============================

Mn 2.603049040 0.942815065 12.338946342

N   3.771000862 0.851995707 10.587359428

N   3.359487295 2.887943506 12.707058907

C   4.976667404 1.727796435 8.622960091

H   5.806558132 1.019898415 8.710571289

H   5.363132954 2.673485041 8.238656998

H   4.285552979 1.306264520 7.886300087

C   4.284576893 1.915648699 9.963006973

C   4.259373665 3.225181341 10.475719452

H   4.675431252 3.985405684 9.826502800

C   3.909876108 3.662759304 11.768692017

C   4.230837822 5.115890503 12.086330414

H   3.310892820 5.695005417 12.213193893

H   4.818562984 5.573534489 11.288429260

H   4.786054611   5.199266434   13.024188042

C   4.081522465   -0.447268963   10.072502136

C   5.221220493   -1.113655329   10.579196930

C   5.539498329   -2.373346090   10.063244820

H   6.420091629   -2.893867016   10.431708336

C   4.735375881   -2.977816343   9.098257065

H   4.990498066   -3.962715149   8.715396881

C   3.594442844   -2.324233055   8.636834145

H   2.961350918   -2.810274363   7.899567604

C   3.256265879   -1.046921134   9.097418785

C   2.024513006   -0.324792802   8.566126823

H   2.096049309   0.722564876   8.873980522

C   1.934106350   -0.355337083   7.030529976

H   2.851102114   0.017454633   6.561625957

H   1.099722624   0.266941905   6.688062191

H   1.758530259   -1.369874835   6.655962944

C   0.750193834   -0.907377243   9.196145058

H   0.636406302   -1.962546825   8.938651085

H   -0.136425227   -0.374425918   8.830522537

H   0.772294104   -0.832423985   10.286846161

C   6.084763527   -0.477931798   11.665171623

H   5.619643211   0.471751273   11.942790985

C   7.503990650   -0.162871003   11.160227776

H   8.031085968   -1.074548125   10.855902672

H   8.095713615   0.319540590   11.946968079

H   7.478697300   0.512246013   10.298612595

C   6.127667427   -1.352651358   12.931069374

H   5.115669250   -1.549479365   13.296227455

H   6.692767143 -0.852700889 13.725954056

H   6.604238987 -2.320941687 12.739538193

C   3.229781389 3.420454025 14.029513359

C   4.227919579 3.103712797 14.984202385

C   4.117020607 3.666165829 16.260057449

H   4.874425888 3.456922293 17.008386612

C   3.029983044 4.468802929 16.603483200

H   2.956318378 4.882493973 17.606155396

C   2.032253504 4.726133823 15.668062210

H   1.176100016 5.330393314 15.953009605

C   2.119292021 4.225050449 14.364764214

C   1.031711221 4.528085232 13.340091705

H   1.436958313 4.314566135 12.347145081

C   -0.169911623 3.593289614 13.544952393

H   0.128841370 2.544753551 13.464462280

H   -0.944009483 3.785529852 12.791718483

H   -0.612472057 3.738430738 14.533564568

C   0.589440703 6.001297951 13.352100372

H   -0.097383253 6.195263863 12.520754814

H   1.441941023 6.682387829 13.256096840

H   0.060511235 6.259592056 14.276079178

C   5.380603313 2.163257837 14.622190475

H   4.948529243 1.361842752 14.008195877

C   6.473994732 2.846899986 13.774513245

H   6.874491692 3.722277641 14.299561501

H   6.103978634 3.166135788 12.799667358

H   7.304523945 2.153088808 13.597403526

C   6.037341595 1.499253631 15.843165398

H   6.740595818   0.727627277   15.511972427

H   5.303013802   1.029188991   16.500419617

H   6.610371113   2.221567392   16.436384201

Mn   0.568059325   -0.954096913   13.898471832

N   -0.533041060   -0.850544989   15.699741364

N   -0.285279751   -2.851070881   13.532521248

C   -1.762055516   -1.688834071   17.662942886

H   -2.581225872   -0.966997087   17.584915161

H   -2.159984827   -2.625540018   18.057352066

H   -1.052321076   -1.275815368   18.385805130

C   -1.101901412   -1.892435074   16.310091019

C   -1.166200161   -3.189508200   15.770253181

H   -1.614387751   -3.938311815   16.411228180

C   -0.856210887   -3.617513180   14.465742111

C   -1.227374196   -5.053443432   14.129137993

H   -0.325329483   -5.650373936   13.959782600

H   -1.800577044   -5.513809204   14.935869217

H   -1.812860966   -5.102922440   13.207813263

C   -0.707988918   0.450315773   16.268743515

C   -1.827988863   1.218945861   15.875704765

C   -1.963052630   2.509492636   16.397161484

H   -2.818419933   3.114836216   16.107294083

C   -1.009313226   3.039001226   17.264019012

H   -1.119855762   4.051815987   17.643077850

C   0.085167579   2.266898870   17.646411896

H   0.826724648   2.686411619   18.320426941

C   0.243280604   0.957857013   17.180095673

C   1.400365472   0.093741037   17.665975571

H   1.220695019 -0.926679790 17.314956665

C   1.488890529   0.052216578 19.202859879

H   0.541693926 -0.256752312 19.657522202

H   2.264382362 -0.653988361 19.520669937

H   1.749634743   1.032884240 19.616184235

C   2.732456446   0.560781419 17.063869476

H   2.977178097   1.573913574 17.393932343

H   3.544393063 -0.107489444 17.377216339

H   2.690371275   0.573522031 15.971749306

C   -2.877148867   0.657494009 14.918837547

H   -2.631855488 -0.391262084 14.731747627

C   -4.291967869   0.702082634 15.522982597

H   -4.631369114   1.731961370 15.680742264

H   -5.009407997   0.217069417 14.851099014

H   -4.332258224   0.187418953 16.488500595

C   -2.842632771   1.378222108 13.559217453

H   -1.861991286   1.267698526 13.088830948

H   -3.599677086   0.964053988 12.883426666

H   -3.039223909   2.450262070 13.671390533

C   -0.228113472 -3.363684893 12.198098183

C   -1.261231184 -3.001921415 11.300975800

C   -1.261556149 -3.581438303 10.028652191

H   -2.056303024 -3.343147755   9.328618050

C   -0.236403048 -4.438153744   9.628770828

H   -0.248761967 -4.870796680   8.631561279

C   0.817871809 -4.713874340 10.495565414

H   1.631773710 -5.351004601 10.161429405

C   0.836304724 -4.197916985 11.796387672

```
C    1.983975410  -4.513321400  12.748340607

H    1.645307899  -4.288570881  13.763960838

C    3.183234930  -3.596194506  12.453793526

H    2.915504456  -2.541521549  12.564490318

H    4.011919975  -3.809088945  13.140628815

H    3.543662071  -3.743227482  11.433072090

C    2.402631521  -5.992838383  12.715946198

H    3.139748335  -6.193496704  13.501329422

H    1.547962427  -6.659950733  12.872776985

H    2.864958763  -6.263837814  11.760385513

C   -2.337116480  -2.003795862  11.726387978

H   -1.867684484  -1.318092823  12.442288399

C   -3.511766434  -2.678057671  12.461580276

H   -3.986466646  -3.431838989  11.822127342

H   -3.186262846  -3.163800716  13.384059906

H   -4.272032738  -1.934089065  12.729351044

C   -2.859880924  -1.152761221  10.558224678

H   -3.506222010  -0.353839308  10.936095238

H   -2.038939953  -0.693572640   9.999393463

H   -3.456509352  -1.744072318   9.854543686

O    0.594823420   0.438339919  12.383190155

H   -0.101620466   0.700492680  11.774504662

O    2.584591866  -0.484357446  13.818829536

H    3.296964407  -0.826352000  14.365790367
```

==============================

6-MONO

==============================

Mn   0.005179527 -0.823412001 13.704684258

N   -0.629300654 -0.835652292 15.659189224

N   -0.303017169 -2.850777864 13.567411423

C   -1.569416523 -1.677923679 17.760585785

H   -2.393225193 -0.956118584 17.775888443

H   -1.908984065 -2.610122204 18.215118408

H   -0.772026002 -1.252243996 18.379161835

C   -1.083516002 -1.889251232 16.340402603

C   -1.150066018 -3.192414045 15.811742783

H   -1.538879037 -3.950246096 16.480497360

C   -0.802978039 -3.639234781 14.520083427

C   -1.023731589 -5.105853081 14.204523087

H   -0.080256715 -5.583872795 13.920087814

H   -1.448214650 -5.642279625 15.054702759

H   -1.695782781 -5.211623192 13.346236229

C   -0.634922922   0.476173639 16.225339890

C   -1.729110837   1.332426906 15.963718414

C   -1.663848162   2.652240992 16.423036575

H   -2.492640257   3.326478720 16.224290848

C   -0.551745653   3.117869377 17.119800568

H   -0.518253922   4.147068977 17.466762543

C   0.522706330   2.264063358 17.364208221

H   1.390476227   2.640217304 17.898170471

C   0.503912091   0.936411917 16.926111221

C   1.708125710   0.022655040 17.128265381

H   1.365266442 -1.009925961 17.014183044

C   2.337988853   0.146607876 18.524517059

H   1.590872765 -0.000300122 19.311428070

H   3.123204470 -0.606012106 18.653755188

H   2.799838066   1.127494097 18.680667877

C   2.758300543   0.275382370 16.027992249

H   3.141479492   1.300472736 16.085742950

H   3.604218483 -0.414341390 16.124492645

H   2.331532478   0.144400269 15.026027679

C -2.927198648   0.856110454 15.148281097

H -2.812470675 -0.220620051 14.988870621

C -4.260669231   1.073094964 15.883483887

H -4.472363472   2.137619257 16.032661438

H -5.088582993   0.651050985 15.303195000

H -4.255949974   0.593382955 16.868124008

C -2.940976381   1.524379015 13.758163452

H -2.011673689   1.329220414 13.211338997

H -3.773920774   1.143686533 13.155749321

H -3.059303522   2.610313892 13.849712372

C   0.002730114 -3.372396231 12.270207405

C -0.949311614 -3.247611046 11.234997749

C -0.593428969 -3.678353071   9.952197075

H -1.310367703 -3.583087683   9.141192436

C   0.665350139 -4.214112282   9.696271896

H   0.924385488 -4.541289330   8.692951202

C   1.599303842 -4.318158150 10.726044655

H   2.584352493 -4.722275734 10.511997223

C   1.290578127 -3.901795626 12.023982048

C   2.335996628 -3.937807322 13.133926392

H   1.808396459 -3.905486822 14.091876030

C   3.225044727 -2.679469585 13.062407494

H   2.627002239 -1.761019111 13.096560478

H   3.936678171 -2.651237965 13.895579338

H   3.790830135 -2.658128023 12.124204636

C   3.193334579 -5.213126659 13.126543045

H   3.846796036 -5.234976292 14.005429268

H   2.568394423 -6.112204552 13.143150330

H   3.837654114 -5.269437313 12.242552757

C   -2.309530258 -2.605140686 11.483937263

H   -2.403704643 -2.436995983 12.561883926

C   -3.472830057 -3.517903090 11.059995651

H   -3.470344305 -3.699387550   9.979516983

H   -3.420285463 -4.490669727 11.561082840

H   -4.433168411 -3.055640936 11.314092636

C   -2.393916368 -1.227623582 10.794611931

H   -3.349562645 -0.742385387 11.027252197

H   -1.582504153 -0.565995693 11.118410110

H   -2.327666759 -1.334724545   9.705533981

O   0.258020401   0.485319227 12.404191017

H   0.351406425   1.427744865 12.578169823

Table S2.4. Energies of the optimized geometries

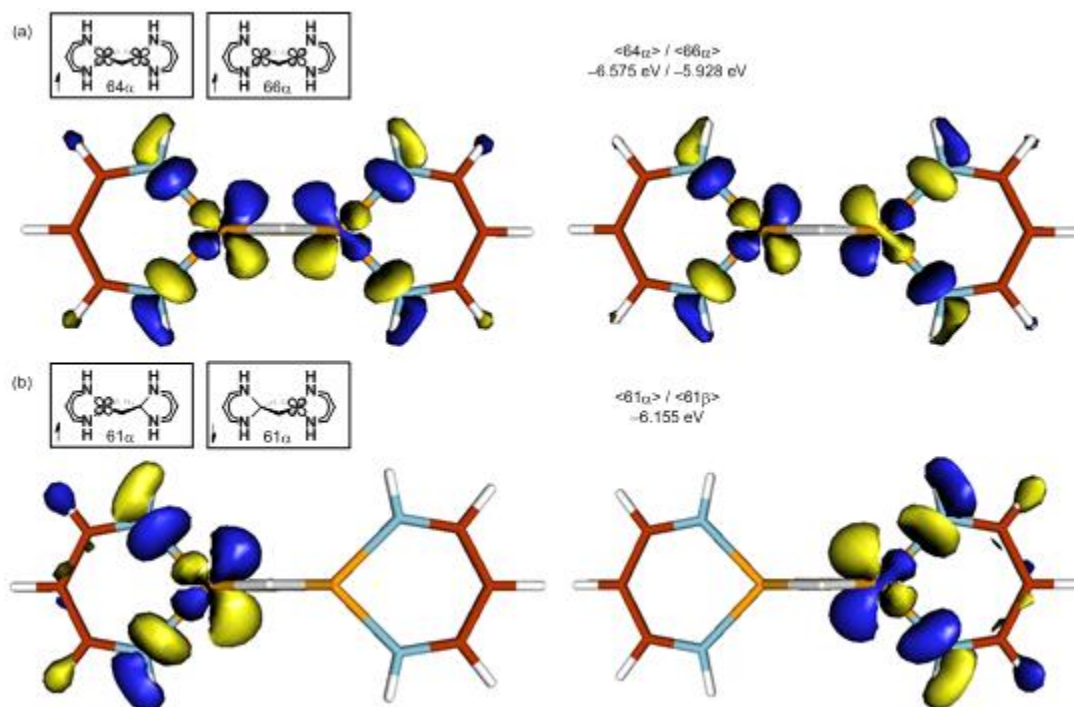|	G(sol)
1-AF	-73136.623
1-F	-73136.655
2-AF	-18039.239
2-F	-18039.185
3-AF	-23446.852
3-MONO	-11723.068
4-AF	-22138.135
4-MONO	-11068.534
5-AF	-78544.608
5-MONO	-39271.814
6-AF	-76152.524

Fig. S2.5. Isosurface plots (isodensity = 0.05 au) of the metal d_{xz}-based MOs of **2**: metal–metal in-phase, and out-of-phase α-spin, **2-F** (b) α-spin and β-spin, **2-AF**.